

GROWTH AND CHARACTERIZATION
OF HIGH-PURITY AND IRON-DOPED
PHOTOREFRACTIVE BARIUM TITANATE

by

Peter Gerard Schunemann

B.S., Massachusetts Institute of Technology

(1984)

SUBMITTED IN PARTIAL FULFILLMENT
OF THE REQUIREMENTS OF THE DEGREE OF

MASTER OF SCIENCE
IN MATERIALS SCIENCE AND ENGINEERING

at the

MASSACHUSETTS INSTITUTE OF TECHNOLOGY

June 1987

c Massachusetts Institute of Technology 1987

Signature of Author _____
Department of Materials Science and Engineering
May 8, 1987

Certified by _____
Harry L. Tuller
Thesis Supervisor

Accepted by _____
Samuel M. Allen
Chairman, Departmental Committee on Graduate Students

MASSACHUSETTS INSTITUTE
OF TECHNOLOGY

JUN 22 1987

LIBRARIES Archives

GROWTH AND CHARACTERIZATION
OF HIGH PURITY AND IRON-DOPE
PHOTOREFRACTIVE BARIUM TITANATE

by

Peter Gerard Schunemann

Submitted to the Department of Materials Science and Engineering on May 8, 1987 in partial fulfillment of the requirements for the Degree of Master of Science in Materials Science and Engineering

ABSTRACT

Variable-valent iron impurities, present at levels sufficient to lead to active trap densities of $\sim 10^{16}/\text{cm}^3$, have been suggested as the source of charge carriers responsible for the photorefractive effect in barium titanate. High-Purity BaTiO_3 single crystals were grown from starting materials purified by various chemical techniques to lower transition-metal impurity levels below this $10^{16}/\text{cm}^3$ baseline. Iron-doped crystals were grown from the same material with concentrations of 5, 50, 250, 500, 750, and 1000ppm Fe. "Pure" and doped crystals were characterized by high-temperature electrical conductivity, optical absorption, and holographic diffraction efficiency measurements in the P_{O_2} range from 1 to 10^{-4}atm . The results are consistent with a quantitative defect-chemical model derived from the literature. Based on preliminary photorefractive evaluation of high-purity and Fe-doped BaTiO_3 in the as-grown, oxidized, and reduced conditions, it appears that iron is not the dominant photorefractive species in this material.

Thesis Supervisor: Dr. Harry L. Tuller
Title: Professor of Ceramics and Electronic Materials,
Department of Materials Science and Engineering

TABLE OF CONTENTS

ABSTRACT	2
LIST OF FIGURES	6
LIST OF TABLES	8
ACKNOWLEDGEMENTS	10
I. INTRODUCTION	12
A. Photorefractive Effect: Definitions and Applications	12
B. Proposed Model	14
C. Identification of Photorefractive Species: Review	15
D. The Goal of this Work	18
II. THEORETICAL BACKGROUND	19
A. Barium Titanate Defect Chemistry	19
1. Pure BaTiO ₃	20
2. The Role of Acceptor Impurities	21
3. Variable-Valent Acceptors	24
B. Optical Absorption Spectroscopy	28
1. Optical Absorption in BaTiO ₃	28
2. Useful Relations	32
C. Diffraction Efficiency	33
III. EXPERIMENTAL PROCEDURE	35
A. Purification of Starting Materials	35
1. Titanium Dioxide Synthesis	35
2. Barium Carbonate Synthesis	37
B. Single Crystal Growth	38
C. Optical Sample Preparation	39
D. Electrical Measurements	41
E. Optical Absorption Measurements	43
F. Diffraction Efficiency Measurements	45
IV. EXPERIMENTAL RESULTS	45
A. Evaluation of Sample Purity	45
B. Coloration Phenomena	47
C. Electrical Conductivity	48
D. Curie Temperature	51
E. Optical Absorption	51
1. Visible Spectrum	51
2. Near-Infrared Spectrum	53
F. Diffraction Measurements	54

V. DISCUSSION	55
A. Electrocoloration	55
B. Background Acceptor Concentrations	57
C. Interpretation of Absorption Spectra	60
1. Visible Absorption	60
2. Near-Infrared Features	62
D. Interpretation of Photorefractive Behavior	63
VI. CONCLUSIONS	67
VII. RECOMMENDATIONS	68
REFERENCES	71
FIGURES AND TABLES	76
APPENDIX 1	136
APPENDIX 2	143
BIOGRAPHICAL NOTE	144

LIST OF FIGURES

Figure 1. Difference between the reflections of a conventional mirror and a phase conjugate mirror.

Figure 2. Phase conjugation by four-wave mixing in a photorefractive crystal. (from reference 2)

Figure 3. Model for the photorefractive effect. (a) Generation of refractive index gratings. (b) Sources and traps for photorefractive charge carriers. (from reference 19)

Figure 4. (a) Typical equilibrium conductivity isotherms for undoped BaTiO_3 (from reference 34). (b) Theoretical Kroger-Vink Diagram illustrating the role of acceptor impurities in the defect chemistry of BaTiO_3 . Dashed lines represent the effect of increasing the acceptor concentration from $[\text{A}']_1$ to $[\text{A}']_2$.

Figure 5. Idealized Kroger-Vink Diagram for BaTiO_3 doped with variable-valent Fe.

Figure 6. Variations in the $\text{Fe}^{3+}/\text{Fe}^{4+}$ valence ratio with increasing iron content.

Figure 7. Variations in the $[\text{Fe}^{2+}]$, $[\text{Fe}^{3+}]$, and $[\text{Fe}^{4+}]$ as a function of P_{O_2} at various Fe concentrations.

Figure 8. Tanabe-Sugano diagrams for (a) Fe^{4+} , d^4 ; (b) Fe^{3+} , d^5 ; and (c) Fe^{2+} , d^6 . (from reference 43)

Figure 9. Optical absorption bands in Fe-doped SrTiO_3 (2300ppm). (a) oxidized, $\text{P}_{\text{O}_2} = 1\text{atm}$; (b) reduced, $\text{P}_{\text{O}_2} = 10^{-4}$ to 10^{-7}atm ; (c) heavily-reduced, $\text{P}_{\text{O}_2} = 10^{-26}\text{atm}$. (from reference 41)

Figure 10. Typical experimental arrangement for holographic diffraction efficiency measurements. (from reference 9)

Figure 11. Flow-chart for preparation of high-purity TiO_2 .

Figure 12. Fractional-distillation system used for the purification of titanium isopropoxide, $\text{Ti}(\text{OC}_3\text{H}_7)_4$.

Figure 13. Flow chart for purification and synthesis of BaCO_3 . (D.R. Gabbe)

Figure 14. Typical single crystal boule grown by TSSG.

Figure 15. 90 degree domain walls (diagonal lines) in unpoled BaTiO_3 single crystal.

Figure 16. Typical voltage-temperature-time profile used for electrical poling.

Figure 17. Extreme example of cracking near the positive electrode which can occur during electrical poling of a sample with residual internal stresses.

Figure 18. Sample holder used for high-temperature electrical conductivity measurements, shown here with optical samples mounted for annealing.

Figure 19. Ultraviolet spectra of reagent BaCl_2 and purified BaCO_3 dissolved in HCl . Peak at 230nm corresponds to iron impurities removed by purification.

Figure 20. Optical absorption spectra comparing relative purity of BaTiO_3 single crystals grown from different feed materials.

Figure 21. Coloration bands observed after prolonged oxygen annealing and subsequent electrical poling of 500ppm (bottom) and 1000ppm (top) Fe-doped BaTiO_3 .

Figure 22. Color bands formed in 500ppm (bottom) and 1000ppm (top) Fe-doped BaTiO_3 during electrical poling in an oil bath.

Figure 23. Equilibrium electrical conductivity data for high purity BaTiO_3 single crystal.

Figure 24. Equilibrium electrical conductivity data for BaTiO_3 single crystal doped with 50ppm Fe.

Figure 25. Equilibrium electrical conductivity data for BaTiO_3 single crystal doped with 500ppm Fe.

Figure 26. Equilibrium electrical conductivity data for BaTiO_3 single crystal doped with 1000ppm Fe.

Figure 27. Arrhenius plots comparing electrical conductivity of high purity, 50, 500, and 1000ppm Fe-doped BaTiO_3 : $P_{\text{O}_2} = 1\text{atm}$.

Figure 28. Arrhenius plots comparing electrical conductivity of high purity, 50, 500, and 1000ppm Fe-doped BaTiO_3 : $P_{\text{O}_2} = 10^{-1}\text{atm}$.

Figure 29. Arrhenius plots comparing electrical conductivity of high purity, 50, 500, and 1000ppm Fe-doped BaTiO_3 : $P_{\text{O}_2} = 10^{-2}\text{atm}$.

Figure 30. Arrhenius plots comparing electrical conductivity of high purity, 50, 500, and 1000ppm Fe-doped BaTiO_3 : $P_{\text{O}_2} = 10^{-3}\text{atm}$.

Figure 31. Arrhenius plots comparing electrical conductivity of high purity, 50, 500, and 1000ppm Fe-doped BaTiO_3 : $P_{\text{O}_2} = 10^{-4}\text{atm}$ ($\log P_{\text{O}_2} = -3.84$ measured).

Figure 32. Typical plot of dielectric constant vs. temperature indicating cubic-to-tetragonal phase transition.

Figure 33. Optical absorption spectra for as-grown crystals after mechanical poling: (a) E parallel to c; (b) E perpendicular to c.

Figure 34. Effect of electrical poling on absorption spectra (crystals not shown did not survive electrical poling): (a) E parallel to c; (b) E perpendicular to c.

Figure 35. Effects of oxidation ($P_{\text{O}_2} = 1\text{atm}$, 800°C) and reduction ($P_{\text{O}_2} = 10^{-4}\text{atm}$, 800°C) on the absorption spectra of high purity BaTiO_3 : (a) E parallel to c; (b) E perpendicular to c.

Figure 36. Effects of oxidation ($P_{\text{O}_2} = 1\text{atm}$, 800°C) and reduction ($P_{\text{O}_2} = 10^{-4}\text{atm}$, 800°C) on the absorption spectra of BaTiO_3 :50ppm Fe: (a) E parallel to c; (b) E perpendicular to c.

Figure 37. Effects of oxidation ($P_{\text{O}_2} = 1\text{atm}$, 800°C) and reduction ($P_{\text{O}_2} = 10^{-4}\text{atm}$, 800°C) on the absorption spectra of BaTiO_3 :500ppm Fe: (a) E parallel to c; (b) E perpendicular to c.

Figure 38. Effects of oxidation ($P_{\text{O}_2} = 1\text{atm}$, 800°C) and reduction ($P_{\text{O}_2} = 10^{-4}\text{atm}$, 800°C) on the absorption spectra of BaTiO_3 :1000ppm Fe: (a) E parallel to c; (b) E perpendicular to c.

Figure 39. Typical NIR absorption spectra (860-3200nm) indicating the agreement of absorbance correction for two different thicknesses.

Figure 40. Spectral features in the NIR region between 2700 and 3200nm for BaTiO_3 doped with (a) "pure", 5, 50, 250ppm Fe; (b) 500, 750, 1000ppm Fe.

Figure 41. Spectral features in the NIR region after electrical poling.

Figure 42. Effects of oxidation ($P_{\text{O}_2} = 1\text{atm}$, 800°C) and reduction ($P_{\text{O}_2} = 10^{-4}\text{atm}$, 800°C) on NIR features: High-Purity BaTiO_3 .

Figure 43. Effects of oxidation ($P_{\text{O}_2} = 1\text{atm}$, 800°C) and reduction ($P_{\text{O}_2} = 10^{-4}\text{atm}$, 800°C) on NIR features: BaTiO_3 :50ppmFe.

Figure 44. Effects of oxidation ($P_{O_2} = 1\text{atm}$, 800°C) and reduction ($P_{O_2} = 10^{-4}\text{atm}$, 800°C) on NIR features: BaTiO_3 :500ppm Fe.

Figure 45. Effects of oxidation ($P_{O_2} = 1\text{atm}$, 800°C) and reduction ($P_{O_2} = 10^{-4}\text{atm}$, 800°C) on NIR features: BaTiO_3 :1000ppm Fe.

Figure 46. Diffracted beam intensity vs. time for as-grown BaTiO_3 :High-Purity, 50, 500, 1000ppm Fe.

Figure 47. Diffracted beam intensity vs. time for oxidized BaTiO_3 :High-Purity, 50, 500, 1000ppm Fe.

Figure 48. Diffracted beam intensity vs. time for reduced BaTiO_3 :High-Purity, 50, 500, 1000ppm Fe.

Figure 49. Slight temperature dependence of acceptor concentrations derived from the p-type conductivities of high-purity, 50, 500, and 1000ppm Fe-doped BaTiO_3 at $P_{O_2} = 0.1\text{atm}$.

Figure 50. Derived acceptor content vs. Fe doping level. Slope indicates that the added Fe is only 30% effective as an electronic acceptor.

Figure 51. Systematic shift in the optical band edge (taken at $\alpha = 19\text{cm}^{-1}$) with increasing Fe content.

Figure 52. $\text{Log}\alpha_{620}$ vs. $\text{log}[\text{Fe}]_{\text{tot}}$, illustrating the trend toward the theoretical $1/2$ dependence at higher Fe concentrations.

Figure 53. P_{O_2} -dependence of the 620nm absorption coefficient (Fe^{4+}) approaching the predicted $1/4$ slope with increasing Fe content.

Figure 54. Linear dependence of 3010/3050nm peak area on Fe content, which saturates near 1000ppm Fe.

Figure 55. P_{O_2} dependence of the maximum diffracted beam intensity for "pure", 50, 500, and 1000ppm Fe-doped BaTiO_3 crystals.

Figure A1.1 Schematic of furnace used for single crystal growth.

Figure A1.2 BaO-TiO_2 phase diagram.

Figure A1.3 BaTiO_3 single crystals grown by TSSG.

LIST OF TABLES

Table 1. Defect-chemical relations for variable-valent acceptor-doped BaTiO_3 for seven P_{O_2} -dependent defect regimes (plotted schematically in Figure 5).

Table 2. Boiling points of titanium isopropoxide and the isopropoxides of various possible impurities, $\text{M}(\text{iOC}_3\text{H}_7)_n$, where n is the valence of the metal or rare earth impurity M .

Table 3. Spark-source mass spectrographic analysis of reagent precursors, purified feed materials, and resulting BaTiO_3 single crystal (Quantities given in ppm atomic).

Table 4. P_{O_2} dependence m of p-type electrical conductivity, where $\sigma \propto \text{P}_{\text{O}_2}^{1/m}$.

Table 5. Enthalpies of oxygen vacancy formation, ΔH_p , calculated from Arrhenius slopes in Figures 27-31. (Values from high-temperature fit in parentheses.)

Table 6. Curie temperature ($^{\circ}\text{C}$) dependence on Fe concentration and annealing atmosphere.

Table A1. Details of BaTiO_3 crystal growth runs. (Resulting crystals shown in Figure A1.3.)

Table A2. Dimensions of single crystal samples used for optical evaluation. (Thickness a_1 used for optical absorption and diffraction efficiency measurements.)

ACKNOWLEDGEMENTS

I would like to thank my advisor Prof. Harry Tuller for his guidance availability, and encouragement throughout the course of this research, and for his thoughtful edits of this document. Likewise, I am grateful to Dr. Hans Jenssen for his generous insight and assistance on this project. I am indebted to Dr. Dave Gabbe for his extensive help with the preparation and evaluation of high-purity feed materials, and for the use of his clean room. Professor Cardinal Warde and his students Doyle Temple and Scott Hathcock also provided invaluable collaboration on this project. I am particularly indebted to Doyle for his initial help with crystal growth and sample preparation, and for the photorefractive measurements he performed. I also enjoyed many stimulating discussions (and hearty laughs) with him and Scott in the WCBTR. I would like to acknowledge Leo Torrenzio at Sanders Associates for his generous help with polishing and poling, and Tom Pollak for patiently awaiting the completion of my studies. I want to express my appreciation for for the assistance of the students in Prof. Tuller's group, and particularly Peter Moon and Gyeong-Man Choi for their helpfulness with electrical measurements and data reduction. I also owe sincere thanks to Dr. H.-J. Hagemann, Philips GmbH Forschungslaboratorium, Aachen, West Germany for his prompt and thoughtful provision of important thermodynamic data, and Martin Hartog for help with translation.

In addition to my professional colleagues, I owe great thanks to my family and friends for emotional and prayerful support and often sacrificial service. At the top of this list is my wife, Mary Ann, who not only lovingly endured my many long days and nights in lab but also typed this manuscript in its entirety. This thesis is as much hers as it is my own. I would also like to thank my parents for providing me with an education and with the understanding and encouragement to complete it. Among my friends I acknowledge in particular Brent Chambers for his faithful companionship throughout graduate school, and Beth Bigelow, Todd Kjos and Nick Rowe for preparing various figures in this document.

Above all I give thanks to my God, who taught me perseverance and held both me and my crystals together during the research process.

*The man who plants and the man who waters have one purpose,
and each will be rewarded according to his own labor.
(I Corinthians 3:8)*

Dedicated to those who will continue in the research that I
have begun. May they find success and satisfaction in their
labors.

I. INTRODUCTION

A. *Photorefractive Effect: Definitions and Applications*

The photorefractive effect is an optical phenomenon which occurs in a class of materials, known as nonlinear optical materials, whose optical properties are affected by light. Named in analogy to the well known photochromic effect (used to describe light-induced absorption changes), the photorefractive effect describes optically-induced refractive index changes.

The photorefractive effect was first discovered over twenty years ago in LiNbO_3 , LiTaO_3 , and BaTiO_3 .¹ At that time researchers at Bell laboratories discovered that an intense laser beam focused into these crystals caused a local change in the refractive index at the focus. Originally termed "optical damage" or "laser damage," the effect has since been used to advantage in a wide variety of holographic applications.

Many applications of the photorefractive effect involve optical phase conjugation by four-wave mixing. The process of optical phase conjugation is illustrated in Figure 1. If a plane wave incident on a conventional mirror passes through a distorting medium such as a glass cylinder, the reflected wave traverses the cylinder in reverse, doubling the distortion (Figure 1a). Phase conjugation, however, produces a reflected wave whose wavefront is reversed with respect to the direction of the beam, thus creating an

"anti-distorted" beam whose distortion is removed upon retraversing the medium (Figure 1b). An additional consequence of phase conjugation is that the reversed or "phase conjugate" wave retraces the path of the incident beam regardless of the incident angle (Figure 1c).²

Optical phase conjugation is performed in photorefractive crystals by a method known as four-wave mixing. The "four-waves" refer to an object beam, two reference beams (a "write" beam and a "read" beam), and the resulting phase conjugate beam. The geometry of such an experiment is shown in Figure 2. The object beam and one of the reference beams (the "write" beam) generate a three-dimensional interference pattern (i.e. a hologram) in the crystal which is stored as a corresponding pattern of refractive index variations via the photorefractive effect. The second reference beam comes from a direction opposite to that of the first one and is reflected by the zones of the stored interference pattern, "reading" the phase information of the object beam. The sum of these reflections from each zone of the interference pattern is the phase conjugate beam which retraces the path of the object beam. Since the writing and reading of the hologram occur simultaneously, four-wave-mixing is a form of dynamic holography.²

Optical phase conjugation by four-wave mixing in photorefractive crystals has many exciting applications. Since a phase-conjugate beam returns to its place of origin free of distortion, it is ideal for use in the pointing and

tracking of moving objects, optical image and data processing, interferometry, laser gyroscopes, fiber optic and satellite communications systems, photolithography, and laser weapon systems.³

B. Proposed Model

The first model to explain the occurrence of light-induced refractive index changes was proposed by Chen.⁴ The process, illustrated in Figure 3, consists of four steps: (1) upon illumination of the crystal, electrons (or holes) are optically excited from filled donor (acceptor) sites into the conduction (valence) band; (2) the excited carriers migrate by diffusion and drift and are re-trapped and re-excited until they drift into dark regions of the crystal where they can no longer be re-excited; (3) the redistribution of filled and empty traps creates a space charge grating which is balanced by a space charge electric field; (4) the space charge field modulation, δE , causes a corresponding spatial variation of the refractive index, Δn , via the linear electro-optic effect, i.e.,

$$\Delta n = 1/2n_b^3 r_{eff} \delta E \quad (1)$$

where n_b is the appropriate tensor component of the refractive index and r_{eff} is the effective electro-optic coefficient. This model is still the accepted one, except that the presence of a large internal electric field, proposed but unexplained by Chen to account for carrier

migration, has since been explained by the bulk photovoltaic effect.⁵

C. *Identification of Photorefractive Species: Review*

Following Chen's observation and proposed model for "optical damage", considerable research was devoted to identifying the centers responsible for the effect. Most of these studies focused on LiNbO_3 and LiTaO_3 , and early results suggested oxygen vacancies, impurities, or cation defects as the sources of photorefractive charge carriers.^{4,6-8} Peterson, Glass, and Negran⁹ were the first to link iron impurities to the cause of the photorefractive effect. Using diffraction efficiency to quantify "damage susceptibility," electron paramagnetic resonance (EPR) to identify Fe^{3+} , and optical absorption as an indication of Fe^{2+} , they examined the effects of Fe-doping and annealing atmosphere on the photorefractive properties. Their conclusion, that Fe^{2+} acted as the source of photoelectrons and Fe^{3+} as the electron traps in the dark regions, explained all previous observations and inspired much additional research,¹⁰⁻¹⁷ concluding with a very systematic study by Kurz et al,¹⁸ which strongly correlated the photorefractive effect in lithium niobate to the presence of Fe^{2+} and Fe^{3+} . The results of these studies did not entirely rule out, however, the role of compensating defects such as oxygen vacancies in the photorefractive process.

The source of photorefractive charge carriers in barium titanate is less clear. BaTiO_3 is of particular interest among photorefractive materials because it has demonstrated the highest four-wave-mixing reflectivities (greater than a factor of 20) by virtue of its large electro-optic coefficients.^{19,20} Research to isolate the photorefractive species in BaTiO_3 has been limited, however, by the difficulty in preparing single domain samples. Micheron and Bismuth^{21,22} reported an increase in induced birefringence changes and storage time for 0.1wt% Fe-doped crystals over nominally pure crystals. These results are inconclusive, however, because flux-grown crystals were used²³ which are inherently very impure and yield small samples.

More recently Klein and Schwartz^{24,25} reported the photorefractive properties of a group of nominally undoped samples of melt-grown BaTiO_3 whose iron levels were determined by chemical analysis. At the same time Ducharme and Feinberg²⁶ reported the effects of oxidation and reduction on similar samples from the same commercial source.²⁷ In the former studies Klein and Schwartz found a general increase in the photorefractive trap density, Fe^{3+} EPR signal, and absorption coefficient with increasing iron content over a narrow concentration range (~50-150ppm), but had no knowledge or control of the oxidation state of the crystals. Ducharme and Feinberg, on the other hand, varied the oxidation state of their crystal by annealing in oxidizing and reducing atmospheres but had no indication of

the Fe content or other impurity levels. Based on their results, both groups identified Fe^{3+} and Fe^{2+} centers as the donors and traps respectively of photorefractive carriers when the carriers are holes (and vice-versa for electrons). Ducharme and Feinberg also proposed oxygen and barium vacancies as possible photorefractive species, but in neither case was the iron concentration or valence ratio systematically varied over an appreciable range.

The only reported study of the photorefractive properties of intentionally doped BaTiO_3 , is the very recent work of Godefroy *et al.*^{28,29} They measured the maximum diffraction efficiency, writing speed, and electro-optic coefficients in a series of crystals doped with a wide range of Fe concentrations (undoped to 2500ppm). They reported that all measured parameters were highest in the 750ppm Fe-doped crystal, with the diffraction efficiency increasing by a factor of 1000 over that of the undoped crystal. A major shortcoming of this work, however, is that the measured crystals were neither electrically nor mechanically poled, while the measurements they performed are particularly sensitive to the presence of 90 and 180 degree domains. In fact, their own investigations of the crystal domain structure (performed using a unique optical topography approach) indicated a low degree of poling and notable variation among crystals. Consequently their observations may simply reflect differences in domain structure among doped crystals.

D. *The Goal of this Work*

The goal of this research is to gain more insight into the identity of the photorefractive species in barium titanate. This is accomplished by controlling the concentrations and valence states of impurities and native defects in a series of crystals and correlating them with their measured photorefractive properties. Our approach is based on the popular theory that variable-valent transition-metal ions, in particular divalent and trivalent iron impurities, are the species responsible for photorefractive charge carriers in barium titanate.

Our strategy for evaluating the effects of such centers on the photorefractive behavior of barium titanate is three-fold. Since it has been estimated that the density of charge carriers involved in the photorefractive effect is on the order of $10^{16}/\text{cm}^3$,³⁰ the first goal of this project was to prepare high purity single crystals with transition-metal and aliovalent impurity levels below this baseline. Since this is one to three orders of magnitude lower than the impurity levels of BaTiO_3 samples studied thus far, a substantial lowering or disappearance of photorefractivity should occur if transition-metals are the sole centers responsible for the effect.

The second goal of this project was to study the effect of iron impurities by systematically doping the above mentioned high purity melt, since doping over an extended

range in the presence of low baseline impurity levels would allow a more rational interpretation of the dopant effects.

Thirdly, our aim is to employ a defect chemical approach to study the effects of Fe valence and native defect levels on the photorefractive performance of our crystals. Defect models for undoped,³¹⁻³⁵ acceptor-doped,^{36,37} and specifically transition-metal-doped³⁸⁻⁴¹ BaTiO₃ have been well-developed based on previous high-temperature electrical conductivity and thermogravimetric studies. These models, as described in the next section, allow for the calculation of concentration levels of Fe in its various valence states, as well as native defect levels, as a function of annealing temperature, oxygen partial pressure, and total Fe content. These levels, in turn, can be monitored by optical absorption, high-temperature electrical conductivity, and chemical analysis, and correlated with general trends in the photorefractive behavior as indicated by holographic diffraction efficiency measurements.

II. THEORETICAL BACKGROUND

A. Barium Titanate Defect Chemistry

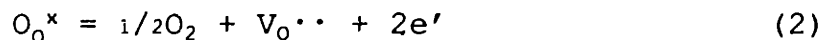
In order to best describe the established defect models for BaTiO₃, let us begin with a simplified picture involving only native defects before incorporating the roles of inadvertent acceptor impurities and variable-valent dopants.

1. Pure BaTiO₃

The construction of a defect-chemical model requires knowledge or assumptions to be made concerning (1) the character of the primary intrinsic ionic disorder, (2) the ionization state of the defects at the temperature of interest, and (3) the valence and lattice sites occupied by the dopant or impurity ions (if any).

If we consider the hypothetical case of pure barium titanate with a Ba/Ti ratio of unity, a very simplified model can be based on the following assumptions: (1) intrinsic ionic disorder contributes negligibly to the defect structure; (2) all defects are fully ionized. The first assumption can be made because of the high ionic charges and the lack of suitable interstitial sites in BaTiO₃, and is supported by the findings of Eror and Smyth.³³ The second assumption is almost certainly realized at the elevated temperatures (650°C) required for equilibration. The resulting model would predict just two regimes of P_{O₂}-dependent defect behavior.

At very low oxygen-partial pressures and elevated temperatures, oxygen vacancies would be created and balanced by the generation of mobile electrons according to the reaction



with an equilibrium constant for reduction given by

$$K_n = [V_o^{\bullet\bullet}]n^2P_{O_2}^{1/2} = K_n''\exp(-\Delta H_n''/kT) \quad (3)$$

Here the notation is that of Kroger and Vink,⁴² and ΔH_n° is the standard enthalpy of reduction associated with the formation of doubly-ionized oxygen vacancies. The electroneutrality condition in this region would be approximated by

$$2[V_{O^{\bullet\bullet}}] = n \quad (4)$$

such that the material would exhibit n-type electrical conductivity given by

$$\sigma_e = n e \mu_e = (2K_n)^{1/3} P_{O_2}^{-1/6} e \mu_e \quad (5)$$

At higher P_{O_2} 's, once all the oxygen vacancies were effectively filled, pure stoichiometric $BaTiO_3$ would behave simply as an intrinsic semiconductor with the generation of electron-hole pairs given by

$$= e' + h^\circ \quad (6)$$

$$np = K_i = K_i' \exp(-E_g/kT) \quad (7)$$

where K_i' is equal to $N_C N_V$, the product of the densities of states in the conduction and valence bands, and E_g is the band gap energy.

2. The Role of Acceptor Impurities

Actual studies³¹⁻³⁶ of the defect chemistry of undoped barium titanate by means of equilibrium electrical conductivity measurements indicate an additional region of p-type conductivity for which this simple model does not account. Typical results are shown in Figure 4(a), plotted as $\log \sigma$ vs $\log P_{O_2}$. The p-type conductivity is represented at high oxygen partial pressures as an increase in conductivity with increasing P_{O_2} , while at low P_{O_2} the

conductivity changes to n-type. The $-1/4$ and $+1/4$ dependencies of $\log\sigma$ vs $\log P_{O_2}$ observed for the n-type and p-type regions respectively are inconsistent with the above model.

These inconsistencies can be explained by assuming the presence of a species with a net negative charge, i.e., an acceptor. Seuter³⁶ proposed that barium vacancies, resulting from a non-stoichiometric excess of Ti, act as a constant background acceptor concentration. Chan and Smyth,³⁵ however, found that variations in the Ba/Ti ratio had no effect on the conductivity behavior, presumably because of electrostatic association of V_{Ba}'' and $V_{O}^{\bullet\bullet}$ into uncharged complexes. Instead, the latter proposed that accidental acceptor impurities, which are far more abundant in nature than possible donor impurities, were present in all undoped $BaTiO_3$ samples investigated and account for an extrinsic excess of oxygen vacancies.

In the region where the total concentration of oxygen vacancies is fixed by acceptor impurities, the electroneutrality relation is given by

$$2[V_{O}^{\bullet\bullet}] = [A'] \quad (8)$$

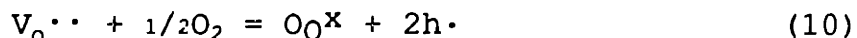
Substitution of Equation (8) into Equation (3) gives

$$\begin{aligned} n &= (2K_n/[A'])^{1/2} P_{O_2}^{-1/4} \\ &= (2K_n''/[A'])^{1/2} \exp(-\Delta H_n''/2kT) P_{O_2}^{-1/4} \end{aligned} \quad (9)$$

At lower P_{O_2} 's and high temperatures, the concentration of oxygen vacancies will exceed the extrinsic levels and be

compensated by electrons, as indicated by Equations (2)-(4) of our simpler model.

At higher P_{O_2} 's, however, the extrinsically generated oxygen vacancies will begin to be partially filled according to the reaction



with a corresponding mass-action relation of

$$p^2/[V_o^{\bullet\bullet}] = K_p P_{O_2}^{1/2} = K_p'' \exp(-\Delta H_p''/kT) P_{O_2}^{1/2} \quad (11)$$

Substitution of Equation (8) into Equation (11) yields

$$p = ([A'] K_p''/2)^{1/2} \exp(-\Delta H_p''/2kT) P_{O_2}^{1/4} \quad (12)$$

with a corresponding p-type conductivity

$$\sigma = pe\mu_n = e\mu_n ([A'] K_p''/2)^{1/2} \exp(-\Delta H_p''/2kT) P_{O_2}^{1/4} \quad (13)$$

explaining the observed $+1/4$ slope-dependence of $\log\sigma$ vs $\log P_{O_2}$.

At still higher oxygen partial pressures the acceptor generated oxygen vacancies could be sufficiently depressed to saturate the hole concentration at

$$p = [A'] \quad (14)$$

The relative concentrations of holes, electrons, oxygen vacancies, and acceptor impurities in these P_{O_2} regimes are plotted schematically in Figure 4b.

The net effect of increasing the background acceptor levels is indicated by the dashed lines in Figure 4b. If the total acceptor concentration is increased from $[A']_1$ to $[A']_2$, then : (1) the extrinsically controlled oxygen vacancy regime (Region II) expands to cover a broader P_{O_2} range; (2) the hole and electron concentrations in this region are increased and decreased respectively according to Equations (9) and (12); (3) the location of the conductivity minimum, $P_{O_2}^0$, is shifted to lower oxygen partial pressures. An expression for $P_{O_2}^0$ as a function of acceptor content, then can be derived from Equations (9) and (12) for the condition $n\mu_e = p\mu_h$, where μ_e and μ_h are the electron and hole mobilities respectively. Chan et al³⁷ give this relation as

$$P_{O_2}^0 = 4 (\mu_n/\mu_p)^2 (1/[A']^2) (K_n''/K_p'') \exp(-(\Delta H_n'' - \Delta H_p'')/kT) \quad (15)$$

from which one obtains

$$d\log P_{O_2}^0 / d\log [A'] = -2 \quad (16)$$

The position of the conductivity minimum, then, serves as a convenient parameter for the comparison of background acceptor levels, shifting two orders of magnitude lower in P_{O_2} for each order of magnitude increase in acceptor concentration.

3. Variable-valent Acceptors

The defect chemistry of $BaTiO_3$ grows still more complex when the acceptor impurities or dopants can exist in more

than one stable valence state. Such is the case for transition metal ions, in particular Cr, Mn, Fe, Co, and Ni, substituted at titanium sites. Transition-metal doped BaTiO_3 has been carefully studied by Hagemann *et al*³⁸⁻⁴¹ by means of thermogravimetry and Mossbauer spectroscopy.

To account for acceptors in variable valence states, our defect model must be expanded to include the acceptor ionization reactions



for more reducing conditions and



for more oxidizing conditions, where A_{Ti}'' , A_{Ti}' and A_{Ti}^x represent di-, tri-, and tetra-valent dopants respectively on Ti sites. These reactions have the corresponding mass action relations

$$[A_{\text{Ti}}']n/[A_{\text{Ti}}''] = K_D'' = 1/2N_c \exp(-(E_g - E_A^{2-})/kT) \quad (19)$$

$$[A_{\text{Ti}}^x]n/[A_{\text{Ti}}'] = K_D' = 2N_c \exp(-(E_g - E_A^-)/kT) \quad (20)$$

where N_c is the density of states in the conduction band, E_g is the band gap of BaTiO_3 and E_A^- and E_A^{2-} are the ionization energies from the top of the valence band of A^{3+} and A^{2+} respectively.

The consequence of acceptors existing in variable valence states is that there are then two regimes in which

the oxygen vacancy concentration is extrinsically controlled. The charge neutrality condition

$$[A_{Ti}'] + 2[A_{Ti}''] = 2[V_O^{\bullet\bullet}] \quad (21)$$

applies in the transition region from the divalent to the trivalent state or to Eq. (8) when only trivalent and tetravalent acceptors are present.

The above Equations (17)-(21), along with the acceptor mass conservation conditions

$$[A_{Ti}]_{tot} = [A_{Ti}''] + [A_{Ti}'] \quad (\text{reducing}) \quad (22)$$

$$[A_{Ti}]_{tot} = [A_{Ti}'] + [A_{Ti}^x] \quad (\text{oxidizing}) \quad (23)$$

can be incorporated into the defect model developed thus far to yield $[V_O^{\bullet\bullet}]$, n , p , $[Fe^{2+}]$, $[Fe^{3+}]$, and $[Fe^{4+}]$ as functions of P_{O_2} , temperature, and $[Fe]_{tot}$ for Fe-doped $BaTiO_3$. These Equations are listed in Table 1 for five P_{O_2} -dependence regimes and plotted schematically on an idealized Kroger-Vink diagram, Figure 5. (Note that if the total iron concentration Fe_{tot} is below that of the background acceptor concentration, the majority defect concentrations will be governed by the model in Figure 4b.)

Equation (3) can be combined with Equations (19) and (21) or Equations (8) and (20) to yield the oxygen partial pressures corresponding to the desired ratios of $[Fe^{3+}]/[Fe^{2+}]$ or $[Fe^{4+}]/[Fe^{3+}]$ respectively. If we let $[Fe^{3+}]/[Fe^{2+}] = R_{32}$ and $[Fe^{4+}]/[Fe^{3+}] = R_{43}$ we obtain

$$P_{O_2} = K_n^2 (R_{32}+1)^2 R_{32}^4 / K_D'^4 [Fe]_{tot}^2 (2R_{32}+1)^2 \quad (24)$$

and

$$P_{O_2} = K_n^2 4 (R_{43}+1)^2 R_{43}^4 / K_D'^4 [Fe]_{tot}^2 \quad (25)$$

From these we derive the expression

$$d \log P_{O_2} / d \log R_{32} = d \log P_{O_2} / d \log R_{43} = 4 \quad (26)$$

Thus we can see that the ratio of $[Fe^{3+}]/[Fe^{2+}]$ (for reducing conditions) or the ratio of $[Fe^{4+}]/[Fe^{3+}]$ (for oxidizing conditions) increases one order of magnitude for every 4 orders of magnitude increase in P_{O_2} . Also of interest is the dependence of the Fe valence ratios on the total Fe content at a given P_{O_2} . Similar manipulation of Equations (24) and (26) yields

$$d \log [Fe]_{tot} / d \log R_{32} = d \log [Fe]_{tot} / d \log R_{43} = 2 \quad (27)$$

i.e., the ratios of $[Fe^{3+}]/[Fe^{2+}]$ and $[Fe^{4+}]/[Fe^{3+}]$ increase one order of magnitude for every two orders of magnitude increase in Fe doping level. (Note that the ratio is not constant as one might intuitively expect.) Finally, we can see that differentiating the log of Equations (24) and (25) with respect to $\log [Fe]_{tot}$ yields the same result derived in Equation (16). These trends are illustrated graphically in Figure 6.

The above equilibrium defect model for variable-valent-iron-doped barium titanate can be used to quantitatively

predict the relative concentration levels of Fe^{2+} , Fe^{3+} , and Fe^{4+} for a given set of annealing conditions and doping levels if values for the equilibrium constants K_n'' , $\Delta H_n''$ and for the activation energies E_A^- and E_A^{2-} are known. The equilibrium constants have been determined by thermogravimetric measurements⁴¹ and high-temperature-electrical conductivity measurements,^{33-35,37} which both give $K_n'' \sim 3 \times 10^{75} \text{cm}^{-9} \text{Pa}^{1/2}$ and $\Delta H_n'' \sim 9.6 \times 10^{-19} \text{J}$. The activation energies have been determined using thermogravimetry and Mossbauer spectroscopy by H. J. Hagemann.⁴¹ These results yielded values for E_A^- and E_A^{2-} of 0.8 eV and 2.4 eV respectively. These values have been inserted into the relevant defect equations, and the concentrations of $[\text{Fe}^{2+}]$, $[\text{Fe}^{3+}]$, and $[\text{Fe}^{4+}]$ are plotted vs. P_{O_2} for an annealing temperature of 800°C and the total Fe concentrations relevant to this study (0.3, 50, 500, and 1000ppm) in Figure 7, which will be used later in the interpretation of experimental results.

B. Optical Absorption Spectroscopy

1. Optical Absorption in BaTiO_3

The variations of iron valence predicted by the above model can be monitored by optical absorption spectroscopy, since the optical absorption bands of the iron ions depend on the permitted energies of the outermost valence electrons. Fe^{2+} , Fe^{3+} , Fe^{4+} ions have six, five, and four electrons respectively in their outermost d-shell, and occupy the octahedral titanium site in BaTiO_3 . In order to

determine whether these ions have any allowed optical transitions in BaTiO_3 , we must refer to the appropriate Tanabe-Sugano diagrams, shown in Figure 8.⁴³

In these diagrams, the vertical axis is the energy E measured from the ground state which is the state with the highest degree of spin. (If two states have the same spin number, then the one with the highest angular momentum is the ground state.) The horizontal axis gives the crystal field splitting denoted by $10Dq$. Both axes are given in units of B (cm^{-1}). The free ion energy levels on the left of the diagram are represented by their spin (S) and angular momentum (L) quantum numbers using the notation ^{2S+1}L , where $2S + 1$ is always given as a number and L as a letter ($S=0$, $P=1$, $D=2$, $F=3$, $G=4$, $H=5, \dots$). These energy levels split and shift with increasing crystal field intensity, and are labeled at the right of the diagram with their spin quantum number (as before) and their group theory representation.⁴⁴ According to these diagrams, no internal electric-dipole (optical) transitions are allowed for Fe^{2+} , Fe^{3+} , or Fe^{4+} for either the free ions or for pure octahedral (O_h) symmetry. (This is based on the criteria that the sum of the individual angular momentum of the electrons must change parity, i.e. from an odd to an even number or vice-versa.) It is conceivable that static and dynamic crystal field mixing of the $3d^n$ levels with higher levels of opposite parity (such as $3d^{n-1}4p^1$) might allow the selection rules to be broken, in which case the spin quantum number might serve

as a guide to determine the relative strength of a transition (generally transitions with $\Delta S = 0$ would be stronger). Even if this were the case, it is expected that all internal electric-dipole transitions in these ions would be weak.

The availability of BaTiO_3 absorption data in the literature is rather limited. Most early studies were performed on n-type semiconductive barium titanate that was heavily reduced and often donor-doped.⁴⁵⁻⁴⁹ These results indicate a shift in the band edge to longer wavelengths, and the emergence of a broad peak centered around $2\mu\text{m}$ attributed to small-polaron absorption, upon reduction in hydrogen ($\text{P}_{\text{O}_2} \sim 10^{-20}$ Pa). Didomenico and Wemple^{50,51} were the first to study melt-grown⁵² crystals. They observed an exponential Urbach tail, taken to be an intrinsic property of the BaTiO_3 lattice, and noted the absence of the large excess absorption characteristic of flux-grown crystals. Their spectra also revealed a polarization dependence of the observed band edge, which occurred at a shorter wavelength for $E \parallel c$.

Both Ducharme and Feinberg²⁶ and Klein and Schwartz²⁵ reported optical absorption data in their photorefractive studies. The former reported a broad absorption plateau extending throughout the visible (800nm to the 410nm band edge) which increased with by both oxidation and reduction treatments. They also noted a narrow absorption line at 2870nm whose height of 0.35cm^{-1} was depressed to 0.11cm^{-1} and

0.15cm^{-1} upon annealing in 10^{-6}atm and 2.0atm oxygen respectively. They attributed this to a defect or impurity color center. Klein and Schwartz reported a broad, featureless tail extending from the band edge which increased with increasing Fe content in their nominally-undoped as-grown crystals.

Although no published optical absorption spectra are available for Fe-doped BaTiO_3 , they do exist for Fe-doped SrTiO_3 ,^{41,53-55} a compound almost identical in structure to BaTiO_3 but uncomplicated by the problems of single-domain sample preparation. The most recent work of Hagemann⁴¹ includes the absorption spectra as a function of oxygen-partial-pressure. These results are shown in Figure 9 for a crystal doped with 2300ppm Fe. Under the most oxidizing conditions the absorption is characterized by peaks at 2.1 and 2.8eV (590 and 440nm) which are attributed to Fe^{4+} charge-transfer bands. These absorptions give the crystal a reddish/brownish color. Under more reducing conditions the Fe exists almost entirely in the trivalent state (cf. Figure 7), and the crystal is nearly colorless, Figure 9(b). Under extremely reducing conditions, as during high-temperature hydrogen annealing, a considerable amount of Fe^{2+} is formed as indicated by a double-band with peaks at 1.2 and 1.5eV (1030 and 825nm), Figure 9(c), resulting in a greenish color. Similar P_{O_2} -dependent absorption spectra should be observed in Fe-doped BaTiO_3 .

2. Useful Relations

The optical absorption due to defects such as Fe²⁺ and Fe⁴⁺ can serve as a direct indication of their concentration levels. The absorption coefficient α (cm⁻¹) is linearly related to the concentration of the absorbing species, c , via the Beer-Lambert equation:

$$\alpha = \epsilon c = (1/d) \ln(I_0/I) \quad (28)$$

where ϵ is the extinction coefficient, d is the optical path length, and I_0 and I are the incident and transmitted intensities respectively⁵⁶. The absorption coefficient α is determined experimentally by measuring the overall transmission of a sample, which depends on both reflection and absorption losses according to

$$T = I/I_0 = (1-R)^2 \exp(-\alpha d) \quad (29)$$

In the above equation, R is the reflectance, which is related to the refractive index by

$$R = (n-1)^2 / (n+1)^2 \quad (30)$$

for the case of normal incidence. The refractive index in BaTiO₃ is different for light polarized parallel to the c - and a -axes respectively. In addition, n_c and n_a are wavelength-dependent according to the equation⁵¹

$$n = \{ [S_0 \lambda_0^2 / (1 + \lambda_0^2 / \lambda^2)] + 1 \}^{1/2} \quad (31)$$

Where $S_0 = 91.4 \times 10^{-6} \text{nm}^{-2}$ and $\lambda_0 = 211.0 \text{nm}$ for n_c and $S_0 = 84.5 \times 10^{-6} \text{nm}^{-2}$ and $\lambda_0 = 222.8 \text{nm}$ for n_a . Thus Equations (27) and (28) can be combined to correct measured absorbance spectra for reflection losses, where the absorbance or "optical density" A is given by

$$A = \log_{10}(1/T) \quad (32)$$

If the reflectance for a given sample or wavelength region is not known (for example, Equation (31) is only valid in the visible), one can measure the absorbance of a sample at two different thicknesses d_1 and d_2 , in which case

$$\alpha = [1/(d_2 - d_1)] \ln(T_1/T_2) \quad (33)$$

The concentration of impurity centers is related not only to the absolute absorption coefficient but also to the area under the absorption peak. If the absorption coefficient (cm^{-1}) is plotted vs. energy (eV), then the area A under the absorption peak is related to the absorbing center's concentration c (cm^{-3}) through the relation⁵⁸

$$c = 0.821 \times 10^{17} \text{cm}^{-3} A n / f (n^2 + 2)^2 \quad (34)$$

where n is the refractive index and f is the atomic oscillator strength.

C. Diffraction Efficiency

Holographic diffraction efficiency measurements provide a useful means for quantifying the relative magnitude of the photorefractive effect in a crystal. The basic geometry of

such an experiment is shown in Figure 10. A recording laser beam (from the Ar⁺ laser, 514.4nm) is split with a beam splitter B and the two plane-polarized waves intersect in the crystal at an angle 2θ , creating an interference pattern stored as a refractive index grating as discussed previously. A probe beam (from the He-Ne laser, 633nm) is diffracted by the stored index grating, and the diffraction efficiency η , defined as the ratio of the intensities of the diffracted and incident probe beams, is given by⁵⁹

$$\eta = \exp(-\alpha d / \cos\theta) \sin^2(\pi \Delta n_3 d / 2\lambda \cos\theta) \quad (35)$$

where α is the absorption coefficient, d is the crystal thickness, λ is the wavelength of the read-out beam, and Δn_3 is the induced peak-to-peak refractive index change. The factor $\exp(-\alpha d / \cos\theta)$ takes into account a possible uniform background absorption, which allows for the comparison of crystals with different α values and different thicknesses.

It should be noted here that although the above equation based on the coupled-wave theory of Kogelnik was used as the basis for most of the foundational studies on LiNbO₃, it is subject to certain assumptions and limitations which are often not realized in practice. In particular, the assumption of planar diffraction gratings perpendicular to the plane of incidence does not hold for beams polarized normal to the c-axis, which is the common practice. In addition, the assumption of small absorption losses breaks

down for thick, heavily-doped crystals. Consequently, this well known equation must be used with some caution.

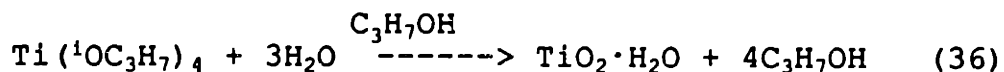
III. EXPERIMENTAL PROCEDURE

A. Purification of Starting materials

A major effort in this research was devoted to the synthesis of high-purity starting materials, since titanium dioxide and barium carbonate feed materials are not commercially available with impurity levels below the $10^{16}/\text{cm}^3$ baseline apparently required for photorefractivity

1. Titanium Dioxide Synthesis

The titanium dioxide feed material was prepared by the hydrolysis of titanium isopropoxide, $\text{Ti}(\text{}^i\text{OC}_3\text{H}_7)_4$, according to the reaction



A flow chart for the process is shown in Figure 11.

The titanium alkoxide precursor (Stauffer Chemical Co.) was first purified by a reduced pressure fractional distillation. This purification technique was based on the observation that titanium isopropoxide has a much lower boiling point than the isopropoxides of other transition-metals as listed in Table 2.⁶⁰ Consequently, upon boiling the material the vapor will be richer in titanium-isopropoxide than in the isopropoxides of its impurities. Repeated condensation and partial revaporization of this

enriched vapor yields purer and purer titanium isopropoxide. A fractional-distillation column allows this condensation-revaporization process to be carried out continuously, with the number of revaporization steps measured in "theoretical plates."

The fractional-distillation apparatus used for this process, including a system for pressure control during collection and fraction cutting, is shown in Figure 12. Its design and the details of operation were based on references 61-63. Distillation was performed under reduced pressure (5mmHg) in order to lower the boiling point and avoid reaction of the isopropoxide with atmospheric moisture. Pressure was controlled with a "cartesian-diver" type manostat and monitored with a McCleod vacuum gauge. A 600mm x 12.5mm vacuum-jacketed distilling column packed with 1/8" glass helices provided ~15-20 theoretical plates.⁶¹ Care was taken to soak all internal glassware surfaces overnight in concentrated or dilute HCl, and whenever possible teflon sleeves were used instead of vacuum grease to seal the system. Purification was qualitatively evidenced by the transformation of the alkoxide from deep-yellow to water-clear in color, leaving a dark-brown liquid and metal particulates in the still pot. (Quantitative results are given in the next section.) The collected distillate was removed under a dry-nitrogen atmosphere and transferred to the reaction flask. Deionized water diluted with semiconductor-grade isopropyl alcohol (Mallinkrodt) was

slowly added to the stirring alkoxide using a dropping funnel to form hydrated TiO_2 powder and alcohol. The powder was then vacuum-dried in the same vessel to minimize handling. The resulting hydrated powder was not calcined to avoid further handling, but instead a sample was weighed before and after oven-drying, indicating 15 to 20% water content which was compensated for during feed preparation.

2. Barium Carbonate Synthesis

Barium Carbonate was formed by reaction of a purified aqueous solution of $BaCl_2$ and urea with CO_2 in a pressurized vessel. A flow-chart for the entire synthesis process which was carried out in a class 100 clean room, is shown in Figure 13. The details of this process developed by D.R. Gabbe are discussed at length in references 64 and 65. Briefly, reagent grade $BaCl_2$ and urea, $(NH_2)_2CO$, were dissolved in water, filtered, and purified by solvent extraction. The solvent extraction involved mixing the aqueous solution with a dense immiscible liquid (in this case chloroform) containing an extracting or "chelating" agent (in this case diethylammonium diethyldithiocarbonate, or DDDC). The DDDC forms precipitates with a large number of metal ions. These precipitates segregated to the dense chloroform phase which was removed using a separatory funnel. During the process, the presence of transition metal complexes in the chloroform phase was indicated by a bright yellow or green color. The solvent extraction process was repeated with replenished chloroform phase until

it no longer became colored, and this procedure was repeated at various pH's. After extraction, the aqueous solution was refiltered and reacted under CO_2 pressure to form BaCO_3 . The BaCO_3 crystalline precipitate was then removed by centrifugation and dried in class 100 clean room air.

B. *Single Crystal Growth*

High-purity and Fe-doped BaTiO_3 single crystals were grown by the top-seeded solution growth technique (TSSG).^{52,66} Extreme care was exercised to minimize furnace contamination of the purified feed materials. The growth furnace was rebricked with new lining materials, new SiC heating elements were used, and the platinum crucible was kept covered while the closing bricks were lowered in place. Crystal growth was first initiated on a platinum wire to avoid contamination from an impure single-crystal seed. Later, high-purity single-crystal seeds cut in the $\langle 100 \rangle$ direction were used with dimensions of approximately $10 \times 2.5 \times 2.5 \text{ mm}$.

Single crystals were grown from a titanium rich melt containing 66 mole% TiO_2 , corresponding to a melting point of approximately 1380°C . (Experience has indicated that growth from melts at temperatures $> 1400^\circ\text{C}$ yields poor results.) The melt was heated slowly at first to drive out moisture, then raised from 200 to 1450°C in 20 hours and soaked for 24 to 40 hours to insure complete dissolution of the ceramic powders. Seeding temperatures, indicated by equilibrium between the melt and the air-cooled seed, varied between

1382°C and 1392°C for successful growth runs due to variations in the moisture content of the hydrated TiO_2 . (Note that the melting point is particularly sensitive to small variations in composition due to the steepness of the liquidus. See phase diagram of Rase and Roy, Appendix 1.) After seeding, the melt was cooled at 0.2°C/hour for 25 to 35 hours until pulling began at 0.15 to 2.0mm/hour. During pulling the melt was cooled at at 0.5°C/hour to temperatures slightly above the eutectic (1320°C), after which the crystal was removed from the melt and slowly cooled to room temperature. Most growth runs yielded high-optical quality single crystals. A typical boule is shown in Figure 14, and other single crystals and specific growth conditions are shown in Appendix 1.

In addition to high purity samples, crystals were grown from melts doped with 5, 50, 250, 500, 750, and 1000ppm Fe. In the case of doped crystals, iron oxide was substituted for TiO_2 in the melt according to $\text{BaCO}_3 + (1-x \cdot 10^{-6})\text{TiO}_2 + (x/2)\text{Fe}_2\text{O}_3$, where x is the doping level in ppm (atomic). A distribution coefficient of unity was assumed in accordance with Godefroy et al.⁶⁷

C. Optical Sample Preparation

The process of preparing single-domain optical samples was labor-intensive and often destructive, requiring a high degree of patience.

Crystals were cut along {100} planes as determined by the back-reflection Laue method, and faces were ground to

near-parallel with $20\mu\text{m}$ SiC. Cut and ground cubes were then polished by hand with $3\mu\text{m}$ diamond paste on a lightly-oiled paper lap. The presence of 90° domains in the polished samples was clearly indicated by sharp planar boundaries within the polished samples which ran diagonally across the predominantly a-faces, as shown in Figure 15. These domain walls, in fact, served to identify the a-faces, while the c-direction was indicated by a characteristic color pattern when viewed between crossed polarizers. Single domain samples were achieved by a combination of mechanical and electrical poling. Uniaxial stresses of 1500 to 3000psi applied along an a-axis were generally sufficient to remove all visible 90° domain walls. During application of the stress, performed using a pressurized piston, the 90° domain walls visible in the unstressed a-direction would migrate towards the corners of the crystal. This migration would create surface steps on faces along which the ends of the domain wall boundaries moved. The moving domain walls would eventually get hung-up on these surface steps so that the crystal needed to be repolished before poling could continue. After sufficient iterations all visible 90° domain walls could be removed, although a cloudiness visible in crossed polarizers revealed the presence of residual 90° domains. These were removed upon application of an applied field of 1000V/cm in an oil bath near or above the Curie temperature (128 to 133°C). Nickel electrodes were polished to optical flatness to ensure good electrical contact, and

voltage was applied slowly (10V/min) to reduce the tendency toward surface cracking at the positive electrode which occurs during rapid domain re-orientation. A typical temperature-voltage profile for electrical poling is shown in Figure 16.

Critical factors in achieving poled BaTiO₃ samples proved to be (1) having a good polish so that moving domain walls would not hang up on surface flaws, (2) using multiple iterations during mechanical poling to avoid stressing and cracking, and (3) having stress-free single-crystals. Residual stresses from cooling through the phase transition during crystal growth, or stresses induced during mechanical polishing and poling could sometimes prevent complete mechanical poling and would often cause severe cracking during electrical poling. A dramatic example is shown in Figure 17, and a graveyard of similarly destroyed crystals was generated by this process. Beware all ye who take this undertaking lightly! A list of the samples that survived for optical evaluation is given in Appendix 2.

D. Electrical Measurements

High-temperature electrical conductivity measurements were performed on BaTiO₃ single crystals as a function of temperature, oxygen-partial-pressure, and iron content. 5.5mm square plates, 0.09mm thick, were cut from high-purity, 50, 500, and 1000ppm Fe-doped crystals. Thin plates were used in order to (1) reduce the required equilibration times at lower temperatures and (2) to increase the measured

capacitance values when monitoring the cubic-to-tetragonal phase transition. The large {100} faces of these samples were polished with 3 μ m diamond paste, sputtered with platinum electrodes, and further painted with platinum paste. The samples were mounted between platinum sheet electrodes in adjacent, spring-loaded alumina sample holders shown in Figure 18. In this configuration each pair of samples shared a common ground with the pure-platinum lead of the Pt-Rh thermocouple between them.

AC complex impedance measurements were performed from 5Hz to 13MHz using a HP4192A impedance analyzer in order to separate possible electrode effects from the bulk resistivity.⁶⁸ Using this method the real conductivity was measured in the temperature range 650 to 1050°C at 50°C intervals between 1 and 10⁻⁴atm oxygen. Oxygen partial pressures in this range were controlled using premixed Ar-O₂ gases and monitored using an independent calcia-stabilized zirconia electrochemical oxygen sensor in series with the sample furnace. Equilibrium times at each temperature were based on

$$t = (l^2/\pi^2D) \ln(4c_0/\pi c) \quad (37)$$

where l is the sample thickness (cm), c is the concentrations at the center of the sample, c_0 the initial concentration at the surface ($c_0/c = 100$ for 99% equilibration), and D is the bulk diffusion coefficient of oxygen vacancies in BaTiO₃, given by Wernicke⁷⁰ as

$$D = 5700 \exp(-2.05\text{eV}/kT) \text{cm}^2/\text{s} \quad (38)$$

(Equation 37 is a conservative determination of equilibration for thin plates derived for the case of 1-dimensional diffusion out of a slab.⁶⁹) These times were confirmed experimentally by the observed equilibration of the measured electrical conductivity.

The configuration in Figure 18 was also used to determine the curie temperature of the samples. The samples used above were annealed at 800°C in P_{O_2} 's of 1, 10^{-2} , and 10^{-4} atm and subsequently quenched to above the curie temperature. Quenching was done by transferring the gas-sealed quartz-glass tube from the split-tube furnace used for annealing to an adjacent one maintained at $\sim 175^\circ\text{C}$. The phase transition was then determined by monitoring the ac capacitance (100KHz) of each sample while cooling slowly to $\sim 125^\circ\text{C}$. In each case the phase change was indicated by a sudden plunge in the relative dielectric constant from $\sim 12,000$ in the cubic phase to ~ 2000 after the transition.

E. Optical Absorption Measurements

Optical absorbance was measured using a Perkin-Elmer Lambda 9 double-beam spectrophotometer. Visible absorption spectra were measured between 380 and 860nm on as-grown and annealed samples for light polarized parallel and perpendicular to the c-axis. Automatic background correction compensated for the effects of matched polarizers and a 4mm circular beam mask (3mm mask for small or slightly

damaged samples). Mechanically-poled samples were measured before and after electrical poling. As-grown samples of high purity and doped with 5, 50, 250, 500, 750, and 1000ppm Fe were measured in the as-grown condition, while a second set of samples from boules of high-purity, 50ppm Fe, 500ppm Fe and 1000ppm Fe were measured after annealing at 800°C in oxygen (1 atm) and 100ppm O₂/Ar (10⁻⁴atm) respectively. The optical samples were annealed using the configuration in Figure 18. Crystals were heated slowly through the curie temperature (4 to 6°C/hour), and heated to 800°C in 1 hour. After annealing the samples were quenched as described above. A field of 1000V/cm was slowly applied (10V/min) and the crystals were cooled slowly through the curie temperature (4 to 6°C/hour) and then to room temperature before removing the field. It was found important to minimize the spring tension of the sample holder since stress applied to the c-axis during electrical poling could cause cracking.

Unpolarized near-infrared (NIR) absorption spectra were also measured for the same samples between 860 and 3200nm. These measurements were performed while purging the instrument in dry nitrogen at flow rates of 14 to 28 L/min in order to eliminate water vapor absorption in the ranges 1350-1450nm, 1800-1950nm, and 2520-3000nm.⁷¹ These measurements were performed for two different thicknesses (the two a-directions) for most samples in order to solve for the absorption coefficient using Equation (33).

F. Diffraction Efficiency Measurements

The photorefractive performance of electrically poled crystals was evaluated by measurements of the diffracted beam intensity as a function of time performed by my colleague, Doyle Temple. The experimental configuration was similar to that shown in Figure 10, with a 2θ value of 14 degrees. The incident intensity of the He-Ne read-out beams was the same for all measurements, but was not measured since only a relative measure of photorefractivity was required.

In an effort to minimize the ambiguities in comparing the relative diffraction efficiency of various crystals, samples were co-polished to identical thicknesses of 4.5mm \pm 3%. The important exception to this, however, was the 3mm thickness of the high purity sample, since the difficulties of preparing samples from these early, highly stressed boules prevented the fabrication of a thicker specimen. (See Appendix 1.)

IV. EXPERIMENTAL RESULTS

A. Evaluation of Sample Purity

A combination of spark-source mass spectrometry (Northern Analytical Laboratory, Amherst, New Hampshire), ultraviolet spectrophotometry, and optical absorption spectroscopy were used to confirm the impurity concentration levels in the starting materials, the purified feed, and the final undoped BaTiO₃ single crystals. The results of spark-

source mass spectrometry are listed in Table 3, and the UV spectrophotometric data and visible absorption spectra are given in Figures 19 and 20 respectively. The results of these analyses can be summarized as follows:

(1) The titanium dioxide fractional distillation procedure reduced the iron content by a factor of four and removed all other transition metals to below detection limits;

(2) UV spectrophotometric data of purified BaCO_3 and the reagent BaCl_2 precursor dissolved in HCl (Figure 19) indicate that the absorbance due to transition-metal chlorocomplexes in the BaCO_3 is significantly lower than in the BaCl_2 . The peak at 230nm in the BaCl_2 spectra corresponds well to the iron peak reported in the literature.⁷² In contrast, then, to the mass spectrometric data, which gave Fe concentrations of 0.3 and 1ppm in BaCl_2 and BaCO_3 respectively, these results indicate that the BaCO_3 purification process significantly reduced the Fe levels of the BaCl_2 precursor;

(3) Optical absorption spectra of crystals grown from (a) reagent BaCO_3 and Baker ULTREX™ TiO_2 , (b) reagent grade BaCO_3 and purified TiO_2 , and (c) purified BaCO_3 and TiO_2 synthesized in this laboratory (Figure 20) reveal that the band edge of the high-purity crystal is shifted to a slightly shorter wavelength and drops off more steeply, both indications of decreased impurity levels;

(4) Transition metal impurity levels in the high-purity BaTiO₃ single crystal are near or below the 10¹⁶/cm³ baseline (1ppma = 1.56x10¹⁶/cm³) predicted for the photorefractive effect, as indicated by mass spectrometry. Iron and nickel were measured at concentrations of 0.3 and 0.04ppm (atomic) respectively, while all other transition metals were below detection limits (0.01ppm). The only aliovalent impurities reported at levels greater than this were B (5ppm), Al (0.5ppm), and Cl, a remnant of the barium chloride precursor (10ppm). These results reveal these high purity BaTiO₃ crystals to be the purest yet achieved in this laboratory or ever used for photorefractive studies.

B. Coloration Phenomena

Unusual color bands were found to develop in heavily Fe-doped (>500ppm) crystals after prolonged high temperature annealing and electrical poling. This phenomenon was first discovered in the large, optical samples originally used for electrical conductivity measurements (pictured in Figure 18 before annealing) before it was found that their dimensions required prohibitively long equilibration times. These samples were maintained at temperatures between 700 and 1000°C in oxygen for over six days before being slowly cooled to ~135°C. A field of 700V (1200-1400V/cm) was applied for 8 hours at this temperature, and for an additional 4 hours during cooling to room temperature. All four samples were well poled upon removal from the furnace, but unusual color bands were present in the 500ppm and

1000ppm Fe-doped crystals, as shown in Figure 21. Diffuse dark brown regions were present at both electrodes. A sharper boundary divided two additional colored regions in the crystal -- a lighter yellowish region near the positive electrode, and a darker amber color toward the negative electrode.

A similar phenomenon occurred in 500, 750, and 1000ppm Fe-doped samples during electrical poling in an oil bath at temperatures near T_c . In these instances a bright yellow region developed at the positive electrode during application of the applied field, and with time the boundary of this region, which was parallel to the electrode, propagated towards the negative electrode. These coloration phenomenon were also observed by Godefroy *et al*²⁹ and caused them to abandon electrical poling procedures in their sample preparation. Fortunately for us the effect was controllable, and the color front advanced only 1 or 2 mm into the crystal in the times required for electrical poling (1 1/2 to 2 1/2 hours), leaving a large enough region for optical evaluation. No diffuse dark brown areas were formed in the oil-bath-poled samples, however, in contrast to the annealed samples. The 500 and 1000ppm Fe-doped samples are shown in Figure 22 after electrical poling.

C. Electrical Conductivity Measurements

The electrical conductivity results for pure, 50, 500, and 1000ppm Fe-doped single crystals are shown in Figures 23-26 respectively as a function of oxygen partial pressure

for nine temperatures between 650 and 1050°C. Arrhenius plots of these data comparing the conductivity of the four samples at each oxygen partial pressure are presented in Figures 27-31. In each case the symbols represent actual data points and the straight portions of the solid lines represent the best least-squares fit to the data.

The reliability of these data is substantiated by the close agreement with previously reported values. Conductivities in the "pure" sample were slightly higher than published values for undoped BaTiO_3 ,³³⁻³⁷ while the conductivity values for the 1000ppm crystal were within 2 to 4 percent of those indicated by Seuter³⁶ for 1000ppm Fe-doped ceramic BaTiO_3 .

Figures 23-26 indicate that the conductivity was p-type over the entire experimentally accessed P_{O_2} range in agreement with earlier studies. With decreasing temperature and increasing Fe content the range of linearity was extended to lower oxygen partial pressures. This behavior corresponds to a shift in the conductivity minimum to lower P_{O_2} 's as expected from Equation (15). The slopes of the pressure dependence listed in Table 4 indicate that the classical $+1/4$ dependence is achieved at the lowest temperatures and Fe contents. At higher temperatures, the conductivity minimum is shifted to higher P_{O_2} 's via Equation (15), so that an increasing n-type contribution to the total conductivity results in the shallower slopes exhibited at high temperatures in Figures 23-26 and Table 4. Increasing

the iron content has the opposite effect on the conductivity minimum, yet has the same effect of decreasing the slope below are quarter. In this case the trend a was from the $1/4$ -dependence of $\log\sigma$ vs $\log P_{O_2}$ would be due to partial transition of the Fe^{3+} to Fe^{4+} , which is characterized by a $1/6$ slope (see Figure 5, Region V.)

The isobars for all four samples in Figures 27 and 28 display two regions of linearity for the most oxidizing conditions, with a transition between 850 and 800°C. This behavior has not been previously observed since earlier studies were limited to temperatures above this range. A possible explanation is that the change in slope is indicating the onset of ionic conductivity, which would by nature be characterized by higher activation energies. For more reducing conditions (Figures 29-31) the isobars are linear at low temperatures, while curvature at high temperatures indicates the contribution of electrons to the total conductivity.⁷³ The activation energies ΔH_p , calculated from the linear regions of the $\log\sigma$ vs $1/T$ plots, are listed in Table 5. The values of 0.68 to 0.87eV for the pure sample compare favorably with values of 0.74 to 0.86eV reported for undoped single crystal $BaTiO_3$ by Eror and Smyth³³ in the P_{O_2} range 1 to 10^{-3} atm. Somewhat lower activation energies are obtained for the heavily Fe-doped crystals.

D. Curie Temperature

A typical plot of relative dielectric constant vs temperature near the curie point is shown in Figure 32. The Curie temperatures determined from this and similar plots for the pure, 50, 500, and 1000ppm Fe-doped crystals after various anneals are listed in Table 6. These results indicate that the curie temperature drops $\sim 2^\circ\text{C}$ for doping with 1000ppm Fe. This change is in excellent agreement with the results of Hagemann and Ihrig,³⁸ who reported a value of dT_c/dc of $-21^\circ\text{C}/\text{mole}\%$ for Fe-doped ceramic samples. Annealing in the oxygen partial pressure range indicated had a negligible effect on the curie temperature, again in agreement with the above workers but in sharp contrast to the results of Ducharme and Feinberg²⁶ who noted a 6°C drop in T_c for annealing in argon as compared to oxygen.

E. Optical Absorption

1. Visible Spectrum

Figures 33-38 show the absorption spectra of pure and Fe-doped BaTiO_3 single crystals in the as-grown, oxidized, and reduced conditions. In each case the absorption for light polarized with E parallel to the c-axis is given in (a) and for E perpendicular to c in (b). In the wavelength range between 400 and 860nm the absorption coefficient α was calculated from the measured absorbance using Equations (29)-(32).

Figure 32 shows the data for mechanically poled crystals over the entire iron concentration range, 0.3

("pure") to 1000ppm. A broad absorption band, extending throughout the visible to the band edge increases with increasing Fe content. In addition, the band edge itself appears to shift to higher wavelengths with increasing Fe content. The E \parallel C polarization (b) shows the emergence of a shoulder at 620nm (2.0eV) for Fe concentrations 500ppm. Figure 34 shows the spectra for the same crystals after electrical poling (except for the 50ppm sample which was already electrically poled in Figure 32). The slight decrease in the overall measured absorption indicates the removal of residual 90° domain walls during electrical poling. As mentioned previously, these domains are visible in polarized light as a cloudiness which adds to the effective measured absorbance by internal scattering of the incident beam. This observation helps resolve the inconsistencies in Figure 32: the apparent absorption of the 50ppm Fe-doped crystal drops below that of the 5ppm Fe crystal because the former was electrically poled while the latter contained residual 90° domain walls; similarly the 250ppm sample contained quite prominent domain wall boundaries which neither mechanical nor electrical poling could remove, causing it to overlap the 500ppm absorption curve. Note that at the higher absorptions near the band edge these effects are negligible, and the edge shifts monotonically with Fe-content without exception.

The effects of oxidation (1atm) and reduction (10^{-4} atm) on pure, 50, 500, and 1000ppm Fe-doped samples are shown in

Figures 34-38 respectively. Oxidation increased the height of the broad visible absorption band, turning the more heavily-doped crystals a darker brown and the lightly-doped crystals a slightly deeper yellow or amber. The effect of reduction was to drastically reduce the height of the 620nm band, changing the heavily-doped crystals from brown to yellow while leaving the high-purity crystal almost colorless.

2. *Near-Infrared Spectrum*

Some interesting and unexpected features were discovered in the NIR spectrum between 2700 and 3200nm. These results are shown in Figures 38-44. The absorbance spectra were initially corrected using Equations (32) and (33), but this method led to ambiguous results such as non-zero absorbances in very flat and clearly non-absorbing regions, and shifting and sloping baselines for different thicknesses. The absorption coefficient was instead obtained by subtracting the minimum absorbance from the entire spectrum and correcting for thickness. The success of this method is indicated by a typical spectrum shown in Figure 39, where the results for two different thicknesses yield overlapping spectra in the region of interest. Figure 39 also shows the featureless spectrum below 2800nm and the onset of the visible absorption band near 860nm.

The spectral features between 2700 and 3200nm are shown for the as-grown crystals in Figure 40. A sharp peak present at 2866nm is highest in the lightly-doped crystals

(pure, 5, 50ppm Fe) but decreases drastically with increasing Fe content and is almost completely gone in the 1000ppm Fe-doped sample. Conversely, a double-peak at 3010 and 3050nm increases steadily with increasing Fe content between 5 and 750ppm Fe. Electrical poling seemed to have little effect on this spectral region, as shown in Figure 41, except that somewhat more consistent baseline correction was achieved which alleviated the anomalously low absorption of the 1000ppm Fe sample. The feature around 2900nm is an artifact which was present in the baseline even after automatic background correction was performed, and variations in purge gas flow rate and instrument purge time were unable to eliminate its presence.

The effects of oxidation and reduction on these absorption peaks are shown in Figures 42-45. The 3010/3050nm double-peak height drops by a factor of 5-6 for the 2 heavily-doped samples upon both oxidation and reduction, while the same peaks in the pure and 50ppm crystals are totally eliminated by both annealing treatments. Similarly, the peak at 2866nm is suppressed greatly by oxidation and reduction in all samples.

F. Diffraction Measurements

Measurements of the diffracted beam intensity as a function of time are shown for pure, 50, 500, and 1000ppm Fe-doped samples in Figures 46-48 in the as-grown, oxidized, and reduced condition respectively. The as-grown crystals are very similar in photorefractive performance: the pure,

500, and 1000ppm samples have a diffracted beam intensity of $7 \pm 2 \mu\text{V}$, while that of the 50ppm sample is somewhat higher at $17\mu\text{V}$. Upon oxidation the diffracted beam intensity drops off by approximately an order of magnitude for all samples, and the grating writing time is somewhat decreased. The reduced crystals vary more systematically, with the diffracted beam intensity and saturation time increasing with increasing Fe content. For the two heavily-doped samples the diffraction efficiency increases roughly by a factor of two upon reduction relative to the as-grown condition, while for the pure and 50ppm samples an apparent decrease by the same ratio occurs.

V. DISCUSSION

A. Electrocoloration

Coloration phenomena similar to those reported in this study have been previously observed in BaTiO_3 ⁷⁴ as well as SrTiO_3 .⁷⁵ Blanc and Staebler⁷⁵ noted that the application of dc electric fields to transition-metal-doped strontium titanate in the temperature range of $\sim 100\text{-}325^\circ\text{C}$ resulted in the appearance of colored regions characteristic of oxidized material at the positive electrode and reduced material at the negative electrode. Their results were consistent with a simple model based on the drift of doubly-ionized oxygen vacancies under the influence of the applied field. This redistribution of positively-charged oxygen vacancies toward

the negative electrode caused the observed reduction of stationary transition metal ions in this region with accompanying oxidation of the transition metals at the opposite electrode. This effect was observed for all transition metals studied: Fe, Ni, Co, and Mo. By applying their analysis to our results, then, we can obtain an approximate value for the mobility of oxygen vacancies in BaTiO_3 . The rate of the color boundary movement dx/dt is related to the oxygen vacancy mobility μ_v and the applied voltage V by

$$dx/dt = \mu_v V/x \quad (39)$$

where x is the width of the untransformed region (initially the crystal length) and dx is the width of the color boundary, as shown for the 1000ppm Fe-doped sample in Figure 22. For this sample, integration of Equation (39) for $x = 0.658$ (before coloration) to 0.533cm (after coloration) and for the voltage-time profile in Figure 16 ($2.14 \times 10^4 \text{V}\cdot\text{s}$) yields a μ_v value of $\sim 3 \times 10^{-8} \text{cm}^2/\text{volt}\cdot\text{sec}$ at $\sim 128^\circ\text{C}$. This mobility compares favorably with the $1.5 \times 10^{-8} \text{cm}^2/\text{volt}\cdot\text{sec}$ value obtained by Blanc and Staebler at 200°C . More careful measurement of the color boundary migration rate was attempted *in situ* by photographing a 500ppm crystal at regular intervals during poling, but the low contrast between the two colored regions, coupled with the yellow tint of the oil bath, made it impossible to detect the location of the coloration front. Similar experiments using a more heavily-doped crystal and clearer mineral oil should

have more success, but these were abandoned in the interest of time.

While this model describes the coloration effects observed during electrical poling, it does not account for the diffuse dark brown regions present at both electrodes in the annealed samples (Figure 21). We suspect that these are due to platinum diffusion from the electrodes into the crystals exposed to high temperatures for long times. The absence of the brown regions in the pure and 50ppm crystals suggests that Fe enhances Pt interaction with the crystal. These hypotheses require further confirmation.

B. Background Acceptor Concentrations

The high-temperature electrical conductivity results in Figures 27-31 allow us to estimate the total background acceptor concentrations in these samples. These can be calculated directly from the p-type conductivity of each sample at a given P_{O_2} using Equation (11a) and values for μ_h , ΔH_p , and K_p derived from the literature. The temperature-dependent hole mobility μ_h may be given as

$$\mu_h = 4040T^{-3/2}\exp(-0.021\text{eV}/kT)\text{cm}^2/\text{V}\cdot\text{s} \quad (40)$$

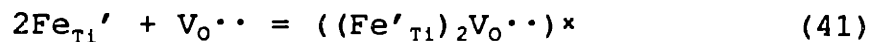
based on the expression given by Ihrig⁷⁶ for the electron mobility and the assumption^{34,37} that $\mu_h \sim \mu_e/2$. (This assumption is in good agreement with the electrical conductivity, and thermoelectric power data of Choi and Tuller⁷³ for $\text{Ba}_{0.03}\text{Sr}_{0.97}\text{TiO}_3$ and with the findings of Hagemann⁷⁷ for BaTiO_3 .) Chan et al³⁷ report a value for ΔH_p of 88.6KJ/mole (0.913eV), and manipulation of their data

yields a value for the mass-action constant K_p'' of 4.0×10^{21} $\text{MPa}^{-1/2}\text{cm}^{-3}$. Application of this analysis is reliable only for higher oxygen partial pressures (1 and 0.1atm) due to the non-linearity of the Arrhenius plots under more reducing conditions (Figures 29-31). The results for $P_{\text{O}_2} = 0.1\text{atm}$ are shown in Figure 49, indicating a very weak temperature dependence similar to that observed by Chan et al³⁷ for Al-doped BaTiO_3 . The derived acceptor concentrations in Figure 49 are replotted vs. Fe concentration in Figure 50 for the two temperature extremes. At 650°C (where the conductivity is not complicated by n-type contributions as discussed previously), total acceptor concentrations of 70, 81, 219, and 370ppm are obtained for Fe-doping levels of 0.3 (high-purity), 50, 500, and 1000ppm respectively.

The above analysis yields a rather high background acceptor concentration relative to the chemical analysis of the high purity sample. Similar background acceptor concentrations have been derived for undoped BaTiO_3 ^{34,37} (58ppm) and undoped $\text{Ba}_{0.03}\text{Sr}_{0.97}\text{TiO}_3$ ⁷³ (115ppm). The origin of these acceptors must correspond either to (1) impurities at the 70ppm level not detected by chemical analysis or (2) barium vacancies, arising from a nonstoichiometric excess of titanium, which are not electrostatically associated into neutral $V_{\text{Ba}}''V_{\text{O}}^{\bullet\bullet}$ complexes. The consequence of this derived acceptor level, whatever its origin, is that it exceeds the Fe concentration in the high-purity and 50ppm crystals and therefore controls the defect chemistry (See Section

III.A.3). This is evidenced by the difference in activation energies ΔH_p between these and the more heavily-doped samples (Figures 27-31, discussed previously).

In addition, Figure 50 indicates that the added Fe is only 30% effective as an acceptor. This unexplained disparity was observed by Chan *et al*³⁷ for added aluminum, which also was only 30% effective as an acceptor. One possible explanation may be that in fact only 30% of the Fe dopant in the melt goes into the crystal, but this is highly unlikely due to (1) the excellent agreement of the conductivity values with the data of Seuter³⁶ for 1000ppm Fe-doped BaTiO₃ ceramic and (2) the distribution coefficient for Fe in BaTiO₃, reported by Godefroy *et al*⁶⁷. An alternative explanation is that a considerable portion of the trivalent iron ions are electrostatically associated with oxygen vacancies into uncharged complexes by the reaction



Although this possibility was discarded by Chan *et al*, the ESR data of Hagemann⁴¹ shows a significant part of the Fe³⁺ acceptors to be associated with oxygen vacancies as nearest neighbors which is likely to influence the formation and an annihilation of vacancies. In fact, the incorporation of associate formation into the defect model would improve the consistency of Mossbauer and thermogravimetric results on Fe-doped BaTiO₃.⁷⁷

C. Interpretation of Absorption Spectra

1. Visible Absorption

Interpretation of the visible absorption spectra for oxidized and reduced $\text{BaTiO}_3\text{:Fe}$ is somewhat straight forward. Based on the previous identification of charge transfer bands in SrTiO_3 , on the theoretically allowed Fe transitions, and on the observed Fe-concentration and P_{O_2} -dependent trends, the broad absorption band in the visible is undoubtedly an Fe^{4+} charge transfer band. The 620nm (2.0eV) shoulder visible in the E1c polarized spectrum corresponds to the 590nm (2.1eV) Fe^{4+} peak in SrTiO_3 (Figure 9) shifted to slightly longer wavelength due to differences in the crystal field strength. The analog to the 443nm (2.8eV) peak in the SrTiO_3 spectrum occurs at absorbances out of range for the spectrometer for the sample thicknesses used (3-4.5mm), and probably explains the apparent shifts in the band edge with increasing Fe content plotted in Figure 51.

Qualitatively, the interpretation above conforms well with the proposed defect model. In the as-grown condition the Fe ions are present in both the trivalent and quadrivalent state, and the relative concentration of Fe^{4+} increases with increasing iron content as given by Equation (24). This manifests itself as a non-linear increase in the 620nm absorption peak with increasing Fe content observed in Figures 32 and 34. Upon oxidation, more of the Fe^{3+} is converted to Fe^{4+} , and vice-versa upon reduction, resulting

in the trends seen in Figures 35 thru 38. It is also significant to note that no absorptions corresponding to Fe^{2+} (825 to 1030nm in SrTiO_3) were observed even for the most reducing conditions investigated, in keeping with the defect model's prediction that the Fe^{2+} concentration is below $10^{15}/\text{cm}^3$ for even the most heavily-doped crystals in the P_{O_2} range (see Figure 7).

Quantitatively, the Fe-concentration dependence and oxygen-partial-pressure dependence of the 620nm absorption deviates somewhat from Fe^{4+} concentration behavior predicted by the defect model, but the fit improves with increasing iron content. According to the defect chemical model, the $[\text{Fe}^{4+}]$ should increase one order of magnitude for every two orders of magnitude increase in the total iron concentration $[\text{Fe}]_{\text{tot}}$, i.e.,

$$d \log [\text{Fe}^{4+}] / d \log [\text{Fe}]_{\text{tot}} = 0.5 \quad (42)$$

A plot of $\log \alpha_{620}$ vs $\log [\text{Fe}]$, shown in Figure 52, shows an overall slope of only 0.29 using linear regression. It can be seen from this Figure, however, that the slope is trending toward one-half at higher concentrations. Similar behavior is observed in the plot of $\log \alpha_{620}$ vs $\log \text{P}_{\text{O}_2}$, Figure 53. At low iron concentrations very little P_{O_2} -dependence is observed. With increasing Fe content, however, the linearity of the data steadily improves, and the theoretical $1/4$ dependence is very nearly achieved in the 1000ppm Fe-doped sample.

2. Near Infrared Features

The interpretation of features in the near infrared is somewhat more troublesome than that of the visible spectrum. No features corresponding to the 3010/3050nm double peak have been reported in any previous studies of BaTiO₃ or SrTiO₃. In addition, the erratic P_{O2}-dependence of these features does not conform to the behavior of any species in the defect model. The one thing that is clear, however, is that the behavior of these absorptions is somehow linked to the presence of iron.

The strongest dependence on iron concentration is exhibited by the double peak centered at 3030nm. If the spectra in Figure 40 are replotted vs energy, the peak area (which is a more reliable measure of concentration than α due to the problems of baseline correction) is linearly related to the Fe concentration up to 750ppm, as shown in Figure 54. The area of the 2866nm peak, determined in the same way, is less consistent but generally decreases with increasing Fe content. The P_{O2}-dependence of both features is somewhat puzzling, in that both oxidation and reduction reduce the features by almost the same magnitude.

The most likely explanation is that both features are related to OH⁻ ions introduced into the crystals during growth. These have been identified in as-grown LiNbO₃ by an absorption at 2.88 μ .^{7,9} Ducharme and Feinberg²⁶ likewise assigned this peak in their spectrum to a hydrogen-like center, and the peak heights and widths in both cases are in

agreement with the 2866nm peak in this study. The 3010/3050nm peaks, then, would correspond to an Fe-OH complex. With increasing iron concentration more and more of the OH⁻ is associated with localized Fe ions, resulting in a decrease of the isolated OH⁻ peak at 2866nm at the expense of the 3010/3050nm absorption of the iron hydroxide species. The saturation of the double peak height between 750 and 1000ppm Fe (Figure 41) coincides with the disappearance of the 2866nm peak, indicating complete association of the OH⁻ with Fe ions. During the first high temperature annealing in dry, flowing gases, much of the OH⁻ is believed to diffuse out of the samples, explaining the depression of all the observed features and the absence of any additional changes upon a second annealing in a reducing atmosphere.

D. Interpretation of Photorefractive Behavior

Although the preliminary characterizations of photorefractive behavior in this study are far too crude to allow for conclusive identification of the photorefractive species in BaTiO₃, the general Fe-concentration and P_{O₂}-dependent trends of the data serve the purposes of our initial strategy.

First of all, the high purity crystal exhibited photorefractivity despite transition-metal-impurity levels below the proposed $10^{16}/\text{cm}^3$ baseline. According to Figure 7, the defect-chemical model predicts an Fe²⁺ concentration on the order of only $\sim 10^{12}/\text{cm}^3$ for the as-grown crystal, which

is four orders of magnitude lower than any trap densities reported in the literature for nominally undoped BaTiO₃. The diffracted beam intensity, as well as other measurements reported elsewhere ⁷⁸ indicate that the strength of the photorefractive effect in this undoped crystal is comparable to these. It therefore appears that the popular model in which Fe²⁺ is the photorefractive trap site does not appear to apply in this case.

Secondly, the photorefractive effect does not scale with Fe concentration in the doped crystals. According to Figure 45, variations in Fe concentration spanning well over 3 orders of magnitude have little effect on the holographic diffraction efficiency of the as-grown crystals. Similarly small and non-systematic variations are exhibited in the oxidized samples. Even in the reduced specimens, which have similar absorptions and display systematic increase in diffraction efficiency with Fe content, the effect varies by less than a factor of 10 over the entire doping range, whereas the relative concentration of Fe²⁺ should increase by 1¹/₂ to 2 orders of magnitude in this span.

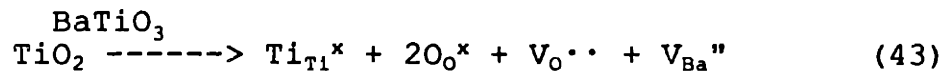
The effects of Fe valence on the photorefractive performance of BaTiO₃ can be deduced from variations in the maximum diffraction efficiency with P_{O₂} plotted in Figure 55. The uniform decrease in diffraction efficiency upon annealing in oxygen coincides for all samples with an increase in the 620nm Fe⁴⁺ absorption peak. Increases in the diffraction efficiency of the heavily doped samples

after reduction correspond to further substantial decreases in Fe^{4+} absorption. Thus Fe^{4+} centers do not appear to be involved in the generation or trapping of photorefractive charge carriers, but instead contribute background absorption which hinders the photorefractive efficiency. The apparent drop in the diffracted beam intensity for Fe concentrations $>50\text{ppm}$ in oxidizing atmospheres may be due simply to absorption of the diffracted beam in these darker crystals.

Except for the low concentration levels of Fe^{2+} , the P_{O_2} -dependent trends in Figure 55 are not entirely inconsistent with the $\text{Fe}^{2+}:\text{Fe}^{3+}$ photorefractive model, for the $1/4 \text{P}_{\text{O}_2}$ -slope-dependence of the Fe^{2+} concentration is approached by the changes in diffraction efficiency at higher Fe concentrations and lower P_{O_2} 's. The observed decrease in the efficiency of the pure and 50ppm crystals after reduction nonetheless requires a different interpretation.

It would be dangerous to elaborate any detailed model for the identity of photorefractive species in BaTiO_3 based on the relatively small changes in photorefractive behavior determined by these experiments for crystals with various Fe concentrations and oxidation states. It is clear, however, that the magnitude of the observed variations in diffraction efficiency does not reflect the wide variations in Fe content of the crystals which were investigated. Nothing even close to the 1000-fold increase reported by Godefroy et al^{28,29} was evidenced in the heavily-doped crystals, nor did

the photorefractive performance of the high-purity crystal drop much below that of more heavily-contaminated commercial samples. Thus it appears that Fe is not the dominant photorefractive species in BaTiO₃. If multivalent Fe impurities are indeed not the cause of the photorefractive effect, then another explanation is needed. The picture proposed by Ducharme and Feinberg²⁶ involves oxygen and barium vacancies, presumably generated by the titanium excess in melt-grown crystals by the reaction



In this model, barium vacancies would exist as a P_{O₂}-independent source of electron traps, while the concentration of oxygen vacancies, which act as photorefractive electron donors, would vary with P_{O₂}. This interpretation has major drawbacks as well, however. First is the fact that oxygen vacancies are extremely shallow donors which should be fully ionized at room temperature. Secondly, all defect chemical investigations of BaTiO₃ (with which the conductivity results here agree) have indicated that the [V₀^{··}] is extrinsically controlled, i.e. P_{O₂}-independent, over an extremely wide range of oxygen partial pressure. Thus a new model, is required to explain the source or the photorefractive properties of BaTiO₃. Only further systematic studies of the defect properties of BaTiO₃ in correlation with the photorefractive properties will enable a clearer image to emerge.

VI. CONCLUSIONS

This work represents the first study in which both the Fe concentration and oxidation state of single crystal BaTiO_3 have been systematically controlled and correlated with its photorefractive properties. Purified starting materials were synthesized by various chemical means to lower transition-metal impurity levels below the $10^{16}/\text{cm}^3$ baseline estimated for photorefractivity. High purity BaTiO_3 single crystals were grown from this material, as well as Fe-doped crystals with concentrations of 5, 50, 250, 500, 750, and 1000ppm Fe. These crystals were characterized by high-temperature electrical conductivity and optical absorption measurements in the P_{O_2} range from 1 to 10^{-4}atm . The results are consistent with the predictions of a quantitative defect-chemical model, based on published equilibrium constants and activation energies, which is presented here in detail to interpret the Fe-concentration and P_{O_2} -dependent changes in iron valence. Based on preliminary photorefractive evaluation of high-purity and Fe-doped BaTiO_3 before and after oxidation and reduction, it appears that Fe is not the dominant photorefractive species in barium titanate.

VII. RECOMMENDATIONS

The very nature of this project requires that further research be done on the evaluation of photorefractive properties. A major thrust of this effort was to provide well characterized material in terms of impurity-levels, dopant concentrations, and oxidation state of BaTiO_3 single crystals. The relatively crude holographic diffraction efficiency measurements reported here are only preliminary indications of the role that Fe impurities and their valence states play in controlling the photorefractive effect in barium titanate. It is expected, however, that the defect-chemical model and spectroscopic results presented here will aid in the interpretation of future work.

Primary among these future investigations should be the acquisition of more reliable photorefractive data. The simplest of these experiments, perhaps, would be anisotropic $(E||c)$ diffraction efficiency measurements which satisfy the assumptions required of Equation (35). These would allow for corrections in absorption and thickness to be made among various crystals and thus yield a more reliable comparison. More quantitative results could be obtained, including the determination of photorefractive trap densities and carrier sign, using the two-beam energy coupling and grating decay measurements described in references 25 and 26. The advantage of these latter techniques is that they are less

sensitive to the presence of 180° domains which are so difficult to characterize.

In addition to improved photorefractive evaluation, further control and characterization of the Fe valence states in these samples is in order. The most obvious experiments would be to extend optical spectroscopy measurements to samples annealed over a wider oxygen partial pressure range. Oxygen partial pressures as low as 10^{-25} atm are easily attainable with CO/CO₂ gas mixtures. (Even lower P_{O₂}'s could conceivably be achieved by H₂ annealing, but this would make the actual pressure control difficult as well as complicate the spectra by the introduction of hydrogen.) At these low pressures significant amounts of Fe²⁺ could be generated, and its effect on the photorefractive carrier density could be evaluated by measurements on these more heavily reduced crystals. In addition to the relatively thick samples required for photorefractive measurements, thinner samples would allow the characterization of more highly absorbing features, especially near the band edge (see Figure 9).

An intriguing means of controlling the Fe valence state which was not taken advantage of in this study suggests still further possibilities for continued research. So-called "electrooxidation" and "electroreduction" of crystals under an applied field at temperatures near T_c had visible effects on the valence state of Fe ions near the electrodes, with the width of the affected regions varying

with time. Such electrochemical manipulation of optical samples may yield higher concentrations of certain valence states and native defects than those achievable by high-temperature annealing. This technique has the added advantage that crystals do not need to be cycled through the curie temperature. Exposure to high electric fields for extended times may also serve to improve the degree of poling. Electrocoloration experiments can also be used to determine important materials parameters for BaTiO_3 . Using the methods detailed in reference 75, one can obtain quantitative determinations of oxygen vacancy mobilities and concentrations, defect concentrations, and defect activation energies.

Finally, the difficulties encountered in crystal growth and single-domain optical sample preparation suggest the need for improved processing, especially if BaTiO_3 is to be an important photorefractive material in the future. Preparation of feed material from purified precursors offers improvement in reproducibility and reliability. Alterations in the growth technique could serve to minimize residual stresses, and efforts to electrically pole single-crystal boules before cooling through the tetragonal phase transition might save countless man-hours of sample preparation and yield more completely poled crystals.

REFERENCES

1. A. Ashkin, et al, Applied Physics Letters, **9(1)**, 72 (1966).
2. V.V. Shkunov and B.Y. Zel'dovich, Scientific American, p.54, December 1985.
3. D.M. Pepper, Scientific American, p.74, January 1986.
4. F.S. Chen, Journal of Applied Physics, **40(8)**, 3389 (1969).
5. A.M. Glass, D. von der Linde, and T.J. Negran, Applied Physics Letters, **25(4)**, 233 (1974).
6. H.J. Levinstein et al, Journal of Applied Physics, **38(6)**, 3101 (1967).
7. R.G. Smith et al, Journal of Applied Physics, **39(10)**, 4600 (1968).
8. G.E. Peterson and J.R. Carruthers, Journal of Solid State Chemistry, **1**, 98 (1969).
9. G.E. Peterson, A.M. Glass, and T.J. Negron, Applied Physics Letters, **19(5)**, 130 (1971).
10. G.E. Peterson, A.M. Glass, A. Carnevale, and P.M. Bridenbaugh, Journal of the American Ceramic Society, **56(5)**, 278 (1973).
11. D.L. Nash, Applied Spectroscopy, **27(2)**, 132 (1973).
12. M.G. Clark, F.J. DiSalvo, A.M. Glass, and G.E. Peterson, Journal of Chemical Physics, **54(12)**, 6209 (1973).
13. A.M. Glass, G.E. Peterson, and T.J. Negran, in "Laser Induced Damage in Optical Materials" (A.J. Glass and A.H. Guenther, eds.) pp.15-26, Nat. Bur. Stand. Spec. Publ. 372, 1972.
14. J.J. Amodei, W. Phillips, and D.L. Staebler, Applied Optics, **11(2)**, 390 (1972).
15. D.L. Staebler and W. Phillips, Applied Optics, **13(4)**, 788 (1974).
16. W. Phillips and D.L. Staebler, Journal of Electronic Materials, **3(2)**, 601 (1974).
17. A.M. Glass, Optical Engineering, **17(3)**, 470 (1978).

18. H. Kurz et al, Applied Physics, **12**, 355 (1977).
19. G.C. Valley and M.B. Klein, Optical Engineering, **22**(6), 704 (1983).
20. P. Gunter, Physics Reports, **93**(4), 199 (1982).
21. F. Micheron and G. Bismuth, Applied Physics Letters, **20**(2), 79 (1972).
22. F. Micheron and G. Bismuth, Applied Physics Letters, **23**, 71 (1973).
23. J.P. Remeika, Journal of the American Chemical Society, **76**, 940 (1954).
24. M.B. Klein and G. C. Valley, Journal of Applied Physics, **57**(11), 4901 (1985).
25. M.B. Klein and R.N. Schwartz, Journal of the Optical Society of America B, **3**(2), 293 (1986).
26. S. Ducharme and J. Feinberg, *ibid.*, p. 283.
27. Sanders Associates, Nashua, N.H.
28. G. Godefroy, G. Ormancey, P. Jullien, Y. Semanou, W. Ousi-Benommar, 1986 IEEE International Symposium on Applications of Ferroelectrics (ISAF), June 8-11, Lehigh University, Bethlehem. PA., paper PA-1.
29. G. Ormancey, P. Jullien, W. Ousi-Benommar, Y. Semanou, P. Lompre, Y. Beaucamps, and G. Godefroy, Proceedings of IMFG, Kobe' 1985, Japanese Journal of Applied Physics, **24**, Suppl. 24-2, 293-295 (1985).
30. J. Feinberg, D. Heiman, A.R. Tanguay, Jr., and R.W. Hellworth, Journal of Applied Physics, **51**(3), 1297 (1980).
31. S.A. Long and R. N. Blumenthal, Journal of the American Ceramic Society, **54**(10), 515 (1971).
32. *ibid.*, **54**(11), 577 (1971).
33. N.G. Eror and D. M. Smyth, Journal of Solid State Chemistry, **24**, 235 (1978).
34. N.-H. Chan, R.K. Sharma, and D.M. Smyth, Journal of the American Ceramic Society, **64**(9), 556 (1981).
35. N.-H. Chan and D. M. Smyth, Journal of the Electrochemical Society, **123**(10), 1584 (1976).

36. A.M.J.H. Seuter, Philips Research Reports Supplement, **3** (1974).
37. N.-H. Chan, R.K. Sharma, and D.M. Smyth, Journal of the American Ceramic Society, **65**(3), 167 (1982).
38. H.-J. Hagemann and H.Ihrig, Physical Review B, **20**(9), 20 (1979).
39. H.-J. Hagemann, A. Hero, and U. Gonser, Physical Status Solidi (a) **61**, 63 (1980).
40. H.-J. Hagemann and D. Hennings, Journal of the American Ceramic Society, **64**(10), 590(1981).
41. H.-J. Hagemann, "Akzeptorionen in BaTiO₃ und SrTiO₃ und ihre Auswirkung auf die Eigenschaften von Titanat Keramiken," Ph.D. Thesis, Rheinisch-Westfalische Technische Hochschule Aachen, Federal Republic of Germany, 1980.
42. F.A. Kroger and H.J. Vink, in *Solid State Physics*, Vol.3, F. Seitz and D. Turnbull (eds.), Academic Press, New York, p. 307 (1956).
43. J.S. Griffith, in *The Theory of Transition-Metal Ions*, University Press, Cambridge, U.K., pp. 260-263 (1961).
44. S. R. Rotman, "Defect Structure of Luminescent Garnets," Ph.D. Thesis, Massachusetts Institute of Technology, Cambridge, MA, September 1985.
45. S. Ikegami, I. Ueda, and Y. Ise, Journal of the Physical Society of Japan, **16**, 572 (1961).
46. S.Ikegami and I. Ueda, *ibid.*, **19**(2), 159 (1964).
47. C.N. Berglund and H.J. Braun, Physical Review, **164**(2), 790 (1967).
48. E.V. Bursian, Y.G. Girshberg, and E.N. Starov, Physical Status Solidi (b) **46**, 529 (1971).
49. M.S. Kozyreva and N.B. Arzheukhova, Izvestiya Akademii Nauk SSSR **11**(7), 1280 (1975).
50. M. Didomenico, Jr., and S.H. Wemple, Physical Review **166**, 565 (1968).
51. S.H. Wemple, M. Didomenico, Jr., and I. Camlibel, Journal of Physics and Chemistry of Solids **29**, 1797 (1968).
52. A. Linz, V. Belruss, and C.S. Naiman, Journal of the Electrochemical Society **112**, 60C (1965).

53. H.W. Gandy, *Physical Review* **113**(3), 795 (1959).
54. B.W. Faughnan, *Physical Review B*, **4**(10), 3623 (1971).
55. R. L. Wild, E. M. Rockar, and J.C. Smith, *Physical Review B*, **8**(8), 3828 (1973).
56. W. D. Kingery, H. K. Bowen, and D. R. Uhlmann, *Introduction to Ceramics*, 2nd Ed., John Wiley & Sons, NY (1976).
57. J.I. Pankove, *Optical Processes in Semiconductors*, Dover Publications, Inc., NY (1971).
58. D.L. Dexter, *Physical Review B*, **101**(1), 48 (1956).
59. H. Kogelnik, *Bell System Technical Journal* **48**, 2909 (1969).
60. Compiled from D.C. Bradley, R.C. Mehotra, and D.P. Gaur, *Metal Alkoxides*, Ch.3, Academic Press, London (1978).
61. *Laboratory Techniques Manual*, Vol.1, Undergraduate Chem. Lab., M.I.T. (1974).
62. K.B. Wiberg, *Laboratory Technique in Organic Chemistry*, McGraw Hill, NY, 1-74 (1960).
63. E.S. Perry and A. Weissberger (eds.), *Technique of Organic Chemistry*, Vol.IV, Interscience, NY (1965).
64. D.J. Epstein, A. Linz, D.R. Gabbe, and N. Rhodes, Rome Air Development Center Technical Report No. 78-141, June 1978.
65. D.R. Gabbe, *Materials Science Forum*, **5**, 87 (1985).
66. V. Belruss, J. Kalnajs, and A. Linz, *Materials Research Bulletin* **6**, 899 (1971).
67. G. Godefroy, D. Lompre, and C. Dumas, *ibid.*, **12**, 165, (1977).
68. J.E. Bauerle, *Journal of Physics and Chemistry of Solids*, **30**, 2657 (1967).
69. P. G. Shewmon, *Diffusion in Solids*, J. Williams Book Co., Jenks, OK, p. 16 (1983).
70. R. Wernicke, *Philips Research Reports*, **31**, 526 (1976).
71. *Operator's Manual*, Lambda 9 UV/VIS/NIR Spectrometer, Perkin Elmer, West Germany (1985).

72. A. Glasner and P. Avinur, *Talanta*, **11**, pp. 679, 761, 775 (1964).
73. G.M. Choi and H.L. Tuller, paper submitted to the *Journal of the American Ceramic Society*, February, 1986.
74. M.S. Kosman and E.V. Bursian, *Soviet Physics Doklady*, **2**, 354 (1957).
75. J. Blanc and D.L. Staebler, *Physical Review B*, **4**(10), 3548 (1971).
76. H. Ihrig, *Journal of Physics C*, **9**, 3469 (1976).
77. H.-J. Hagemann, personal communication.
78. P.G. Schunemann, D.A. Temple, R.S. Hathcock, H.L. Tuller, H.P. Jenssen, D.R. Gabbe, and C. Warde, presented at the 1987 Conference on Lasers and Electro-Optics (CLEO '87), paper no. 0120.

FIGURES AND TABLES

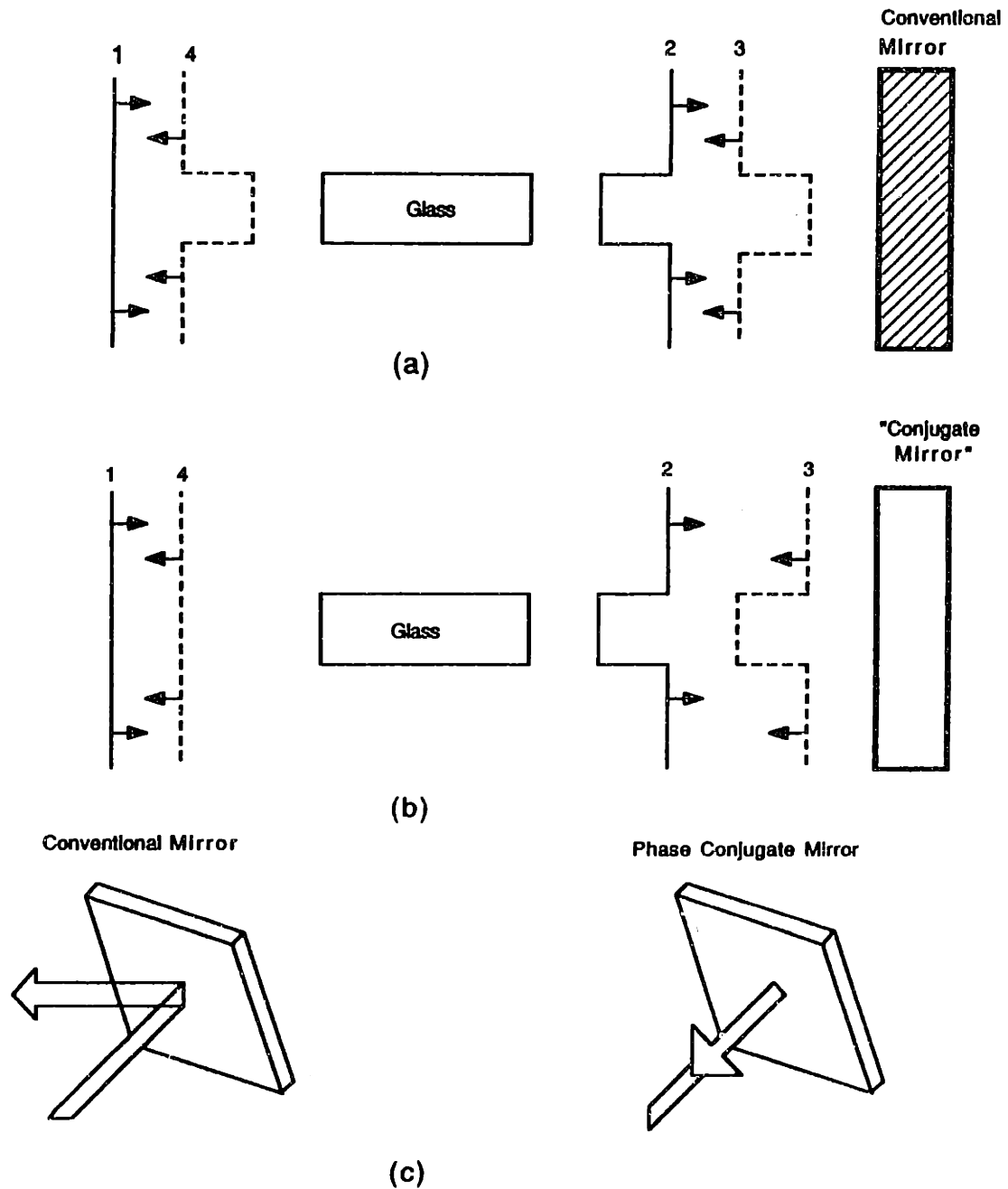


Figure 1. Difference between the reflections of a conventional mirror and a phase conjugate mirror.

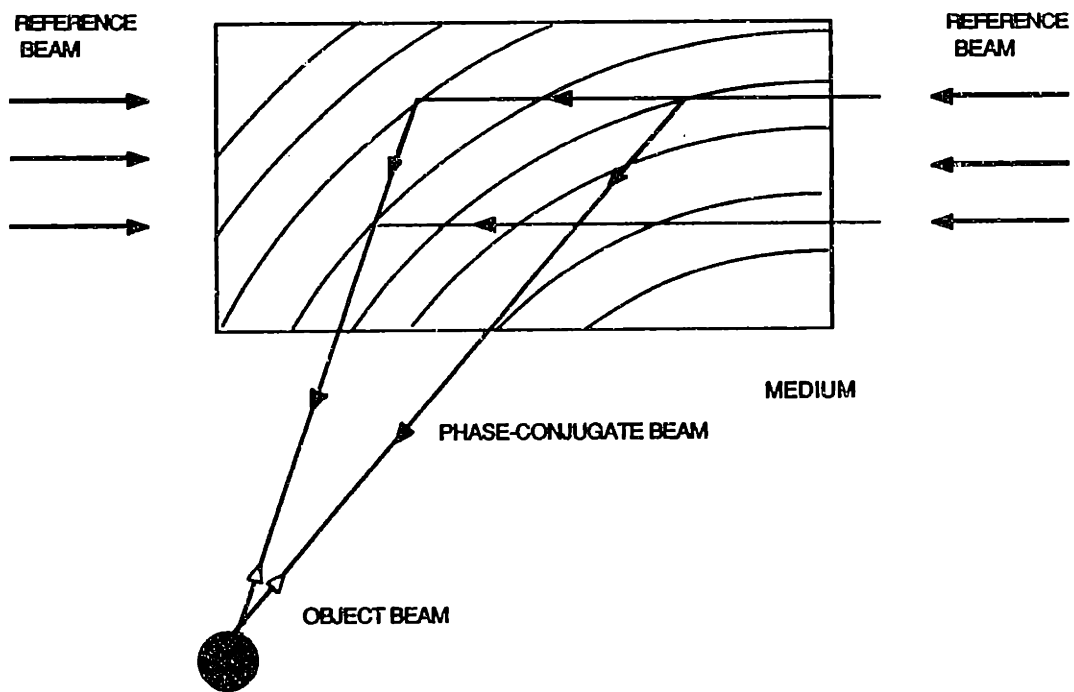
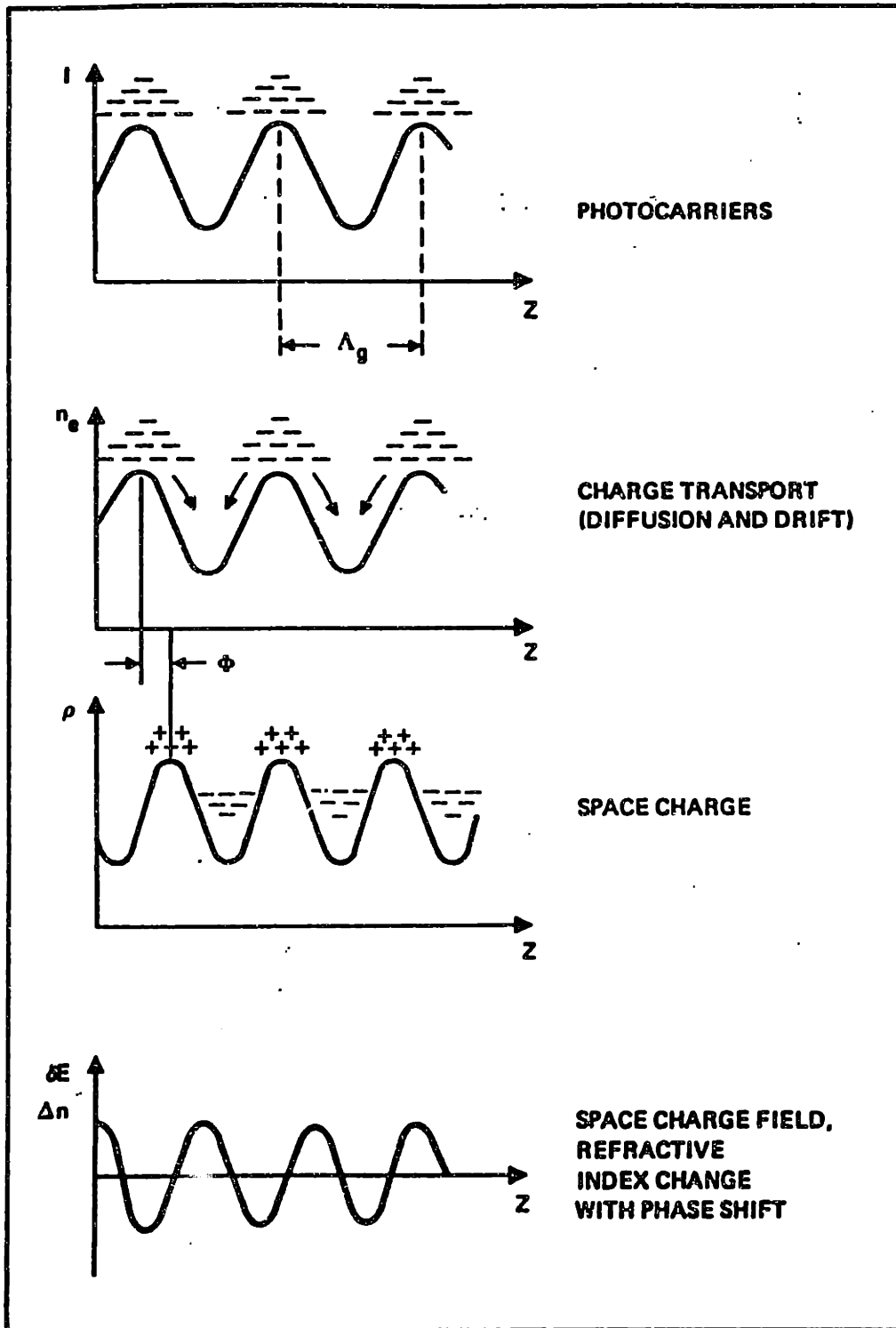


Figure 2. Phase conjugation by four-wave mixing in a photorefractive crystal. (from reference 2)



(a)

Figure 3. Model for the photorefractive effect. (a) Generation of refractive index gratings. (b) Sources and traps for photorefractive charge carriers. (from reference 19)

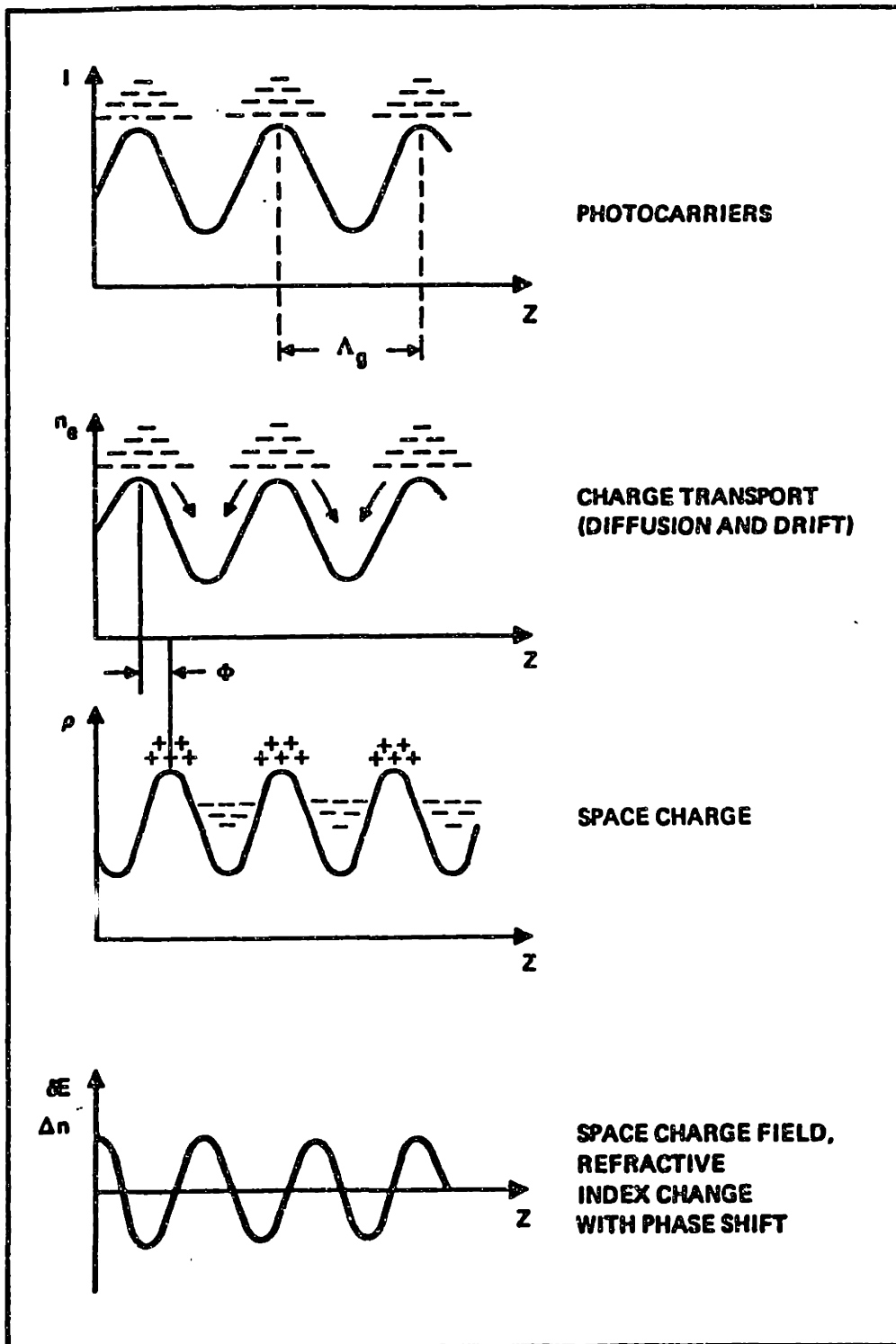
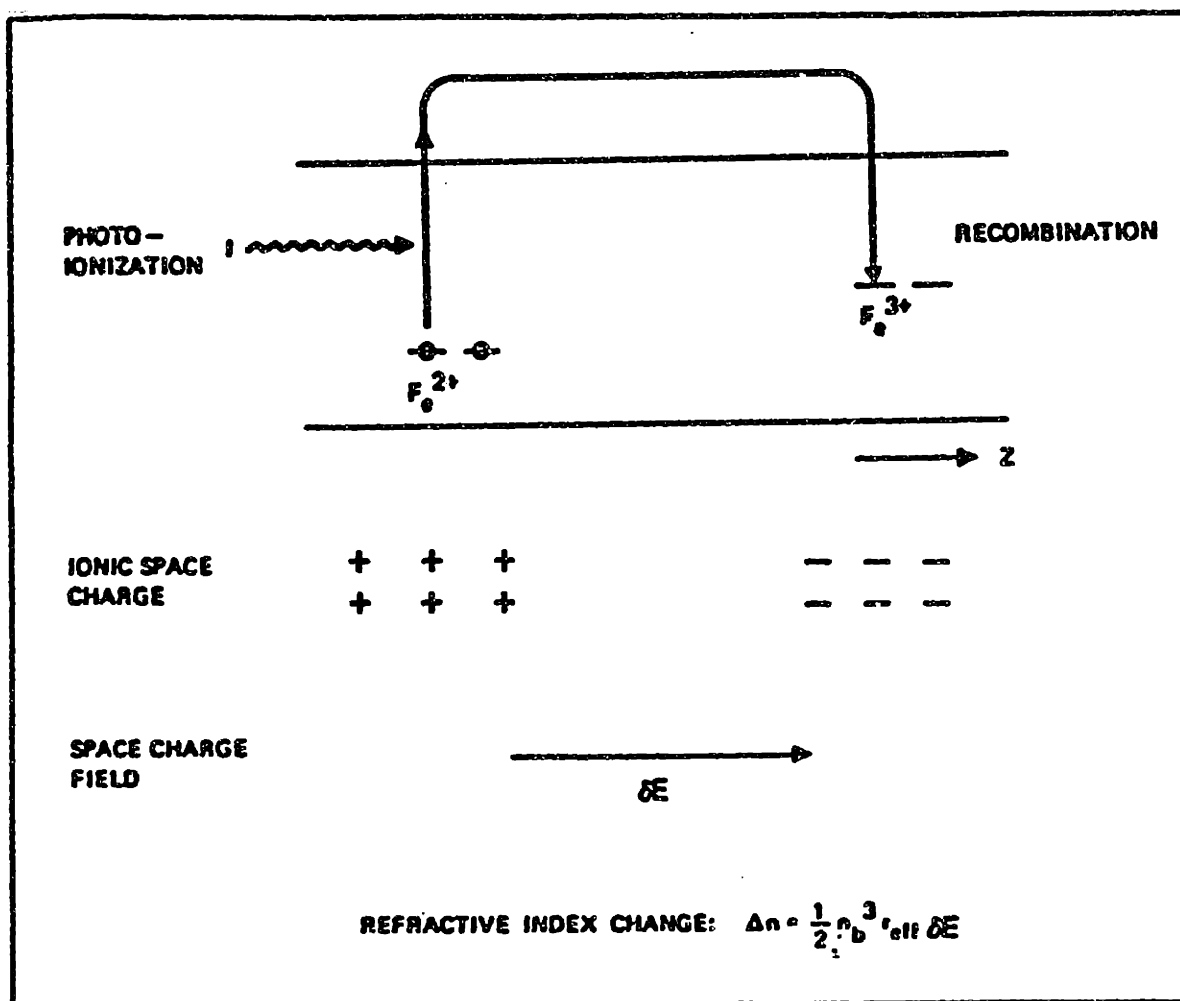


Figure 3. Model for the photorefractive effect. (a) Generation of refractive index gratings. (b) Sources and traps for photorefractive charge carriers. (from reference 19)



(b)

Table 1. Defect-chemical relations for variable valent acceptor-doped BaTiO₃ for seven P_{O2}-dependent defect regimes (plotted schematically in Figure 5).

	I	II
	$n = 2[\text{Vo}\cdot\cdot]$	$[\text{Fe}_{\text{Ti}}''] = [\text{Vo}\cdot\cdot]$
	$[\text{Fe}_{\text{Ti}}''] = [\text{Fe}_{\text{Ti}}]_{\text{tot}}$	$[\text{Fe}_{\text{Ti}}''] = [\text{Fe}_{\text{Ti}}]_{\text{tot}}$
$[\text{Fe}_{\text{Ti}}'']$	$[\text{Fe}_{\text{Ti}}]_{\text{tot}}$	$[\text{Fe}_{\text{Ti}}]_{\text{tot}}$
$[\text{Fe}_{\text{Ti}}']$	$K_D'' [\text{Fe}_{\text{Ti}}]_{\text{tot}} \text{P}_{\text{O}_2}^{1/6}$ $4^{1/6} K_n^{1/3}$	$K_D'' [\text{Fe}_{\text{Ti}}]_{\text{tot}}^{3/2} \text{P}_{\text{O}_2}^{1/4}$ $K_n^{1/2}$
$[\text{Vo}\cdot\cdot]$	$K_n^{1/3} \text{P}_{\text{O}_2}^{-1/6}$ $4^{-1/3}$	$[\text{Fe}_{\text{Ti}}]_{\text{tot}}$
n	$4^{1/6} K_n^{1/3} \text{P}_{\text{O}_2}^{-1/6}$	$K_n^{1/2} \text{P}_{\text{O}_2}^{-1/4}$ $[\text{Fe}_{\text{Ti}}]_{\text{tot}}^{1/2}$
p	K_1 $4^{-1/6} K_n^{1/3} \text{P}_{\text{O}_2}^{1/6}$	$K_1 [\text{Fe}_{\text{Ti}}]_{\text{tot}} \text{P}_{\text{O}_2}^{1/4}$ $K_n^{1/2}$
III		
	$2[\text{Fe}_{\text{Ti}}''] + [\text{Fe}_{\text{Ti}}'] = 2[\text{Vo}\cdot\cdot]$	
	$[\text{Fe}_{\text{Ti}}'] = [\text{Fe}_{\text{Ti}}]_{\text{tot}}$	
$[\text{Fe}_{\text{Ti}}'']$	$[\text{Fe}_{\text{Ti}}]_{\text{tot}} \text{P}_{\text{O}_2}^{-1/6}$ $K_D' 2^{2/3} K_n^{1/3}$	
$[\text{Fe}_{\text{Ti}}']$	$[\text{Fe}_{\text{Ti}}]_{\text{tot}}$	
$[\text{Vo}\cdot\cdot]$	$[\text{Fe}_{\text{Ti}}]_{\text{tot}} \text{P}_{\text{O}_2}^{-1/6}$ $K_D' 2^{2/3} K_n^{1/3}$	
n	$K_D''^{1/3} \text{P}_{\text{O}_2}^{-1/6}$ $[\text{A}_{\text{Ti}}']^{1/3} K_n^{1/3}$	
p	$K_1 [\text{A}_{\text{Ti}}']^{1/3} K_n^{1/3} \text{P}_{\text{O}_2}^{1/6}$ $K_D''^{1/3}$	

	IV	V
	$[\text{Fe}_{\text{T}_1}'] = 2[\text{Vo}\cdot\cdot]$	$[\text{Fe}_{\text{T}_1}'] = 2[\text{Vo}\cdot\cdot]$
	$[\text{Fe}_{\text{T}_1}'] = [\text{Fe}_{\text{T}_1}]_{\text{tot}}$	$[\text{Fe}_{\text{T}_1}^*] = [\text{Fe}_{\text{T}_1}]_{\text{tot}}$
$[\text{Fe}_{\text{T}_1}^*]$	$\frac{K_D' [\text{Fe}_{\text{T}_1}]_{\text{tot}}^{3/2} \text{PO}_2^{1/4}}{2^{1/2} K_n^{1/2}}$	$[\text{Fe}_{\text{T}_1}]_{\text{tot}}$
$[\text{Fe}_{\text{T}_1}']$	$[\text{Fe}_{\text{T}_1}]_{\text{tot}}$	$\frac{2^{1/3} [\text{Fe}_{\text{T}_1}]_{\text{tot}}^{2/3} \text{PO}_2^{-1/6}}{K_D' 2^{2/3} K_n^{1/3}}$
$[\text{Vo}\cdot\cdot]$	$\frac{[\text{Fe}_{\text{T}_1}]_{\text{tot}}}{2}$	$\frac{[\text{Fe}_{\text{T}_1}]_{\text{tot}}^{2/3} \text{PO}_2^{-1/6}}{2^{2/3} K_D' 2^{2/3} K_n^{1/3}}$
n	$\frac{2^{1/2} K_n^{1/2} \text{PO}_2^{-1/4}}{[\text{Fe}_{\text{T}_1}]_{\text{tot}}^{1/2}}$	$\frac{2^{1/3} K_D' 1/3 \text{PO}_2^{-1/6}}{[\text{Fe}_{\text{T}_1}]_{\text{tot}}^{1/3} K_n^{1/3}}$
p 1/2	$\frac{K_1 [\text{Fe}_{\text{T}_1}]_{\text{tot}} \text{PO}_2^{1/4}}{2^{1/3} K_D' 1/3}$	$\frac{K_1 [\text{Fe}_{\text{T}_1}]_{\text{tot}}^{1/3} K_n^{1/3} \text{PO}_2^{1/6}}{2^{1/2} K_n}$

	VI	VII
	$2[\text{Vo}\cdot\cdot] = [\text{A}_{\text{T}_1}']$	$[\text{A}_{\text{T}_1}'] = P$
	$[\text{Fe}_{\text{T}_1}^*] = [\text{Fe}_{\text{T}_1}]_{\text{tot}}$	$[\text{Fe}_{\text{T}_1}^*] = [\text{Fe}_{\text{T}_1}]_{\text{tot}}$
$[\text{Fe}_{\text{T}_1}^*]$	$[\text{Fe}_{\text{T}_1}]_{\text{tot}}$	$[\text{Fe}_{\text{T}_1}]_{\text{tot}}$
$[\text{Fe}_{\text{T}_1}']$	-----	-----
$[\text{Vo}\cdot\cdot]$	$[\text{A}_{\text{T}_1}'] / 2$	$([\text{A}_{\text{T}_1}'] K_n / K_1^2) \text{PO}_2^{-1/2}$
n	$(2K_n / [\text{A}_{\text{T}_1}'])^{1/2} \text{PO}_2^{-1/4}$	$K_1 / [\text{A}_{\text{T}_1}']$
p	$K_1 ([\text{A}_{\text{T}_1}'] / 2K_n)^{1/2} \text{PO}_2^{1/4}$	$[\text{A}_{\text{T}_1}']$

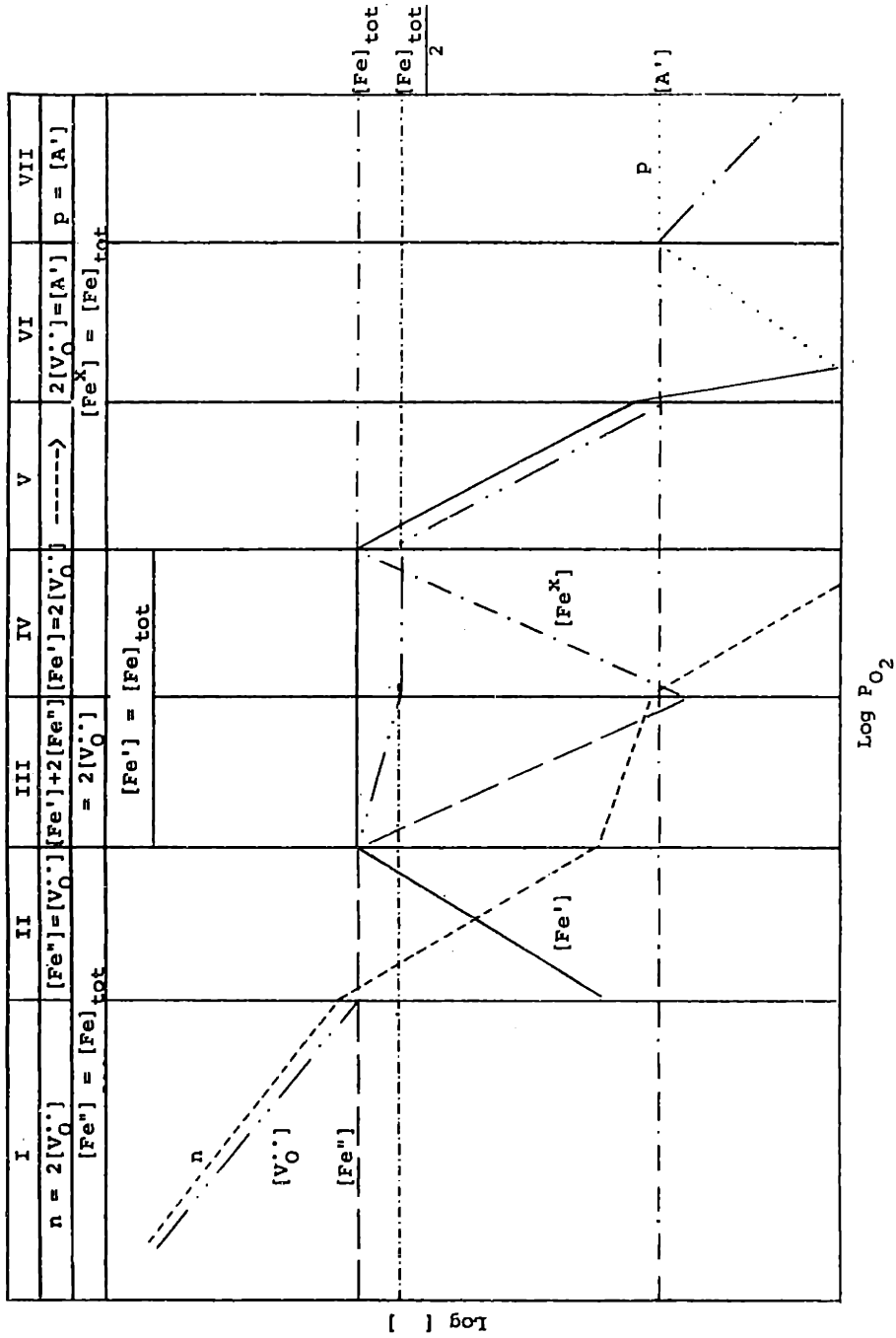


Figure 5. Idealized Kroger-Vink Diagram for BaTiO₃ doped with variable-valent Fe.

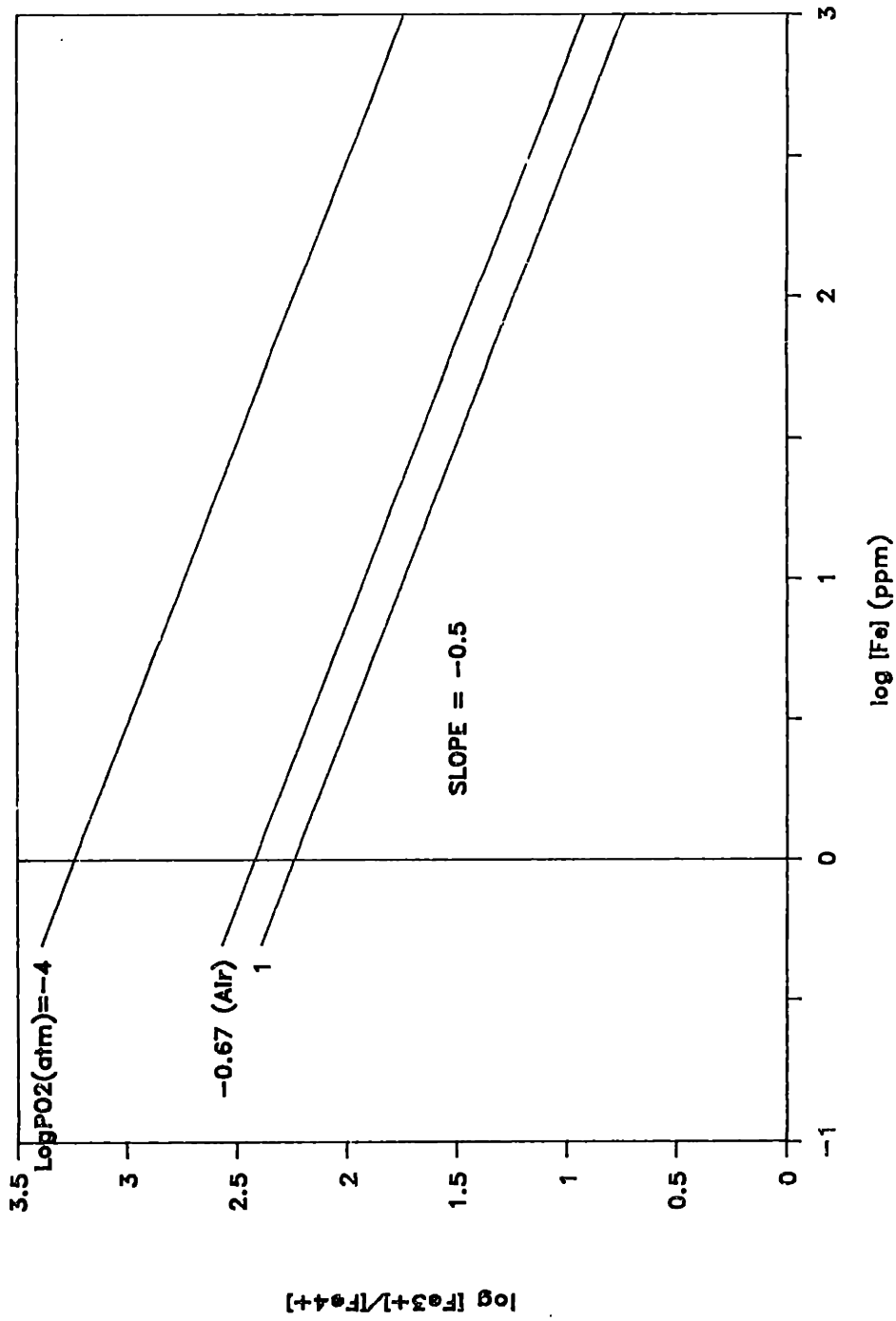


Figure 6. Variations in the Fe³⁺/Fe⁴⁺ valence ratio with increasing iron content.

P_{O2} Dependence of [Fe²⁺],[Fe³⁺],[Fe⁴⁺]

Temperature = 800°C

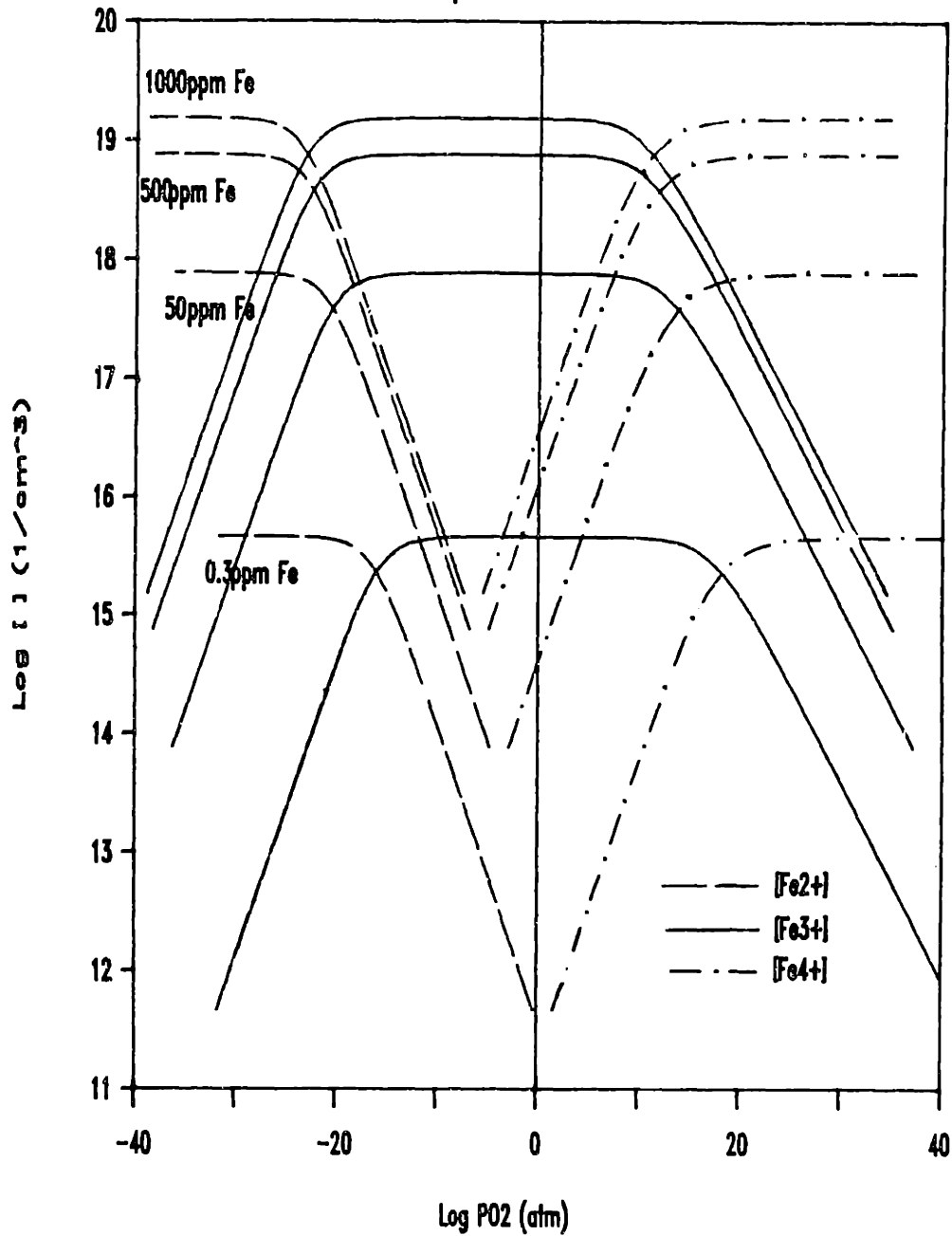


Figure 7. Variations in the $[\text{Fe}^{2+}]$, $[\text{Fe}^{3+}]$, and $[\text{Fe}^{4+}]$ as a function of P_{O_2} at various Fe concentrations.

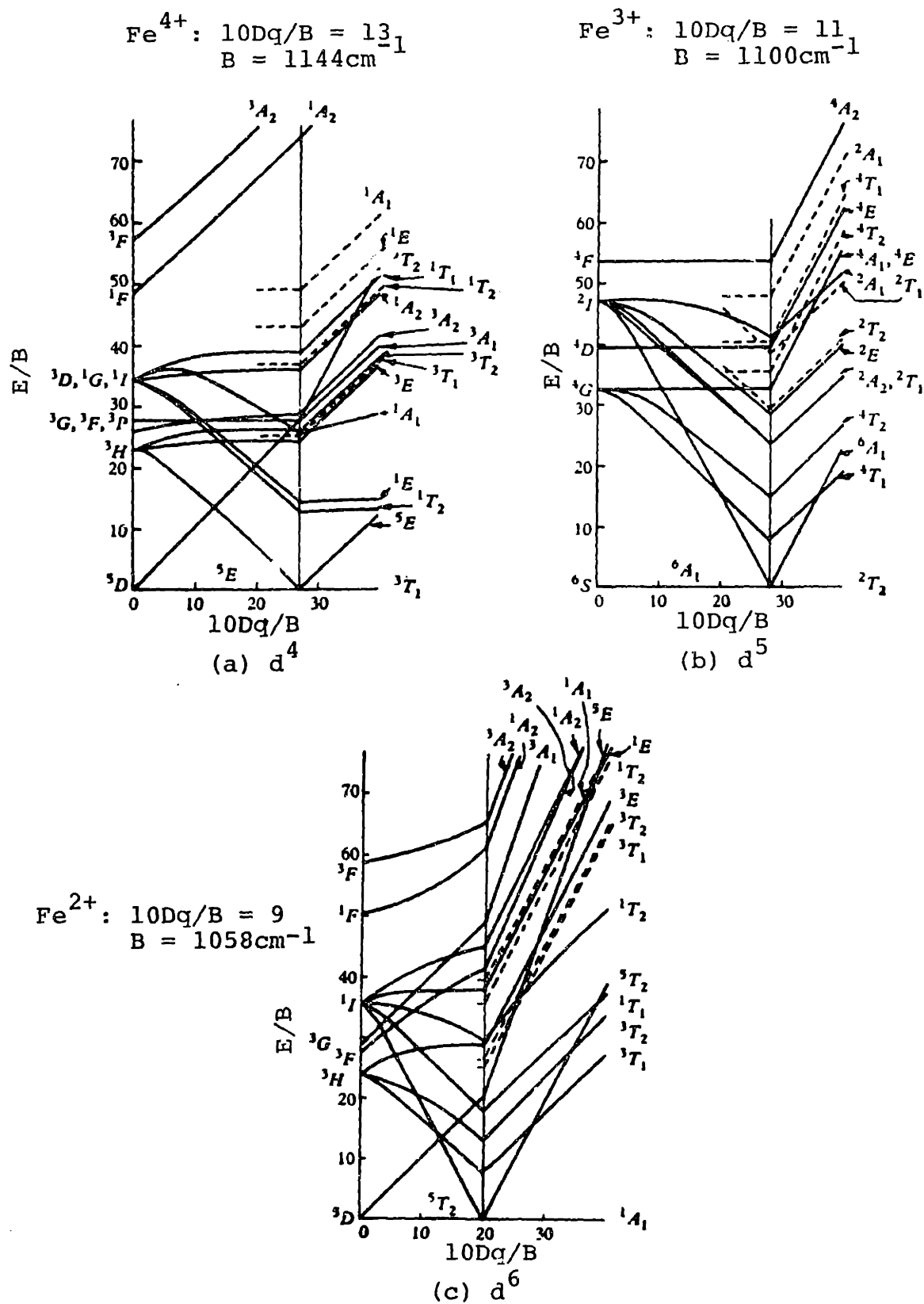


Figure 8. Tanabe-Sugano diagrams for (a) Fe^{4+} , d^4 ; (b) Fe^{3+} , d^5 ; and (c) Fe^{2+} , d^6 . (from reference 43)

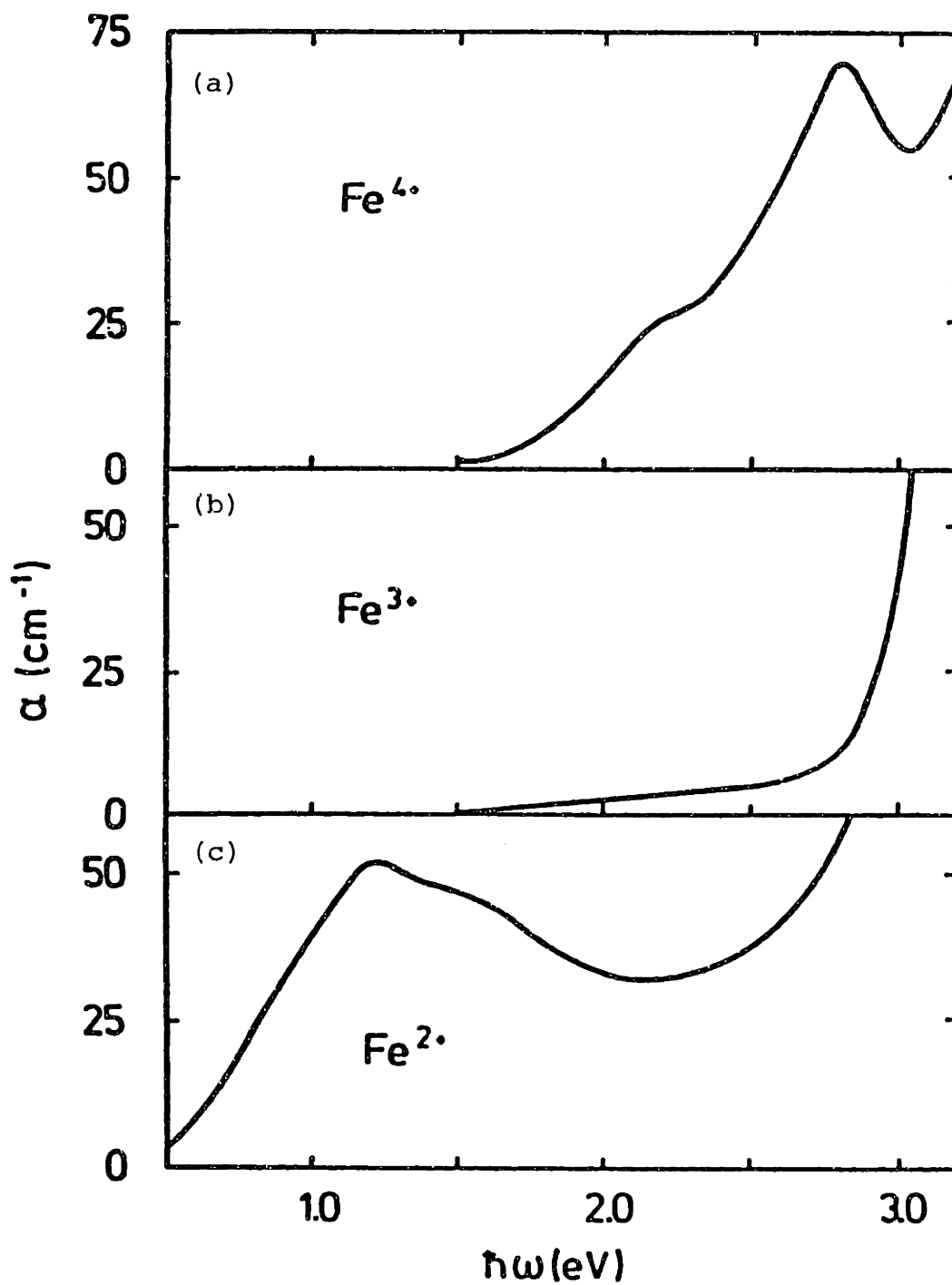


Figure 9. Optical absorption bands in Fe-doped SrTiO_3 (2300ppm). (a) oxidized, $P_{\text{O}_2} = 1\text{atm}$; (b) reduced, $P_{\text{O}_2} = 10^{-4}$ to 10^{-7}atm ; (c) heavily-reduced, $P_{\text{O}_2} = 10^{-26}\text{atm}$. (from reference 41)

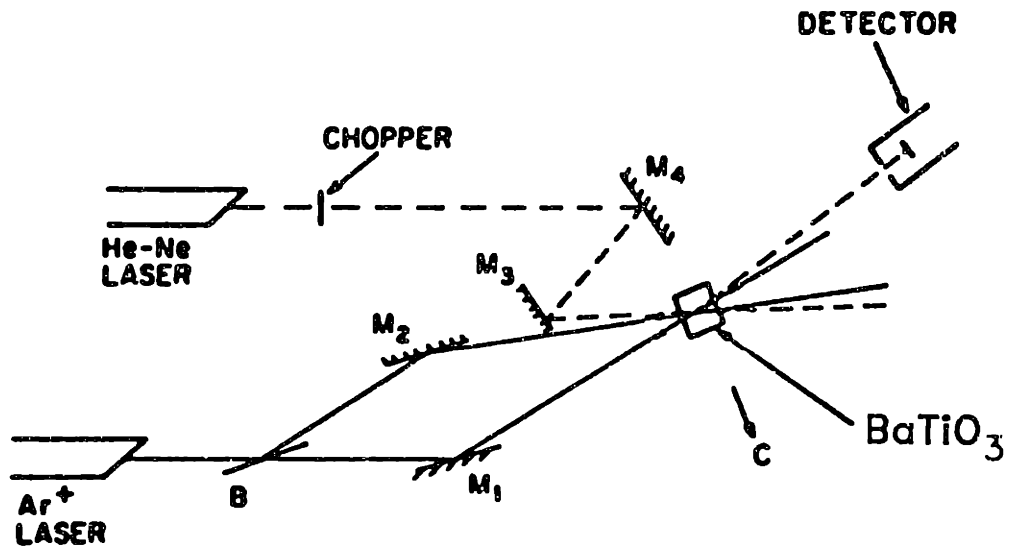


Figure 10. Typical experimental arrangement for holographic diffraction efficiency measurements. (from reference 9)

PURIFICATION of TITANIUM DIOXIDE

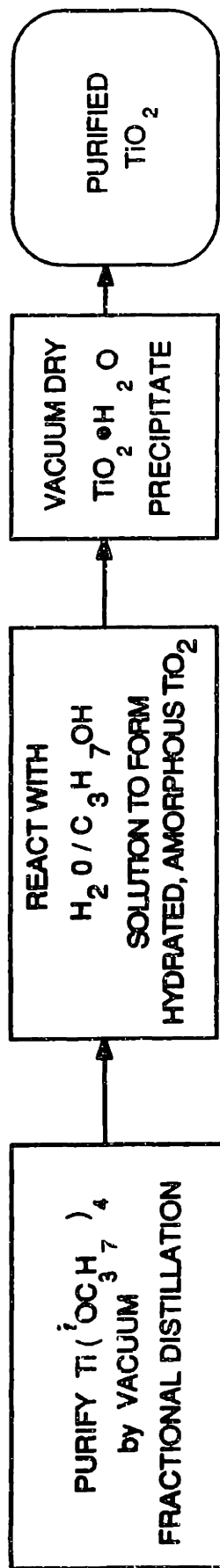


Figure 11. Flow-chart for preparation of high-purity TiO_2 .

Table 2. Boiling points of titanium isopropoxide and the isopropoxides of various possible impurities, $M(^iOC_3H_7)_n$, where n is the valence of the metal or rare earth impurity M.

Impurity	Boiling Point/Pressure
Titanium	49°C/0.1mm
Vanadium	70-80°C/0.1mm
Aluminum	106°C/1.5mm
Iron	149°C/0.1mm
Chromium	in soluble, non-volatile
Manganese	in soluble, non-volatile
Cobalt	in soluble, non-volatile
Nickel	in soluble, non-volatile
Copper	in soluble, non-volatile
Niobium	60-70°C/0.1mm
Tantalum	122°C/0.1mm
Zirconium	160°C/0.1mm
Halfnium	170°C/0.35mm
Cerium	160-170°/0.05mm
Thorium	200-210°C/0.1mm
Lanthanides	>200°C/0.1mm

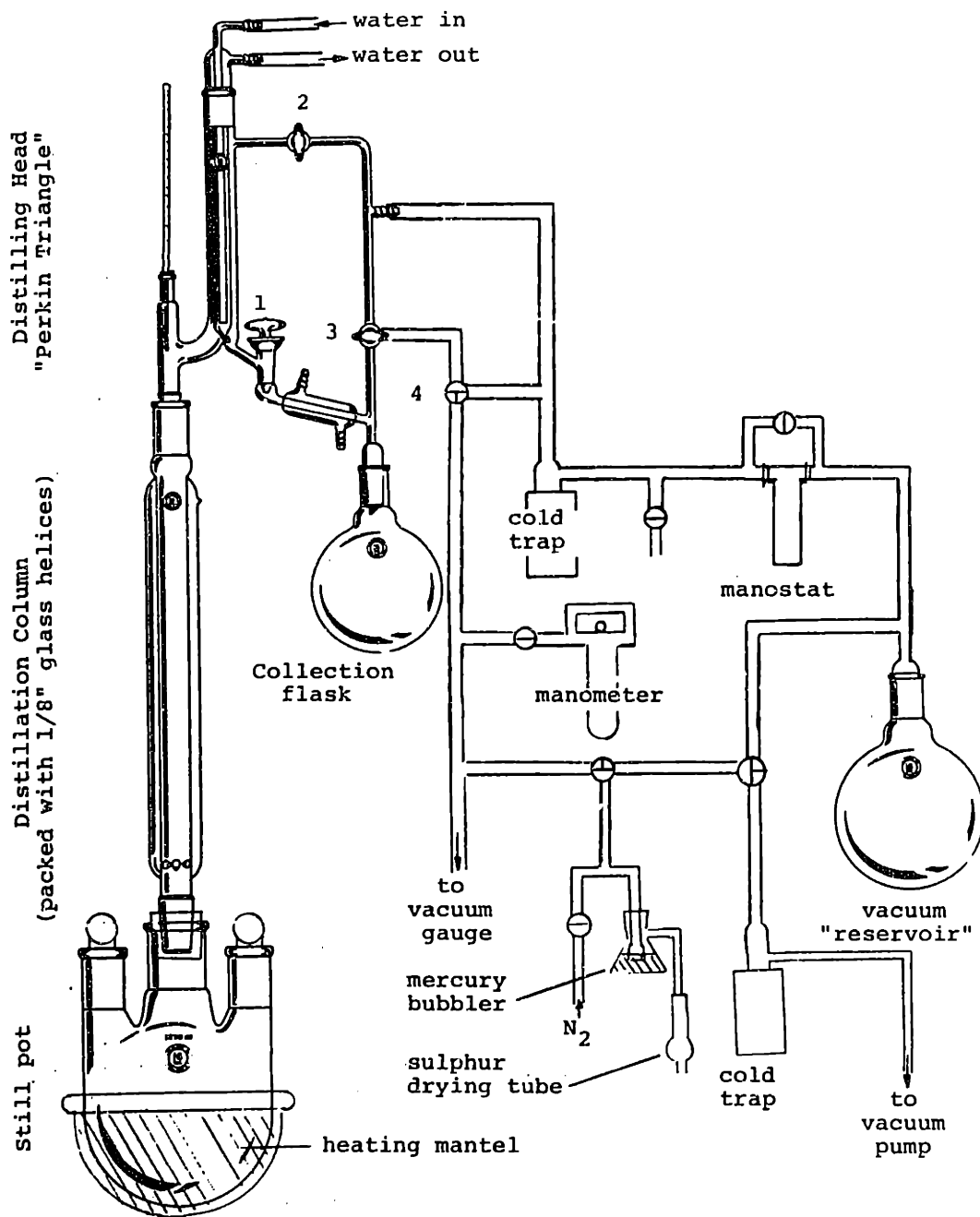


Figure 12. Fractional-distillation system used for the purification of titanium isopropoxide, $Ti(OC_3H_7)_4$.

PURIFICATION OF BARIUM CARBONATE

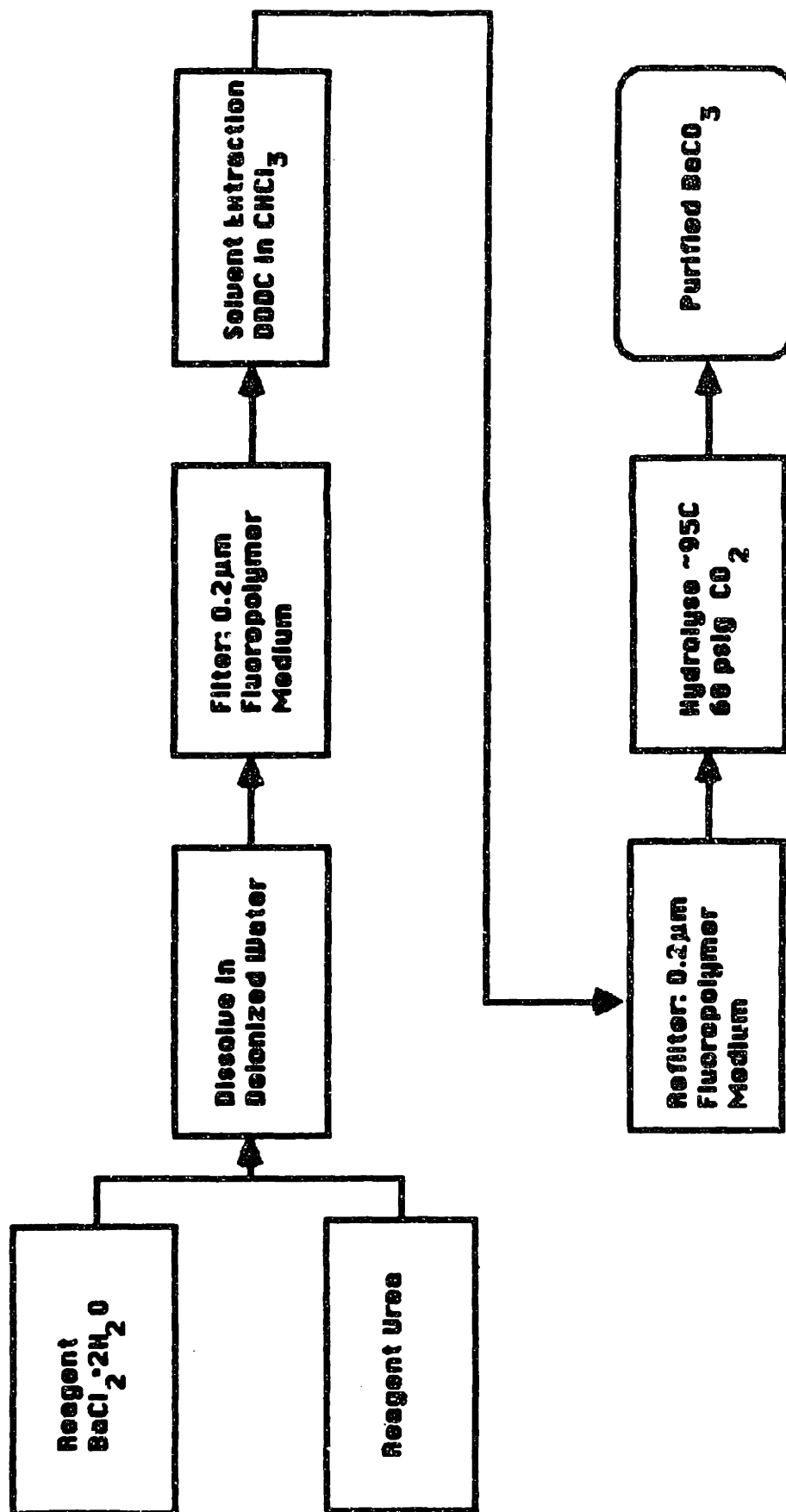


Figure 13. Flow chart for purification and synthesis of BaCO₃. (D.R. Gabbe)

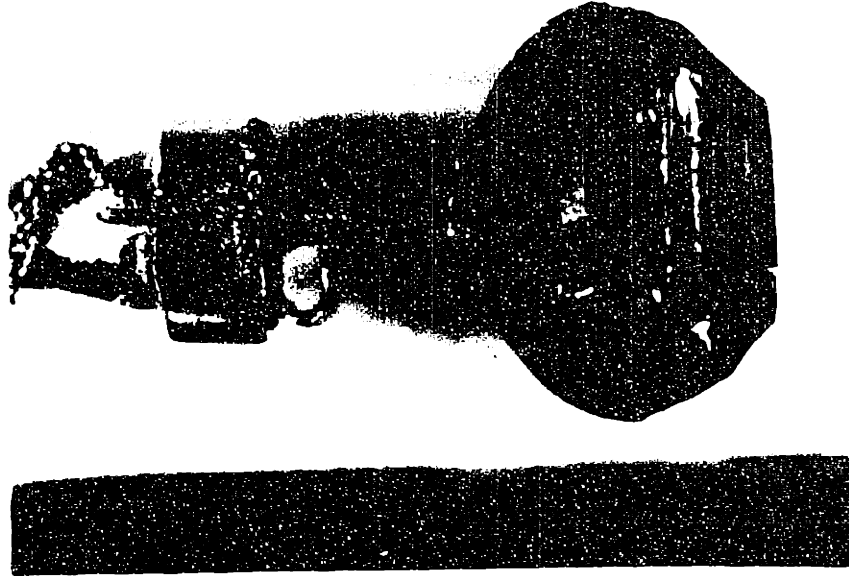


Figure 14. Typical single crystal boule grown by TSSG.

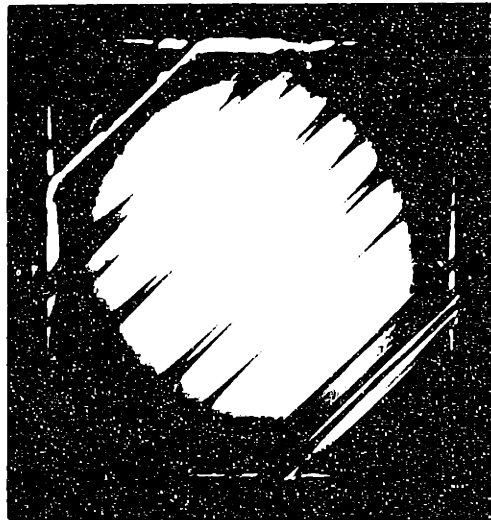


Figure 15. 90 degree domain walls (diagonal lines) in unpoled BaTiO₃ single crystal.

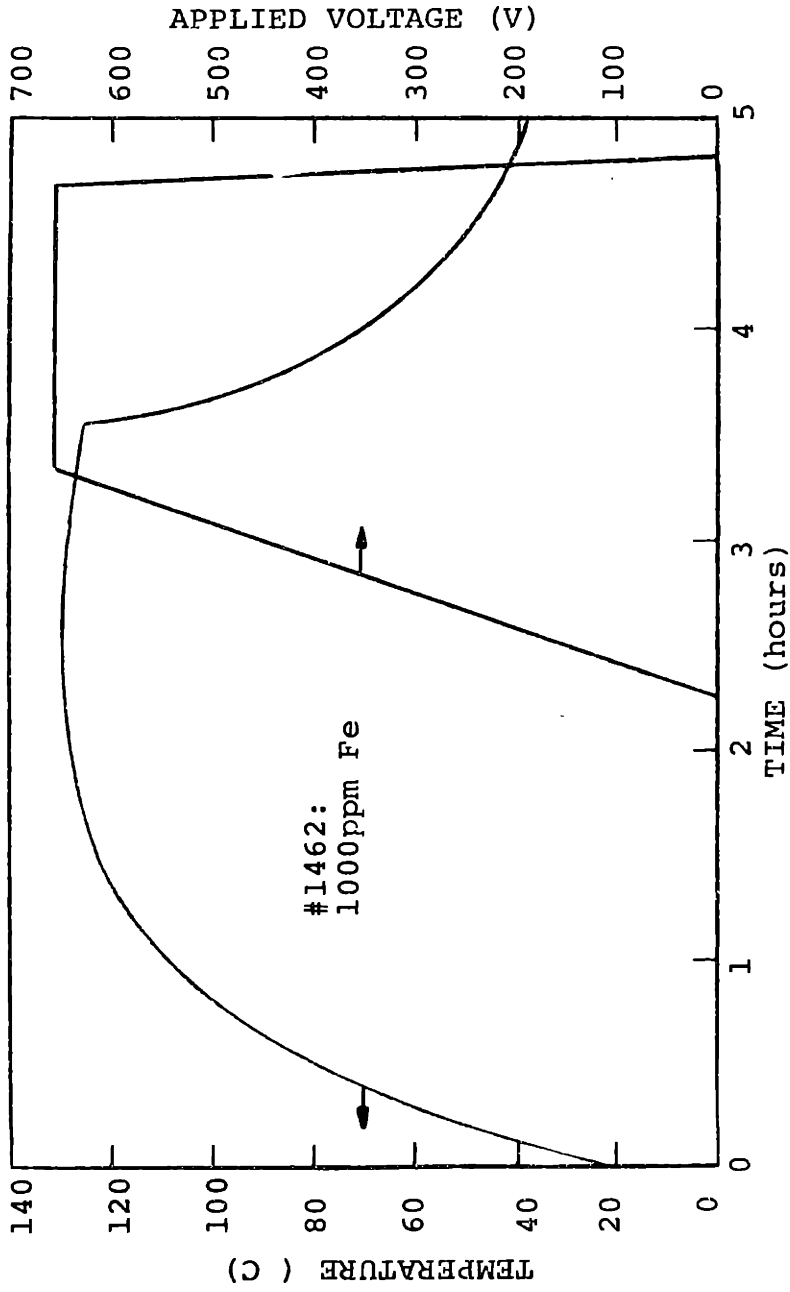
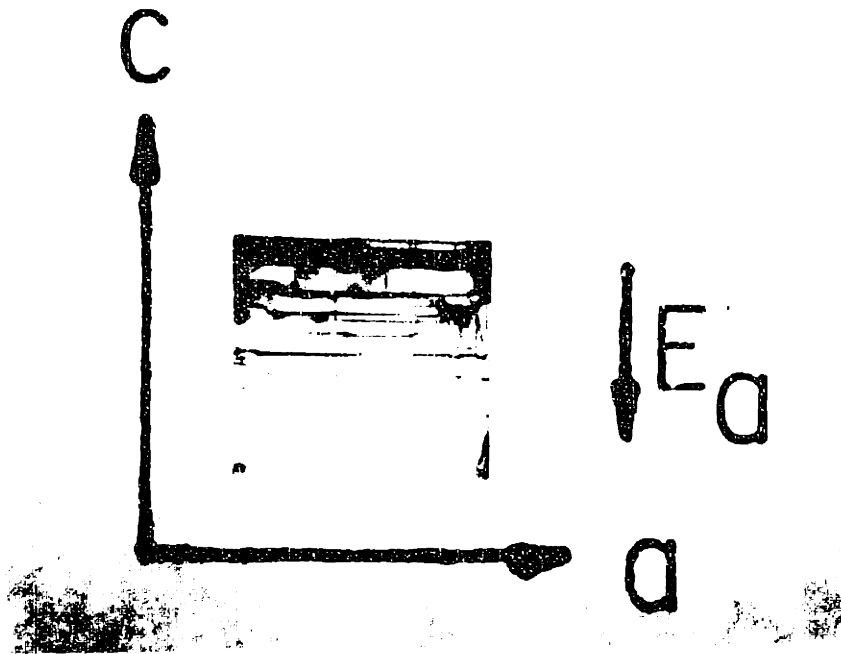


Figure 16. Typical voltage-temperature-time profile used for electrical poling.



Top View

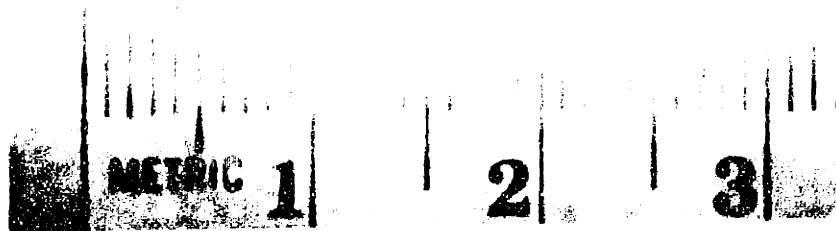


Figure 17. Extreme example of cracking near the positive electrode which can occur during electrical poling of a sample with residual internal stresses.

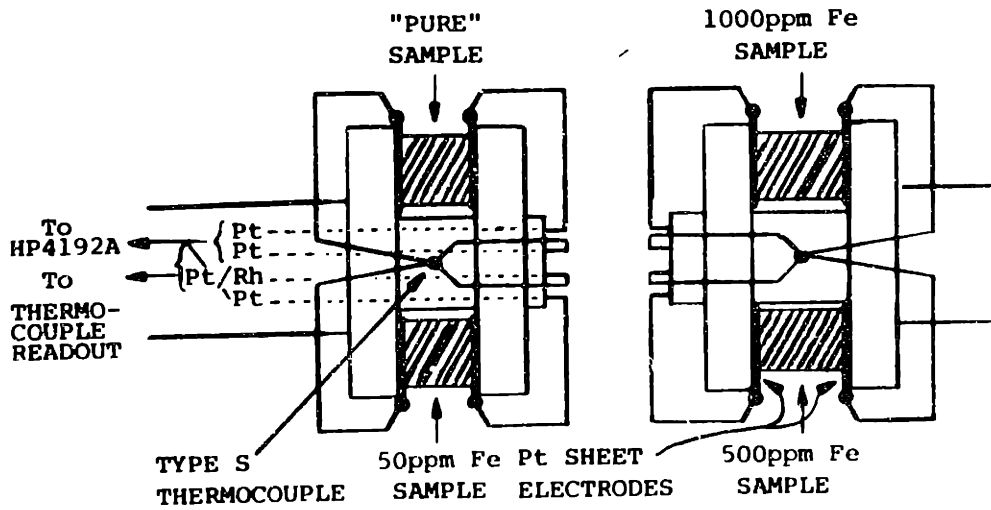
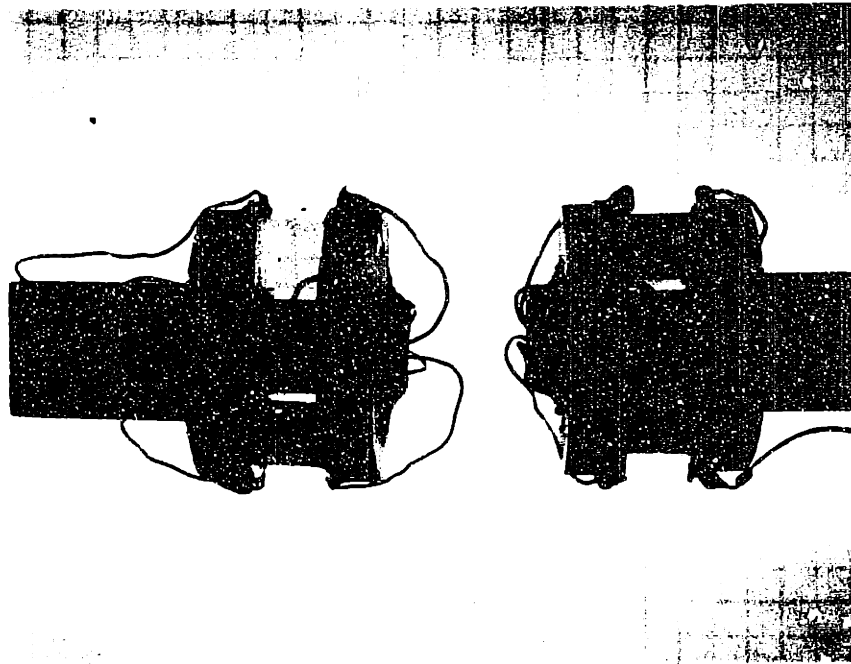


Figure 18. Sample holder used for high-temperature electrical conductivity measurements, shown here with optical samples mounted for annealing.

Table 3. Spark-source mass spectrographic analysis of reagent precursors, purified feed materials, and resulting BaTiO₃ single crystal (Quantities given in ppm atomic).

Element	TiO ₂ (unpurified)	TiO ₂ (purified)	BaCl ₂ (unpurified)	Urea (unpurified)	BaCO ₃ (purified)	BaTiO ₃
Li ⁺	0.5		2		1	
B ³⁺	2	3	2	0.2	1	5
Na ⁺	≤2	≤2	2	0.5	2	≤2
Mg ²⁺	2	2	1	≤1	5	2
Al ³⁺	1	2	2	2	3	0.5
*Si ⁴⁺	5	5	4	10	4	4
P ⁵⁺	0.1	0.03	0.2	0.1	0.1	0.05
S ²⁻	<2	<2	<2	<0.5	<2	<2
Cl ⁻	10	3	Major	2	150	10
K ⁺	2	2	≤0.2	0.1	2	≤0.1
*Ca ²⁺	3	5	200	3	250	2
Cr ^{3+,2+}	0.06		≤0.02	≤0.02	0.05	≤0.02
Mn ^{2,3,4+}					≤0.02	≤0.02
Fe ^{2,3,4+}	2	0.5	0.3	0.2	1	0.3
Ni ^{2,3+}	0.3		0.1	≤0.04	≤0.04	0.04
Cu ^{1,2+}	0.1		≤0.02	≤0.02	0.06	
Zn ²⁺			≤0.1		0.1	
As ⁵⁺			0.5		0.05	0.1
*Sr ²⁺			30		20	50
*Zr ⁴⁺	0.1		<0.04		0.1	
Nb ⁵⁺	0.03					
La ³⁺			0.06		0.06	
Ce ^{3,4+}			≤0.02		≤0.02	
Pr ^{3,4+}					≤0.02	
Nd ³⁺					≤0.08	
*Pb ²⁺			≤0.04		≤0.04	

*Isovalent impurities

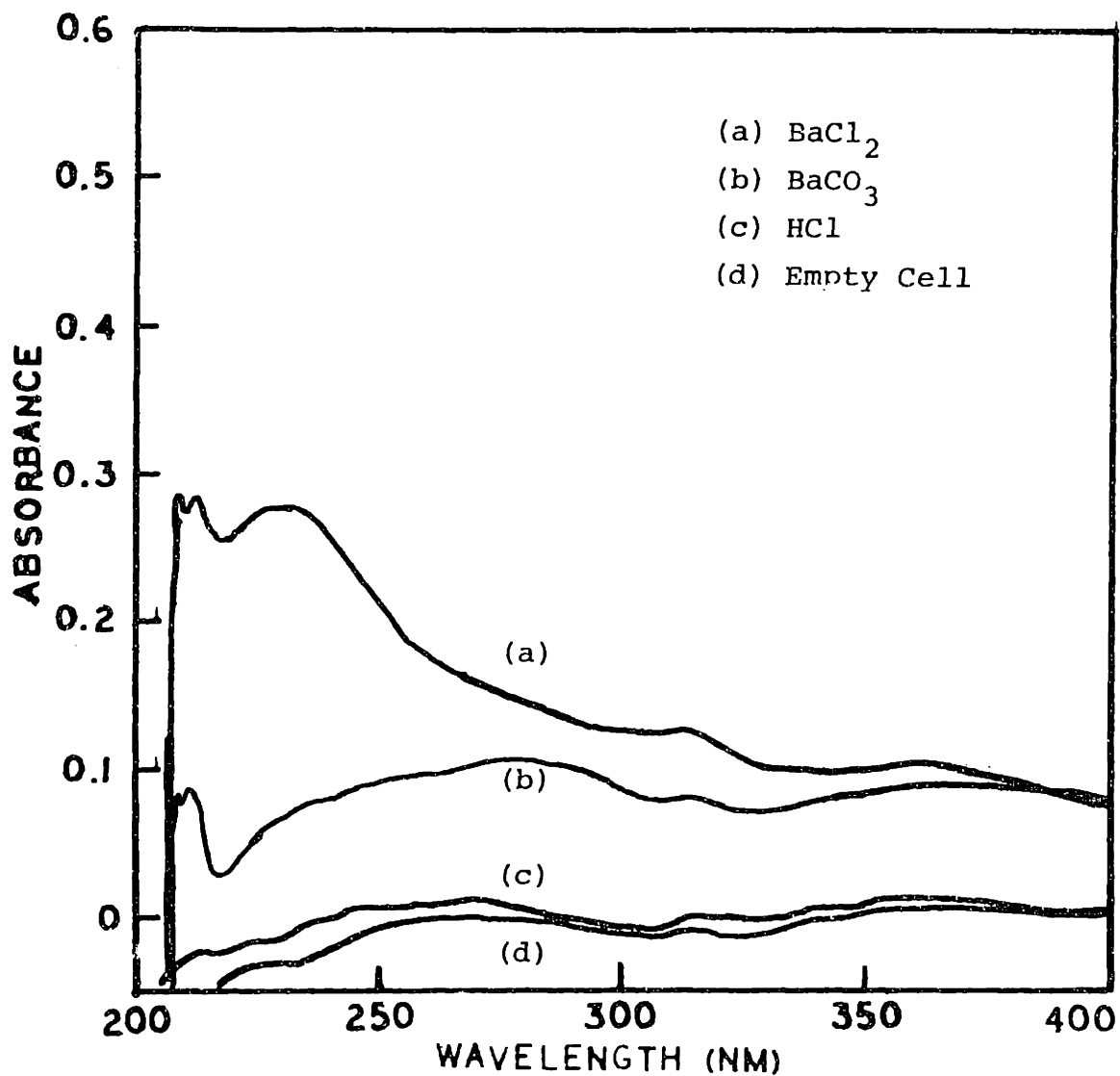


Figure 19. Ultraviolet spectra of reagent BaCl₂ and purified BaCO₃ dissolved in HCl. Peak at 230nm corresponds to iron impurities removed by purification.

Undoped Barium Titanate

From Purified & Reagent Feed Material

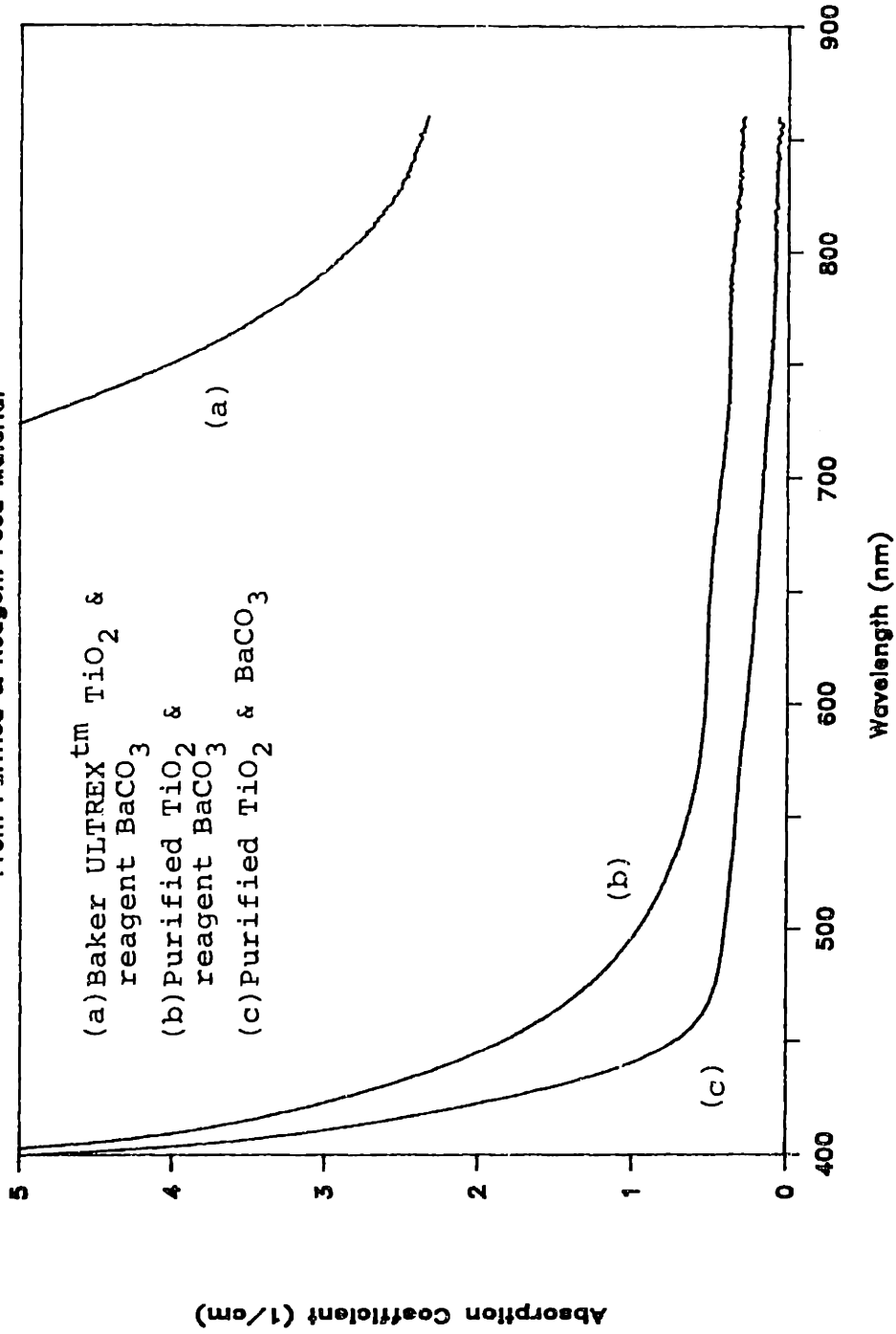


Figure 20. Optical absorption spectra comparing relative purity of BaTiO₃ single crystals grown from different feed materials.

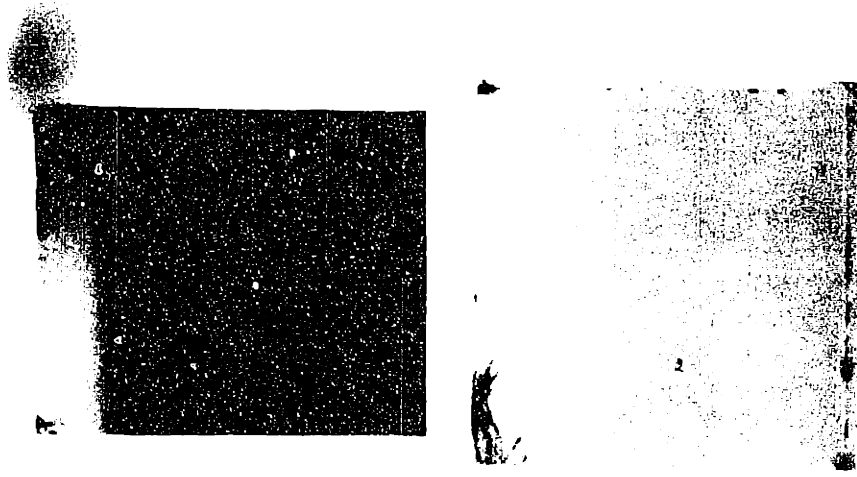


Figure 22. Color bands formed in 500ppm (bottom) and 1000ppm (top) Fe-doped BaTiO₃ during electrical poling in an oil bath.

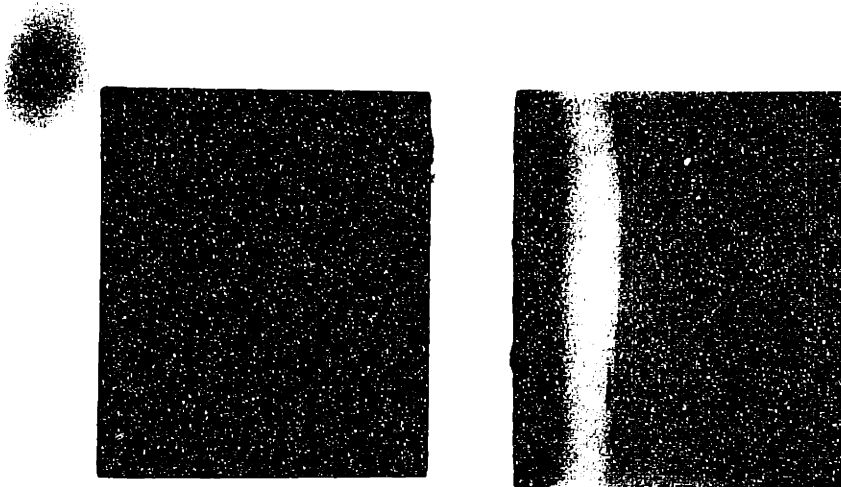


Figure 21. Coloration bands observed after prolonged oxygen annealing and subsequent electrical poling of 500ppm (bottom) and 1000ppm (top) Fe-doped BaTiO₃.

High Purity Barium Titanate

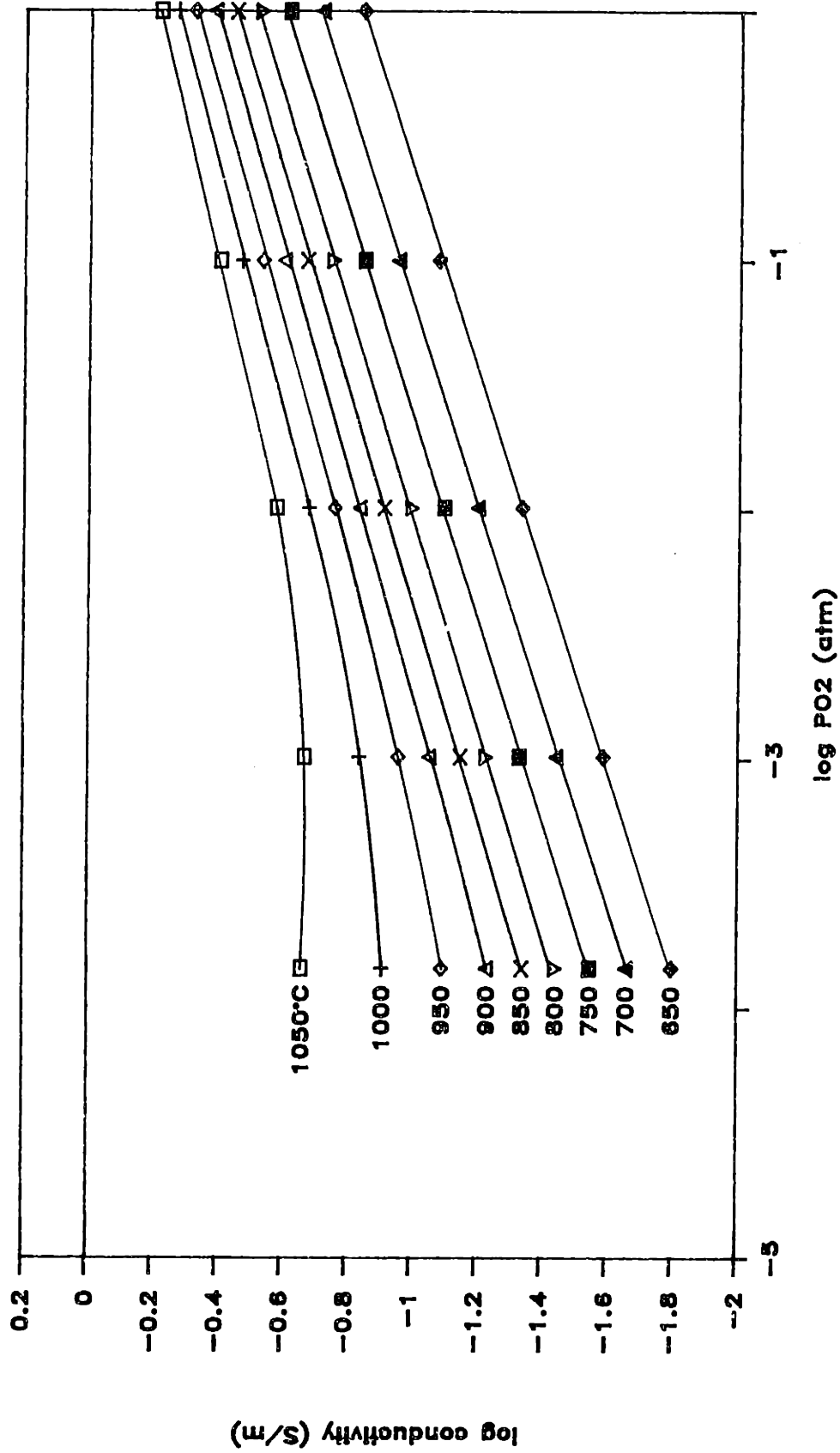


Figure 23. Equilibrium electrical conductivity data for high purity BaTiO₃ single crystal.

Barium Titanate: 50ppm Fe

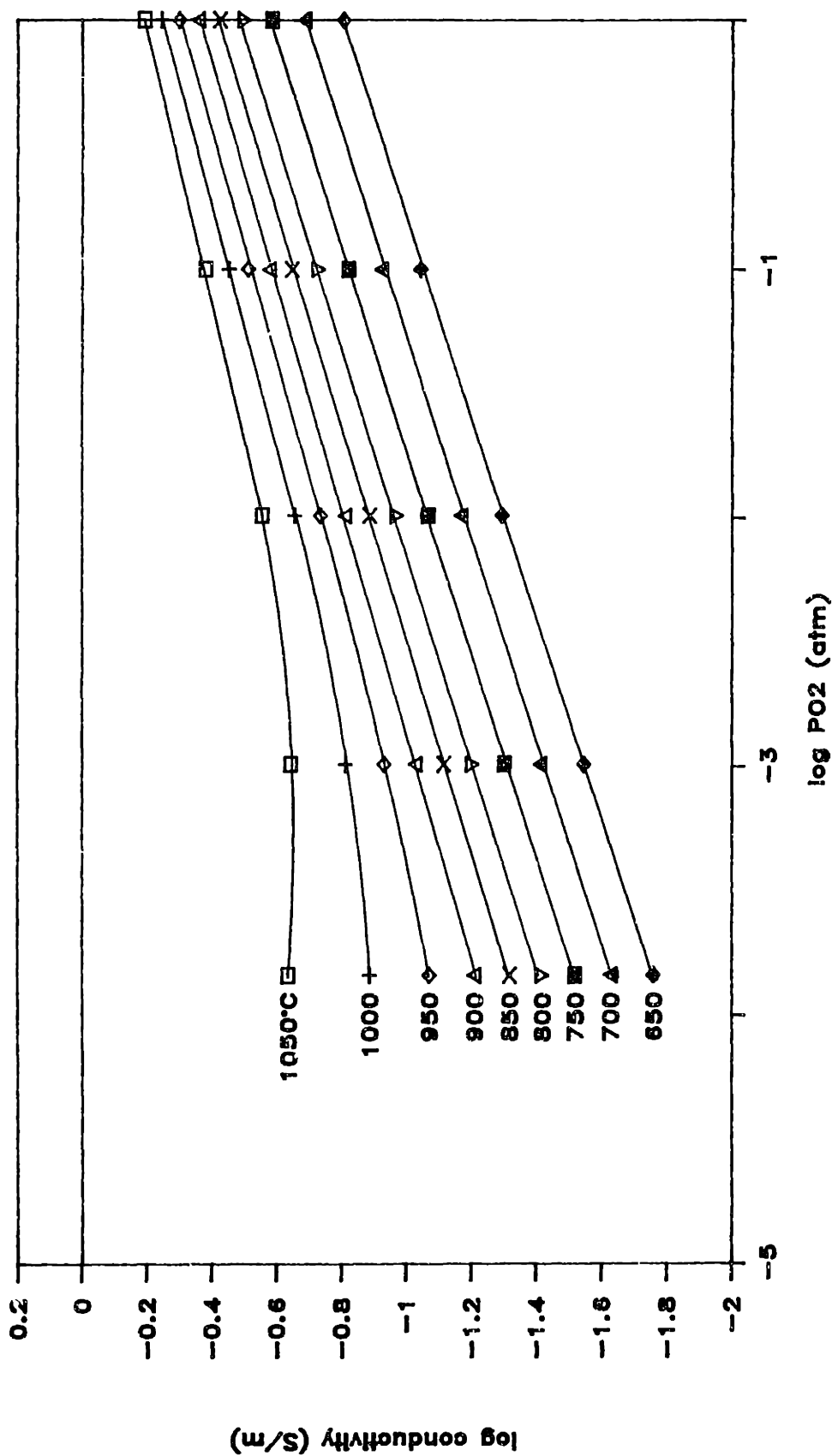


Figure 24. Equilibrium electrical conductivity data for BaTiO₃ single crystal doped with 50ppm Fe.

Barium Titanate: 500ppm Fe

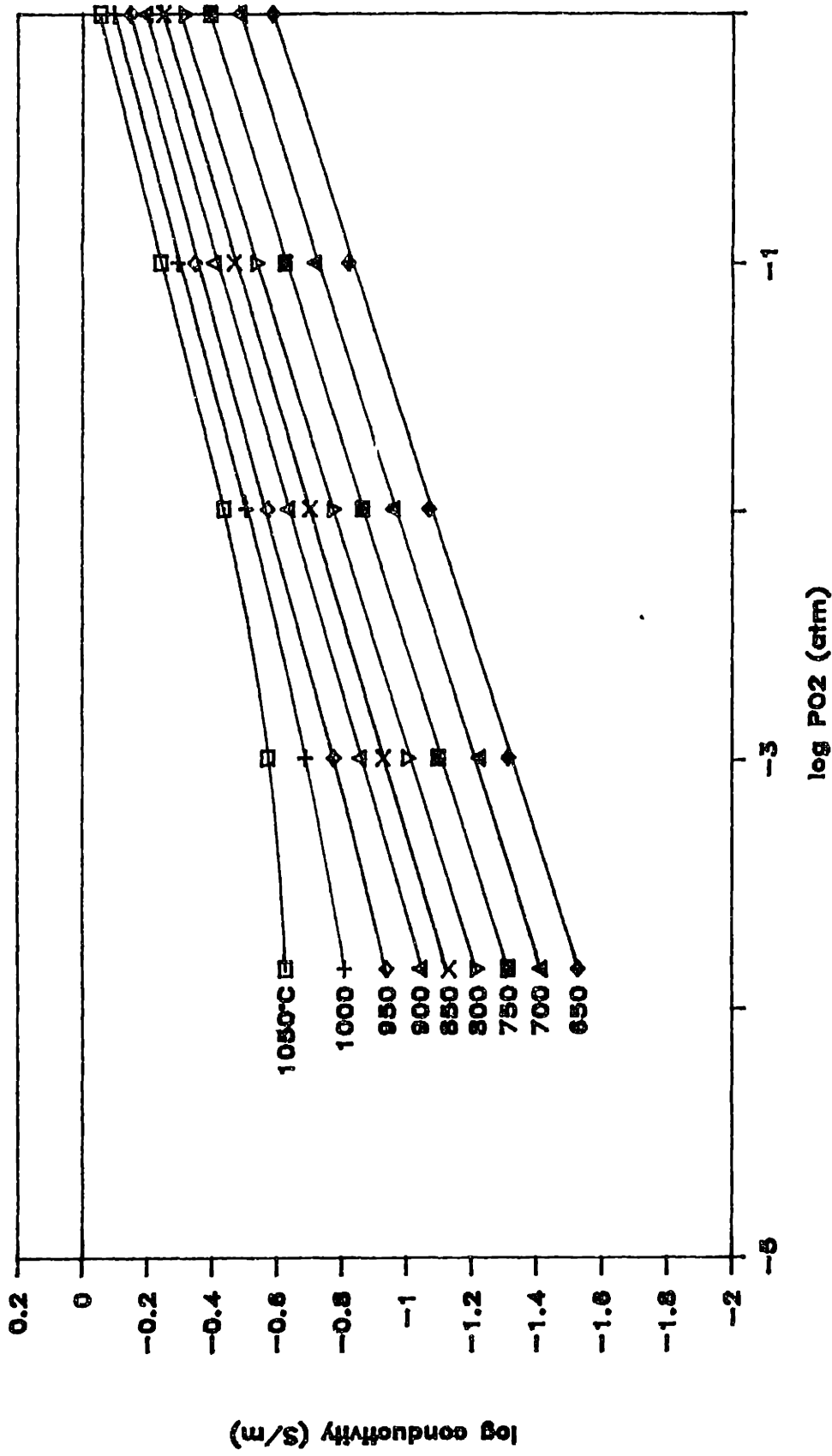


Figure 25. Equilibrium electrical conductivity data for BaTiO₃ single crystal doped with 500ppm Fe.

Barium Titanate: 1000ppm Fe

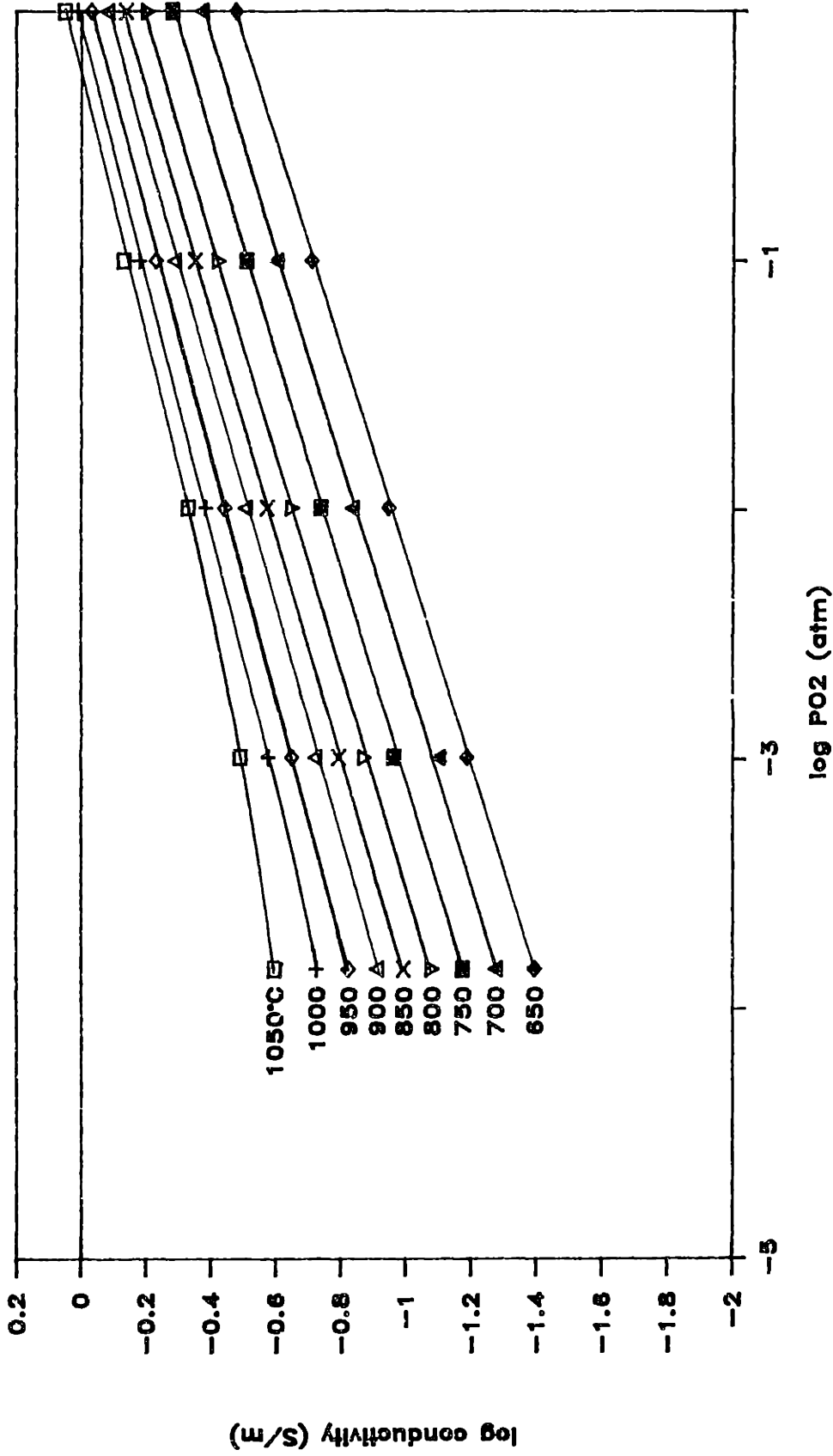


Figure 26. Equilibrium electrical conductivity data for BaTiO₃ single crystal doped with 1000ppm Fe.

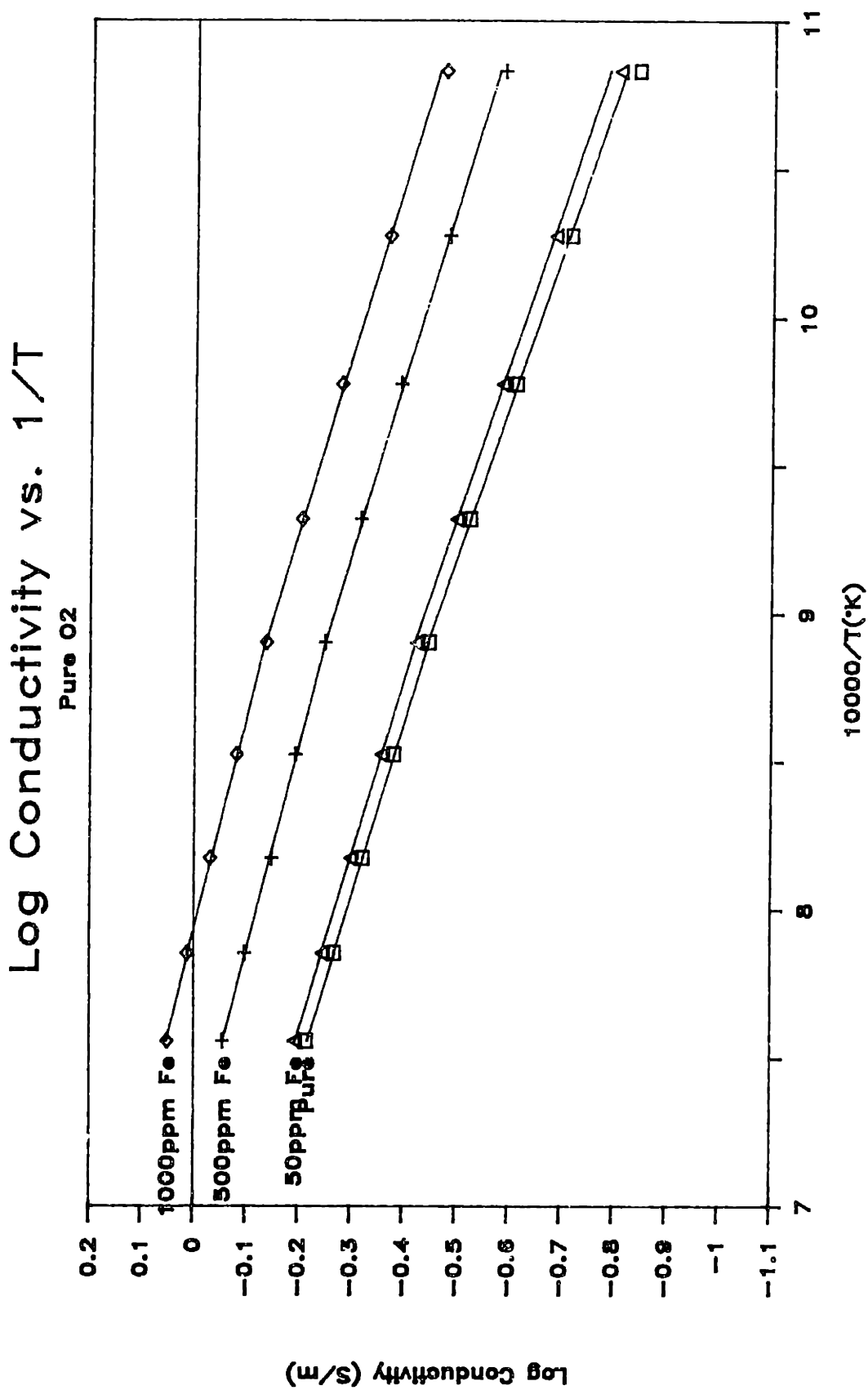


Figure 27. Arrhenius plots comparing electrical conductivity of high purity, 50, 500, and 1000ppm Fe-doped BaTiO₃; PO₂ = 1atm.

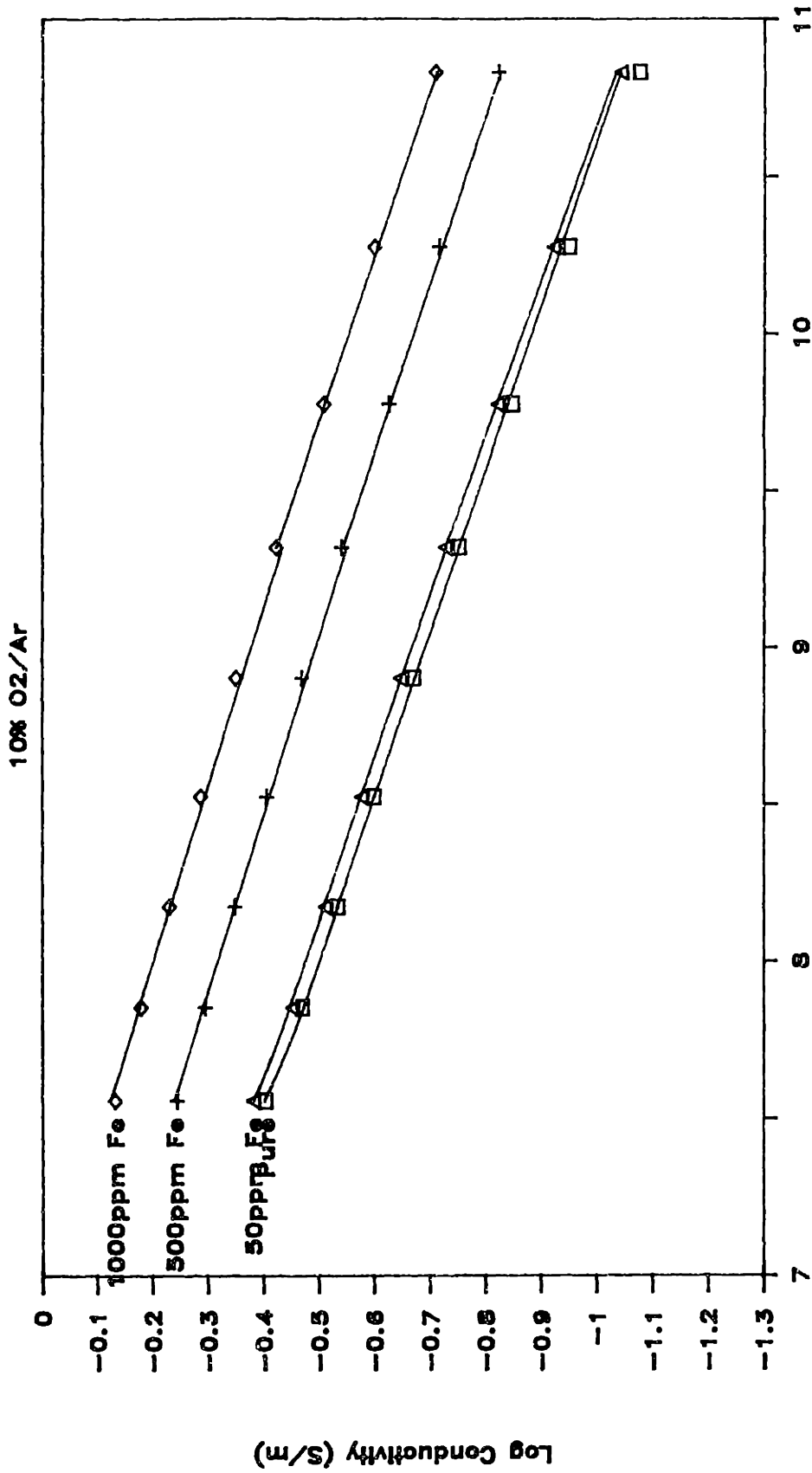
Log Conductivity vs. $1/T$ 

Figure 28. Arrhenius plots comparing electrical conductivity of high purity, 50, 500, and 1000ppm Fe-doped BaTiO₃: PO₂ = 10⁻¹atm.

Log Conductivity vs. $1/T$

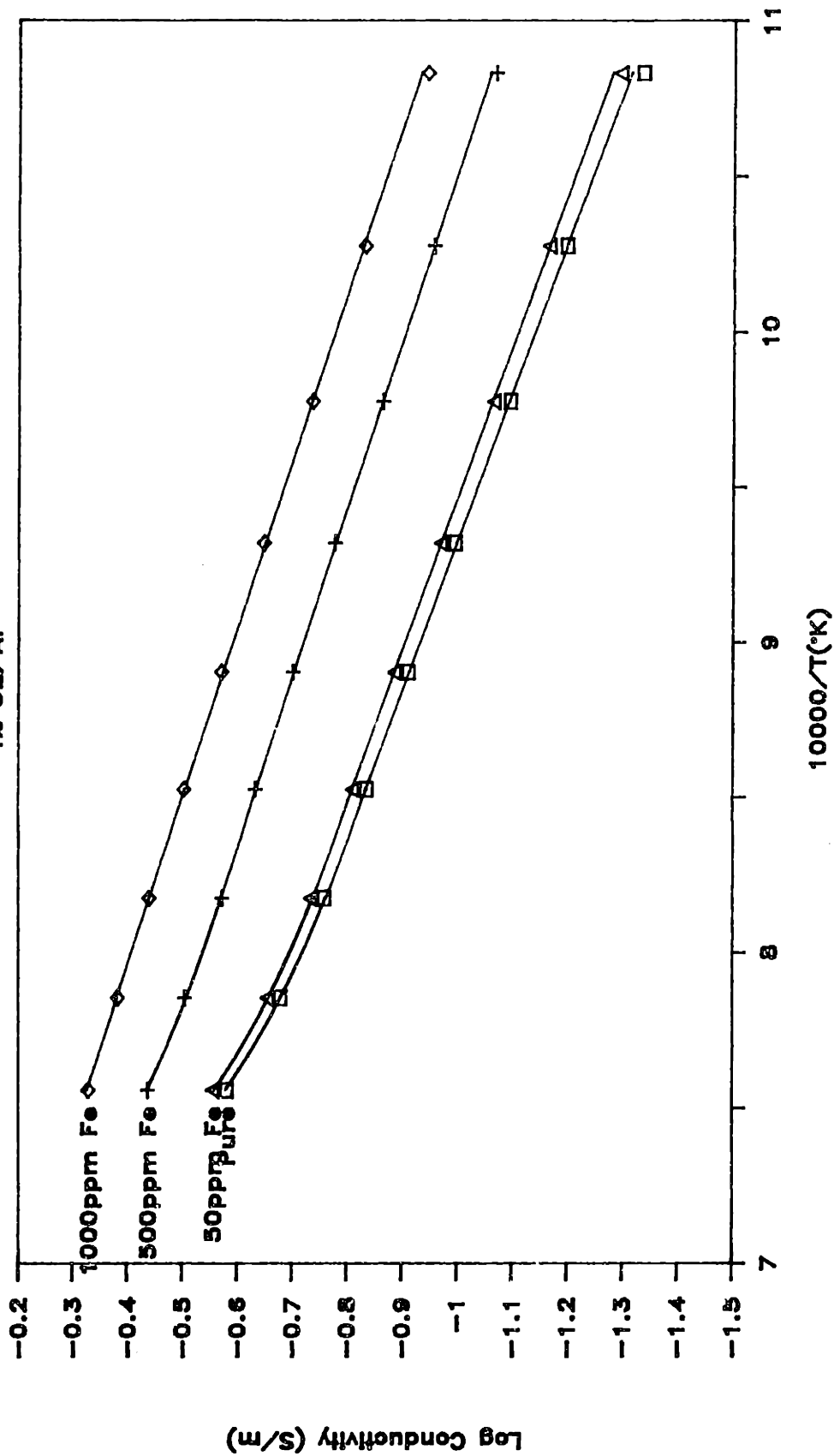


Figure 29. Arrhenius plots comparing electrical conductivity of high purity, 50, 500, and 1000ppm Fe-doped BaTiO₃: PO₂ = 10⁻²atm.

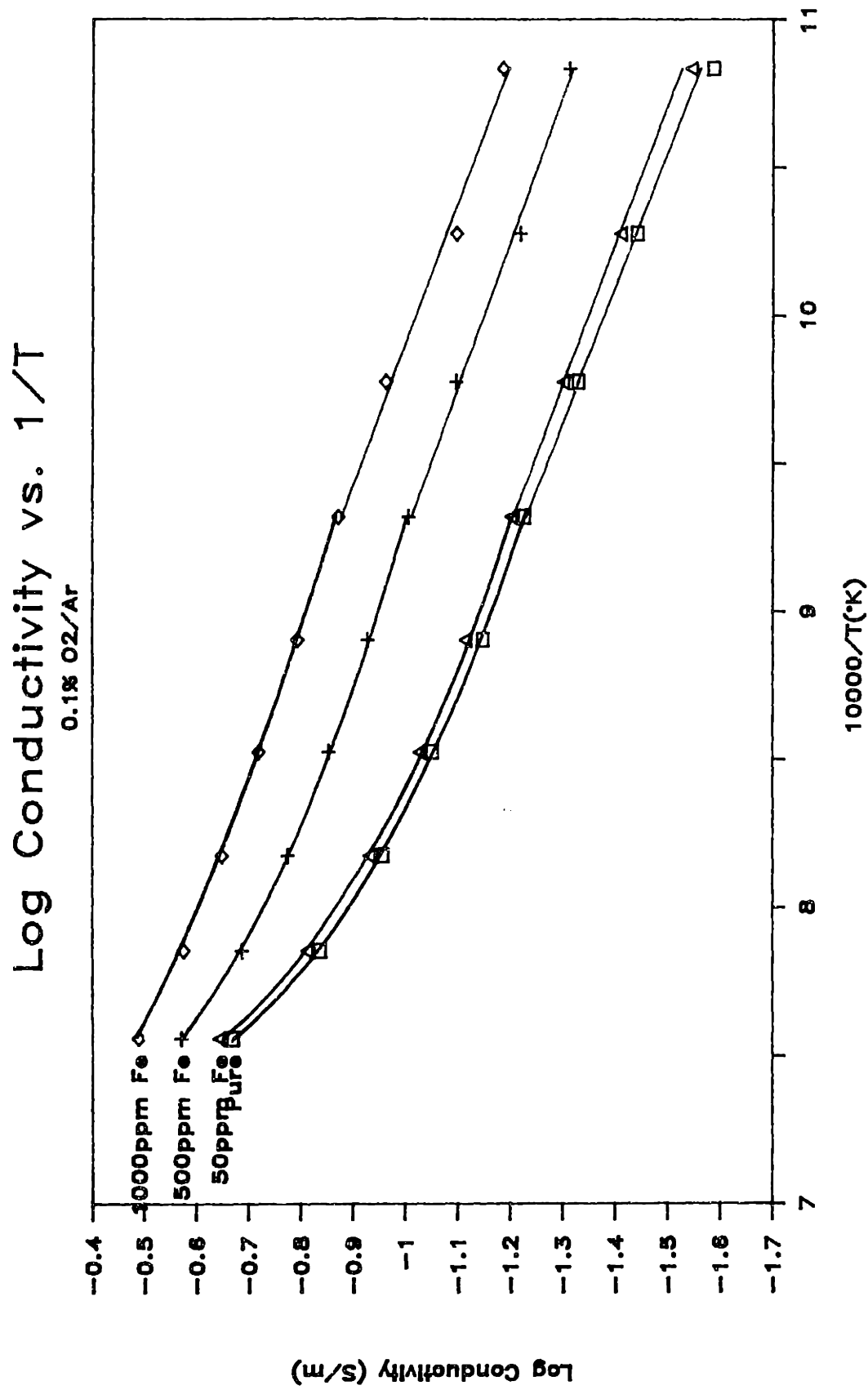


Figure 30. Arrhenius plots comparing electrical conductivity of high purity, 50, 500, and 1000ppm Fe-doped BaTiO₃: PO₂ = 10⁻³atm.

Log Conductivity vs. $1/T$

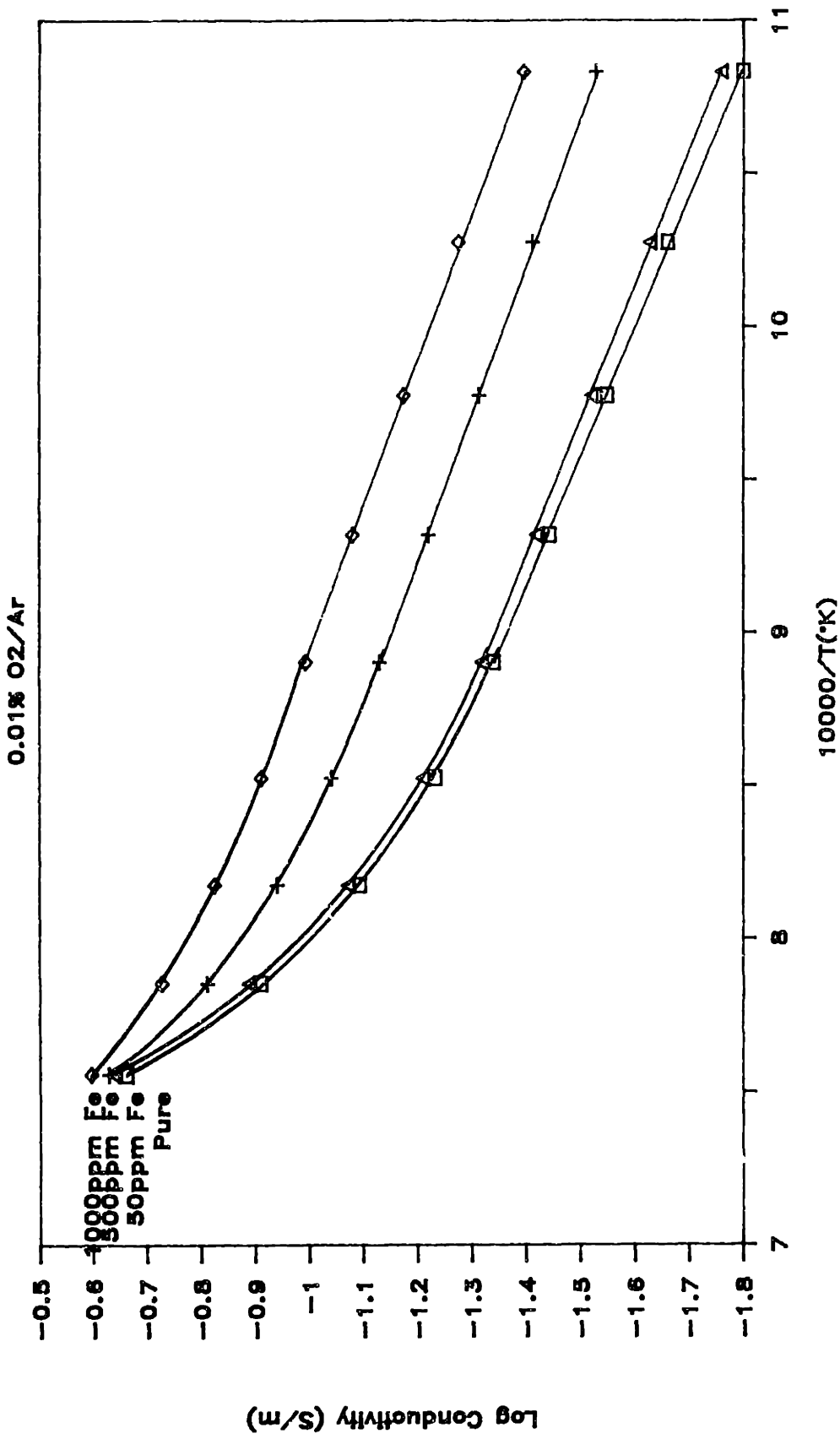


Figure 31. Arrhenius plots comparing electrical conductivity of high purity, 50, 500, and 1000ppm Fe-doped BaTiO₃: PO₂ = 10⁻⁴atm (logPO₂ = -3.84 measured).

Table 4. P_{O_2} dependence m of p-type electrical conductivity, where $\sigma \propto P_{O_2}^{1/m}$.

Temp. (\pm C)	Pure	50ppm	500ppm	1000ppm
1050	5.47	5.49	5.22	5.24
1000	4.85	4.86	4.89	5.07
950	4.57	4.58	4.73	4.83
900	4.45	4.44	4.51	4.62
850	4.28	4.29	4.36	4.49
800	4.19	4.19	4.26	4.40
750	4.11	4.12	4.19	4.32
700	4.06	4.08	4.10	4.19
650	3.99	4.02	4.08	4.18

Table 5. Enthalpies of oxygen vacancy formation, ΔH_p , calculated from Arrhenius slopes in Figures 27-31. (Values from high-temperature fit in parentheses.)

log P_{O_2}	Fe Concentration (ppm)			
	0	50	500	1000
0	130.4	130.4	130.3	128.2
-1.99	130.4	130.4	130.2	128.1
-3.84	130.6	130.6	131.0	129.0

Table 6. Curie temperature ($^{\circ}$ C) dependence on Fe concentration and annealing atmosphere.

Sample	Log Oxygen Partial Pressure (atm)				
	0	-1.00	-1.99	-2.99	-3.84
Pure	0.7666 (0.6804)	0.8197 (0.7589)	0.8246	0.8712	0.9385
50ppm Fe	0.7531 (0.6741)	0.8024 (0.8024)	0.8096	0.8422	0.9032
500ppm Fe	0.6733 (0.5728)	0.7424 (0.7424)	0.7308	0.8106	0.8261
1000ppm Fe	0.6721 (0.5559)	0.7538 (0.7007)	0.7359	0.8370	0.8353

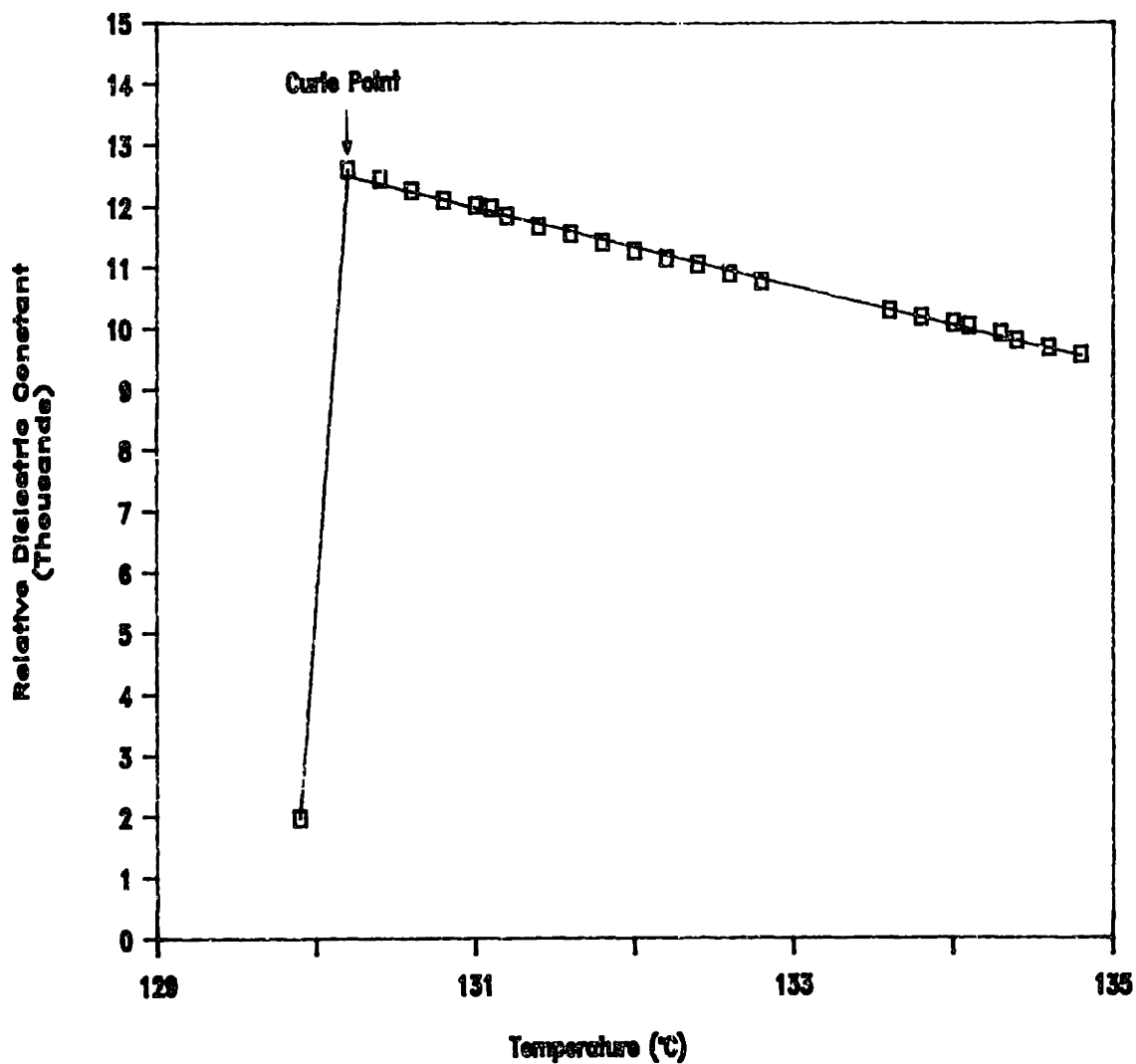


Figure 32. Typical plot of dielectric constant vs. temperature indicating cubic-to-tetragonal phase transition.

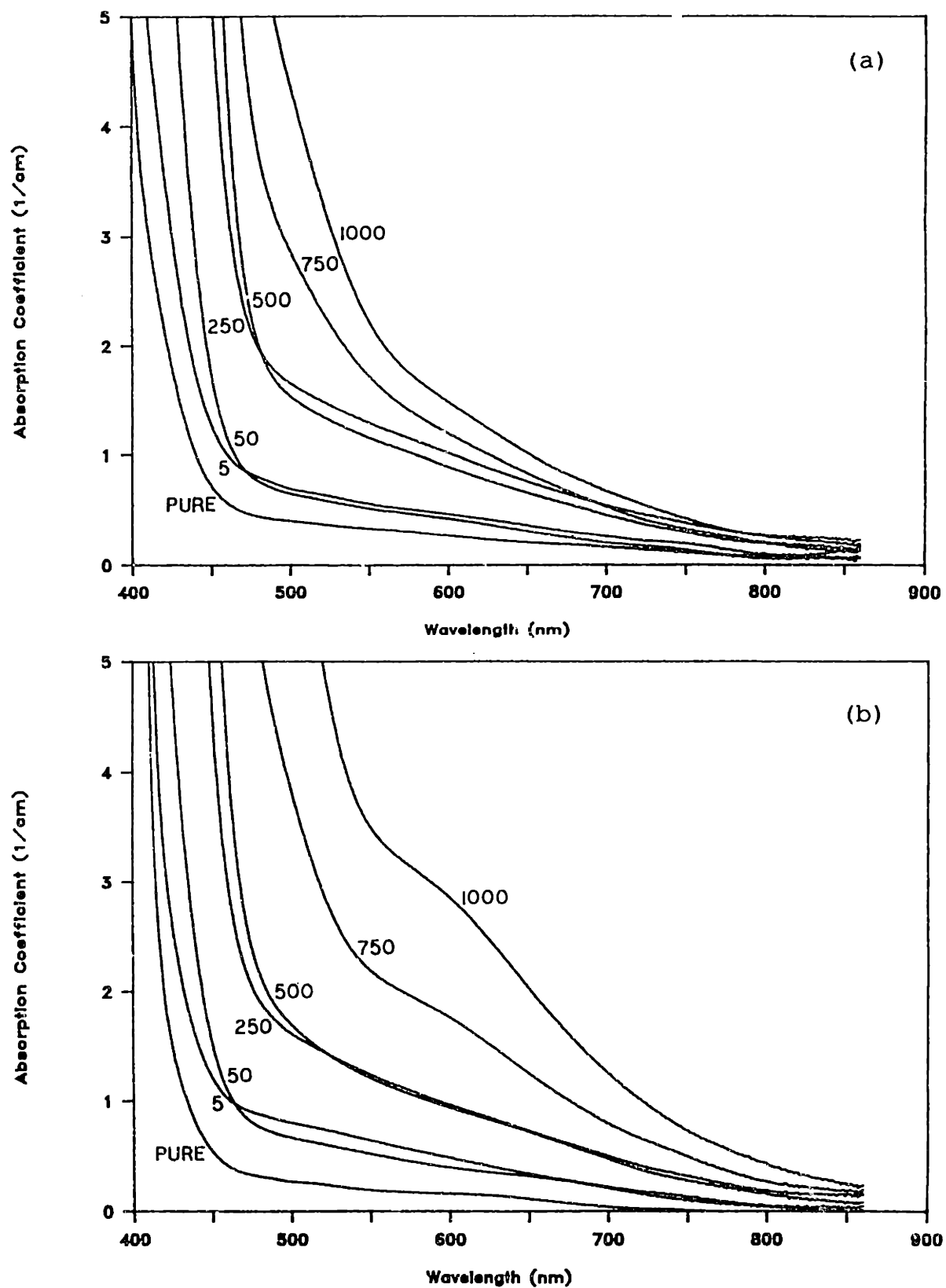


Figure 33. Optical absorption spectra for as-grown crystals after mechanical poling: (a) E parallel to c; (b) E perpendicular to c.

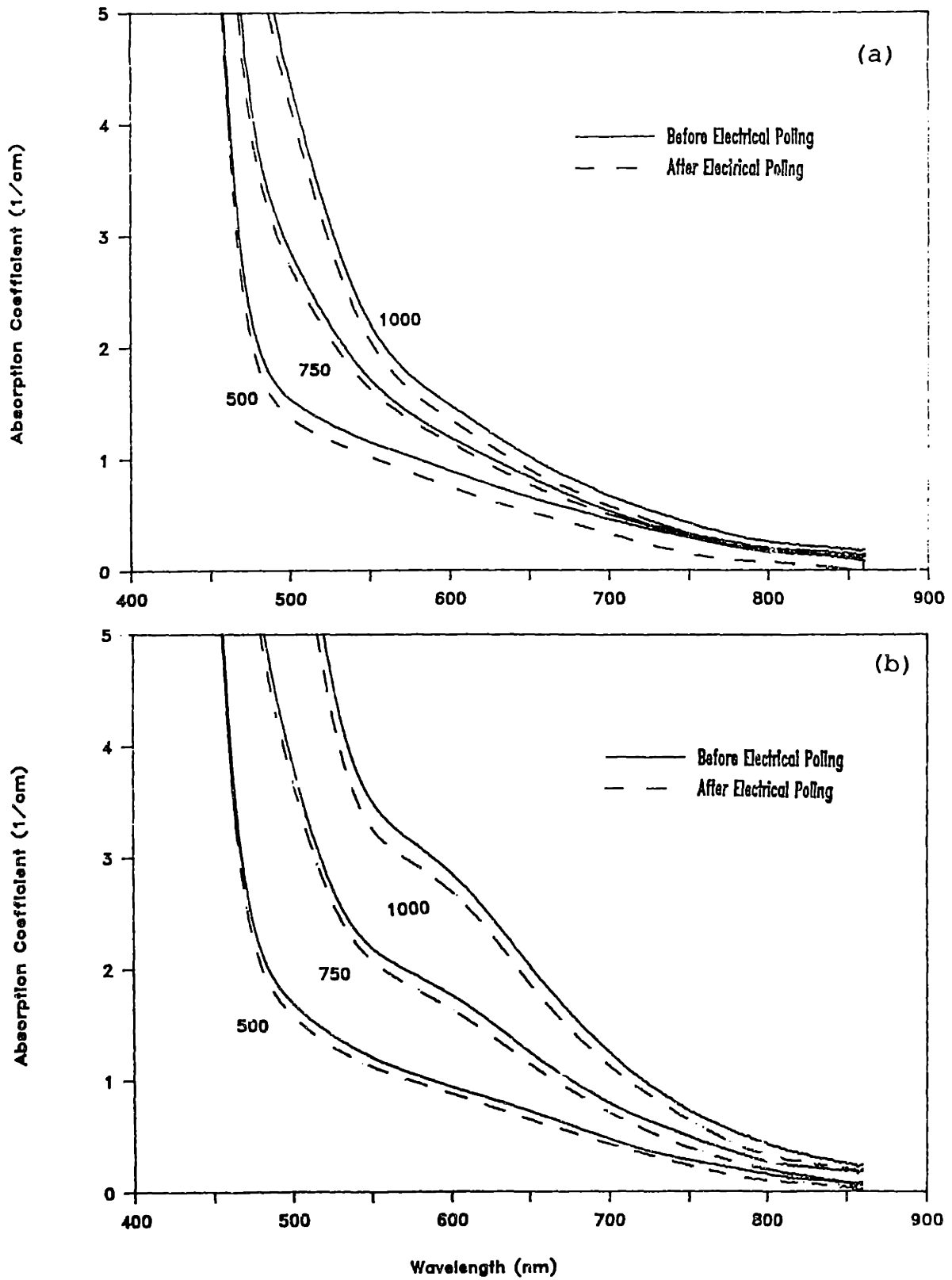


Figure 34. Effect of electrical poling on absorption spectra (crystals not shown did not survive electrical poling): (a) E parallel to c; (b) E perpendicular to c.

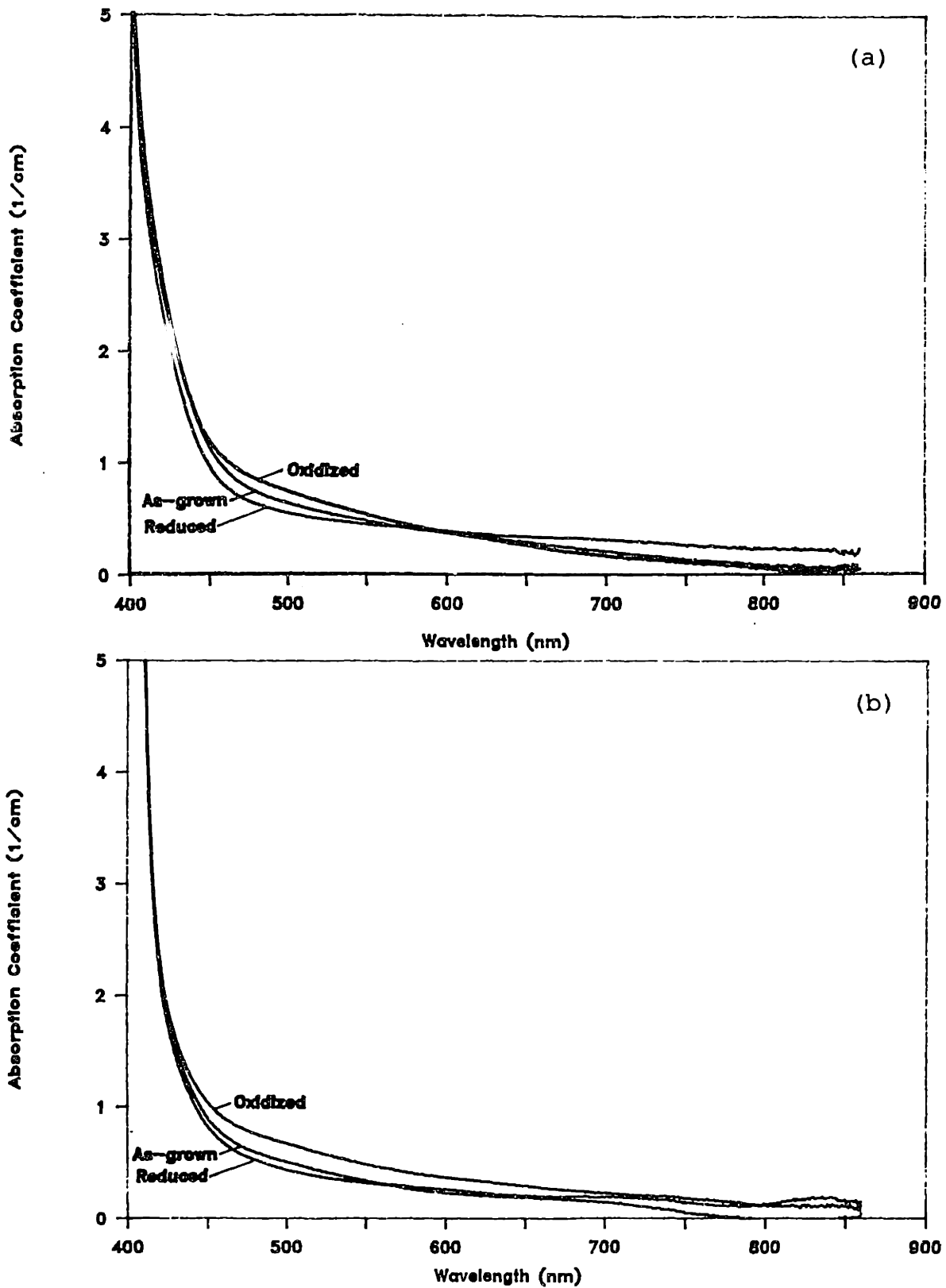


Figure 35. Effects of oxidation ($P_{O_2} = 1\text{atm}$, 800°C) and reduction ($P_{O_2} = 10^{-4}\text{atm}$, 800°C) on the absorption spectra of high purity BaTiO₃: (a) E parallel to c; (b) E perpendicular to c.

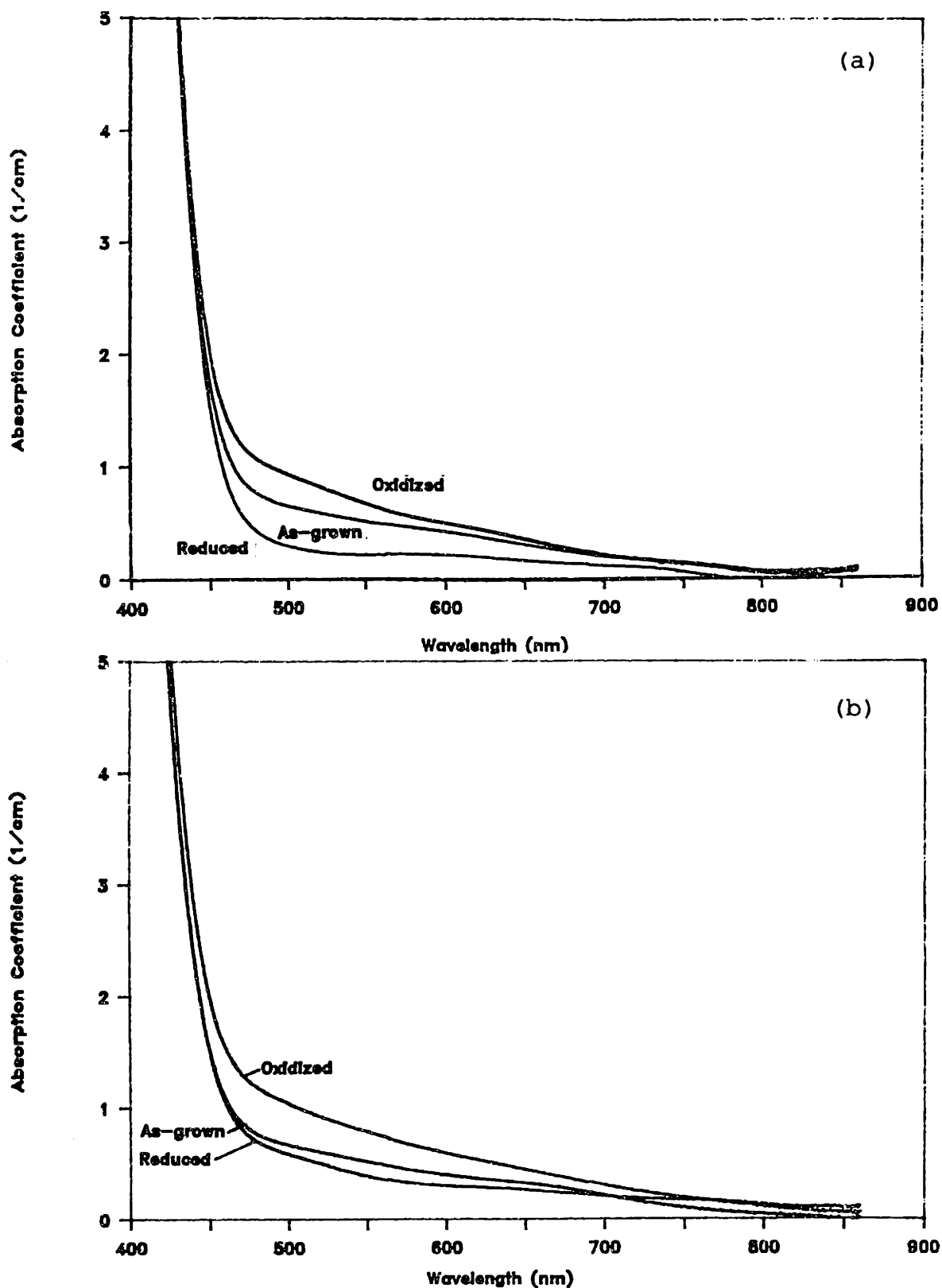


Figure 36. Effects of oxidation ($P_{O_2} = 1\text{atm}$, 800°C) and reduction ($P_{O_2} = 10^{-4}\text{atm}$, 800°C) on the absorption spectra of $\text{BaTiO}_3:50\text{ppm Fe}$: (a) E parallel to c; (b) E perpendicular to c.

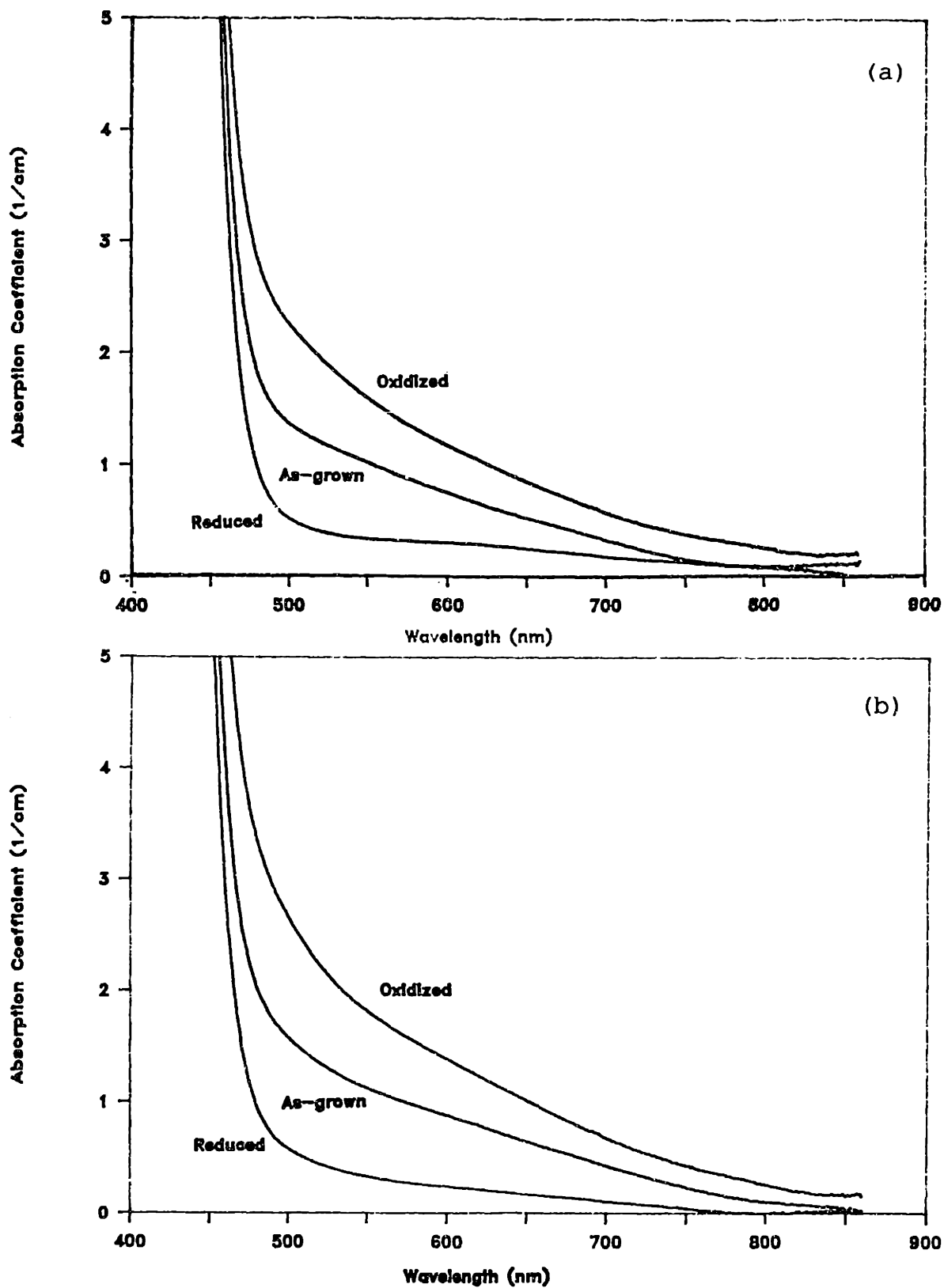


Figure 37. Effects of oxidation ($P_{O_2} = 1\text{atm}$, 800°C) and reduction ($P_{O_2} = 10^{-4}\text{atm}$, 800°C) on the absorption spectra of $\text{BaTiO}_3:500\text{ppm Fe}$: (a) E parallel to c; (b) E perpendicular to c.

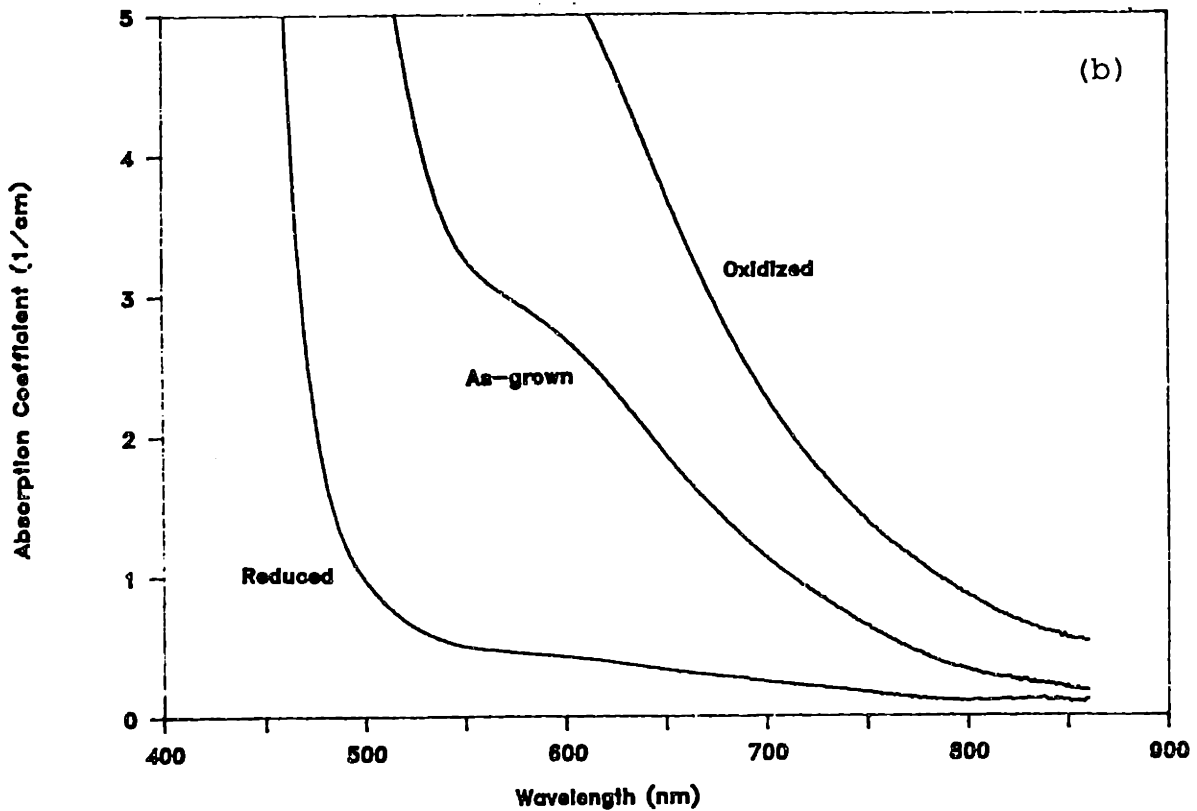
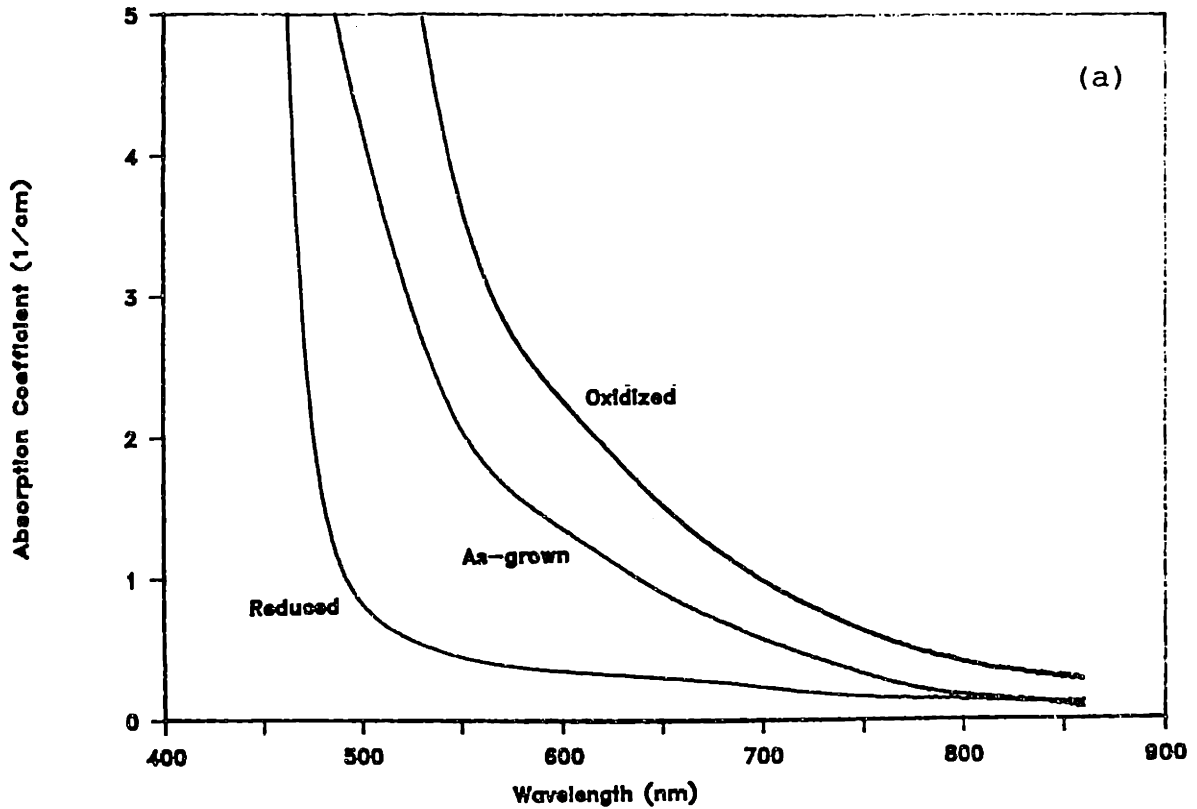


Figure 38. Effects of oxidation ($P_{O_2} = 1\text{atm}$, 800°C) and reduction ($P_{O_2} = 10^{-4}\text{atm}$, 800°C) on the absorption spectra of $\text{BaTiO}_3:1000\text{ppm Fe}$: (a) E parrallel to c; (b) E perpendicular to c.

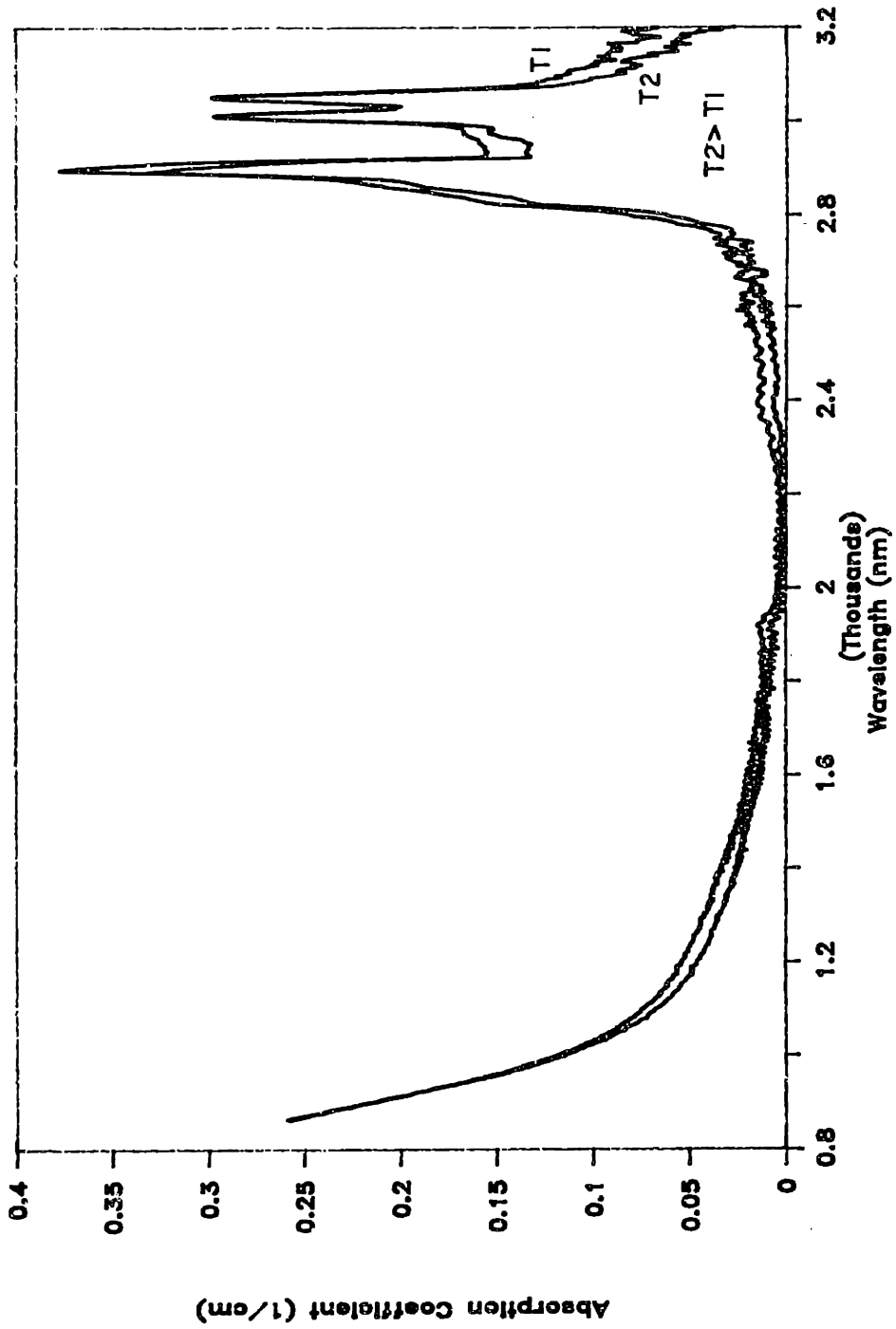
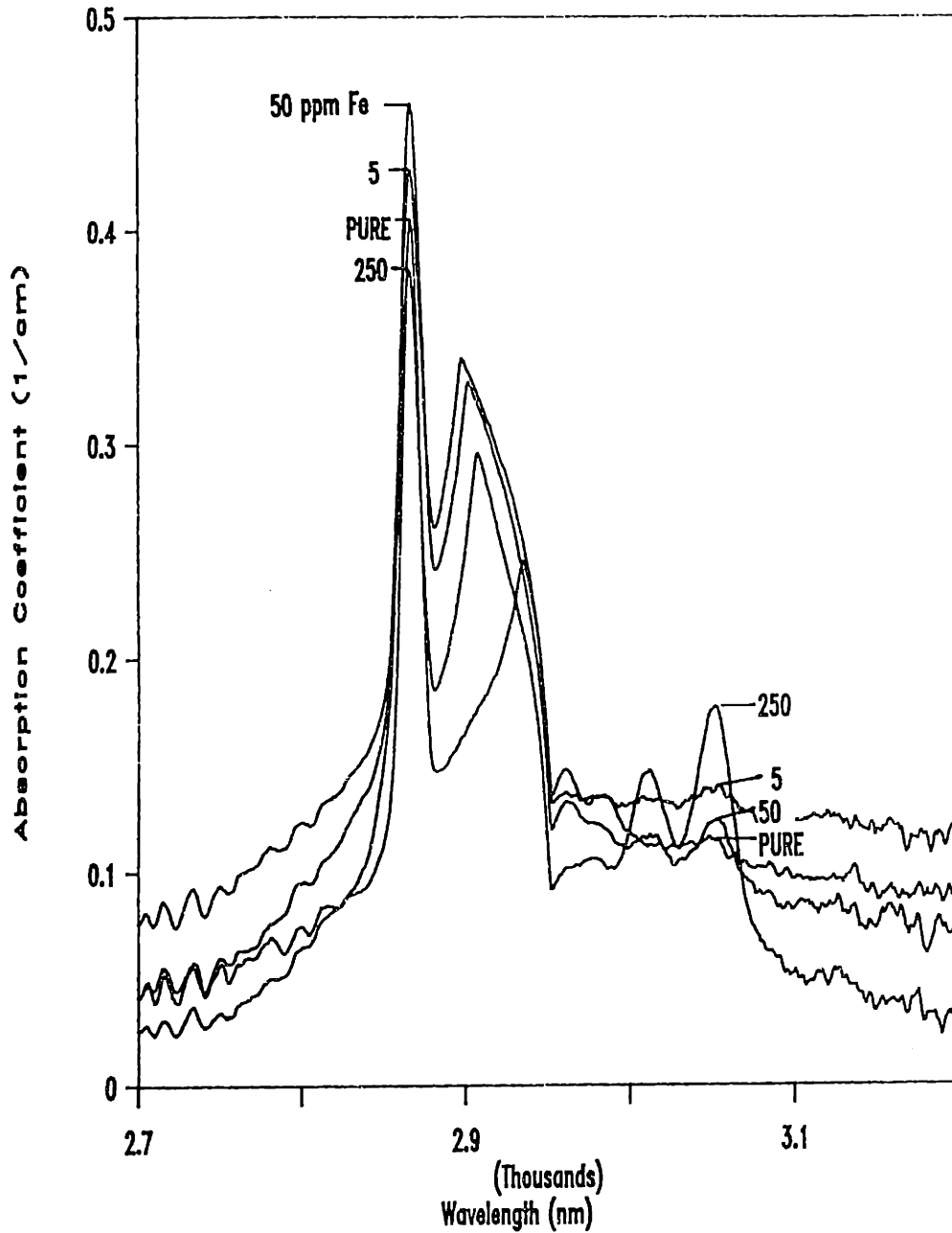


Figure 39. Typical NIR absorption spectra (860-3200nm) indicating the agreement of absorbance correction for two different thicknesses.

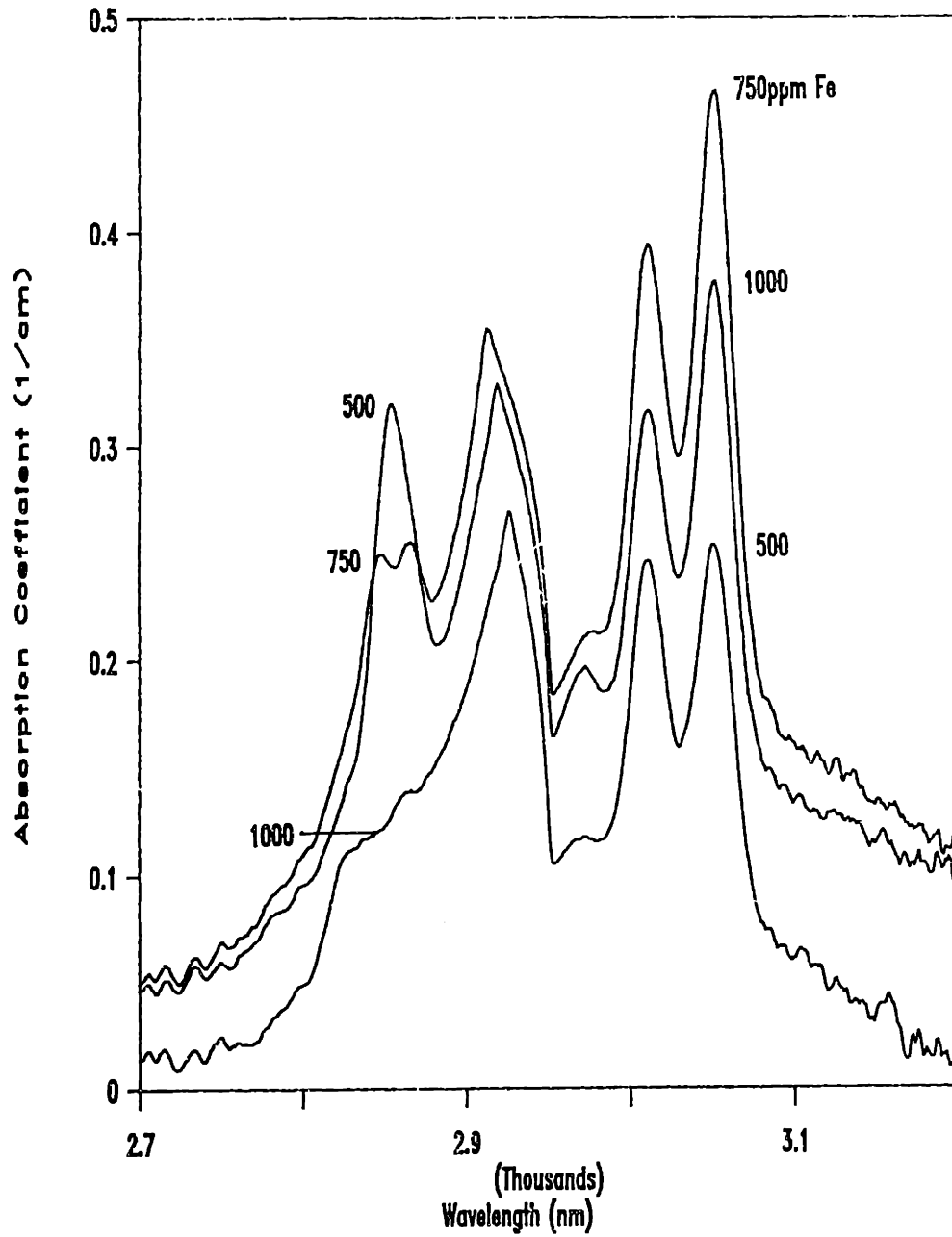
Fe-Doped Barium Titanate NIR Spectra



(a)

Figure 40. Spectral features in the NIR region between 2700 and 3200nm for BaTiO₃ doped with (a) "pure", 5, 50, 250ppm Fe; (b) 500, 750, 1000ppm Fe.

Fe-Doped Barium Titanate NIR Spectra



(b)

Barium Titanate: High Purity

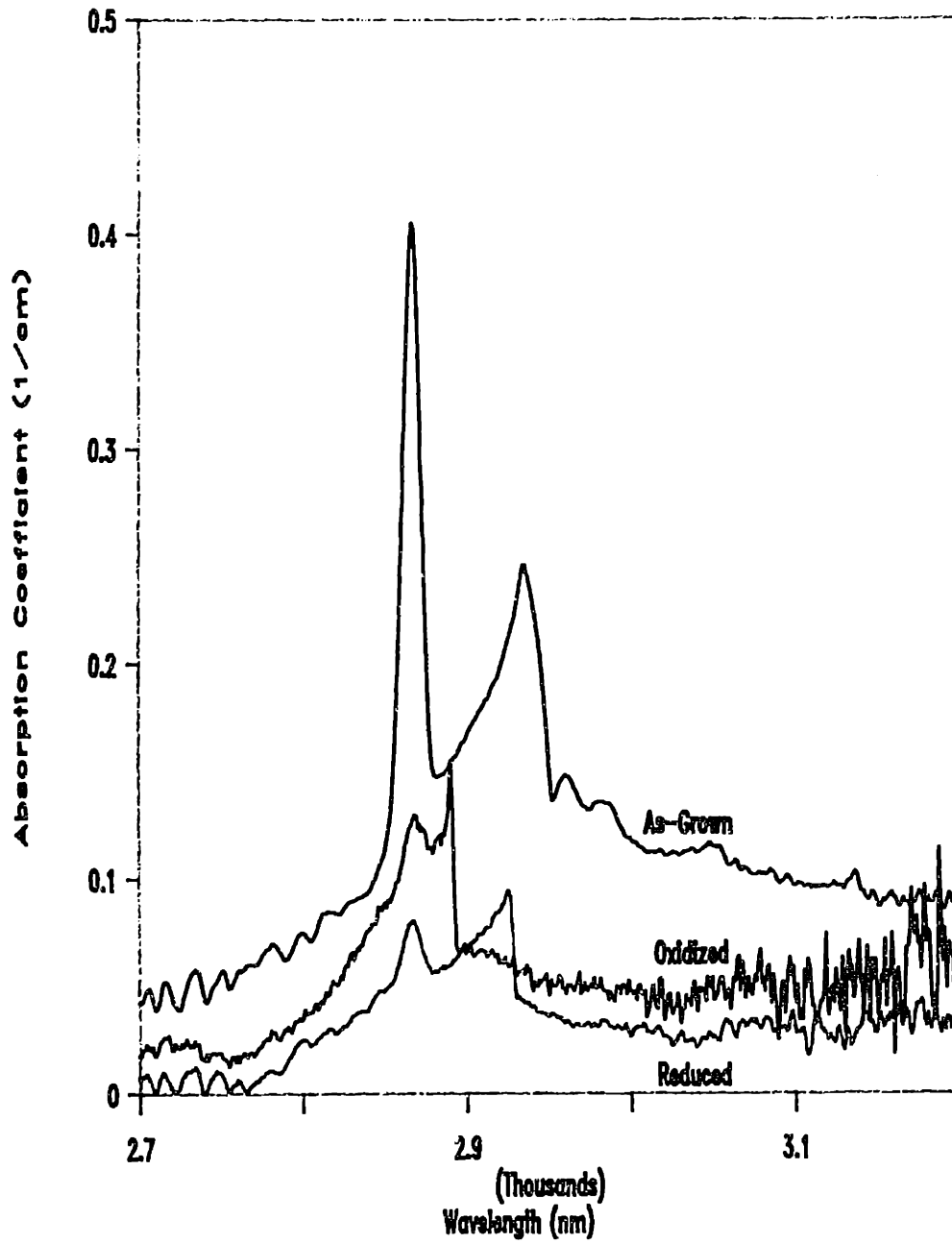


Figure 42. Effects of oxidation ($P_{O_2} = 1\text{atm}$, 800°C) and reduction ($P_{O_2} = 10^{-4}\text{atm}$, 800°C) on NIR features: High-Purity BaTiO_3 .

Barium Titanate: 50ppm Fe

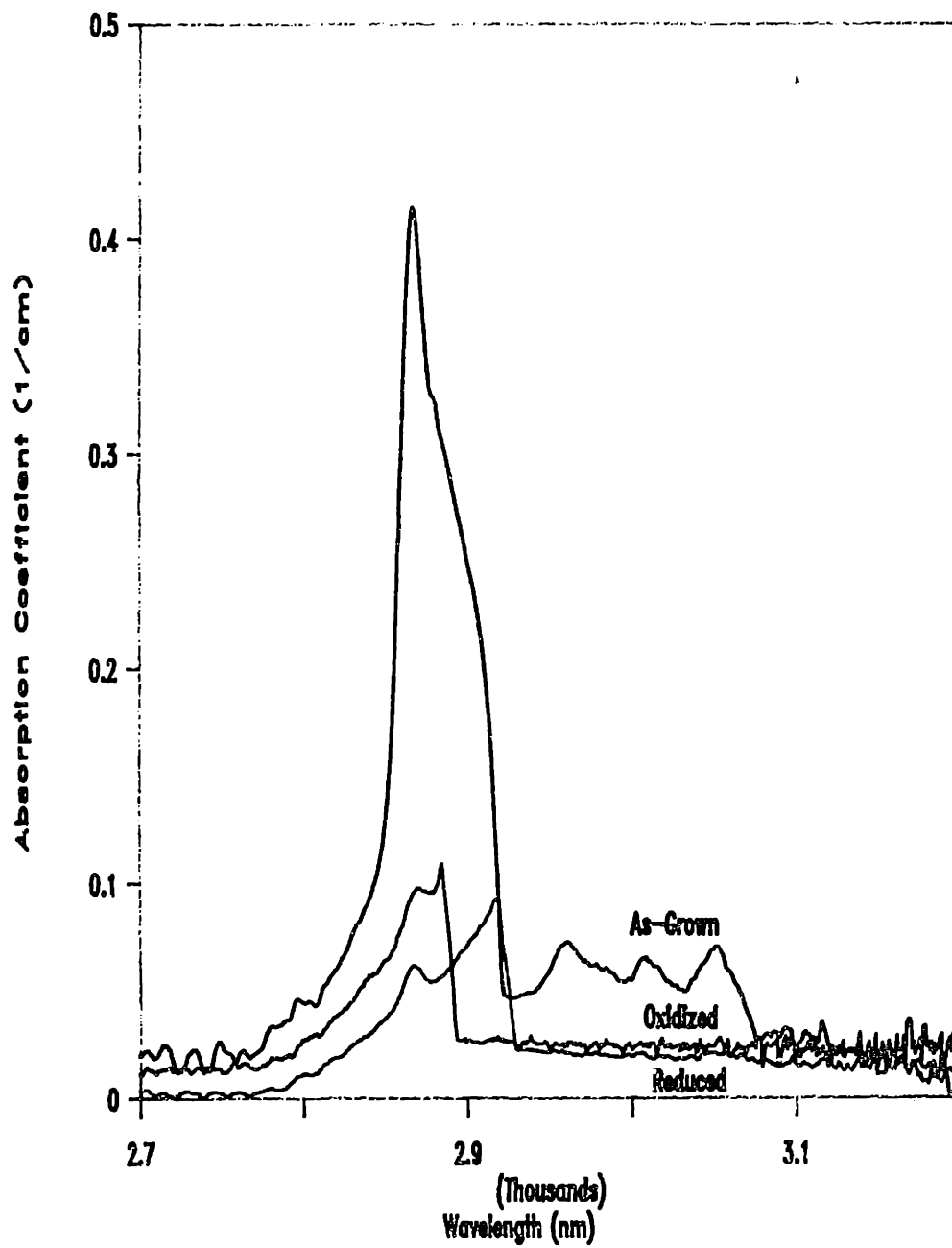


Figure 43. Effects of oxidation ($P_{O_2} = 1\text{atm}$, 800°C) and reduction ($P_{O_2} = 10^{-4}\text{atm}$, 800°C) on NIR features: $\text{BaTiO}_3:50\text{ppmFe}$.

Barium Titanate: 500ppm Fe

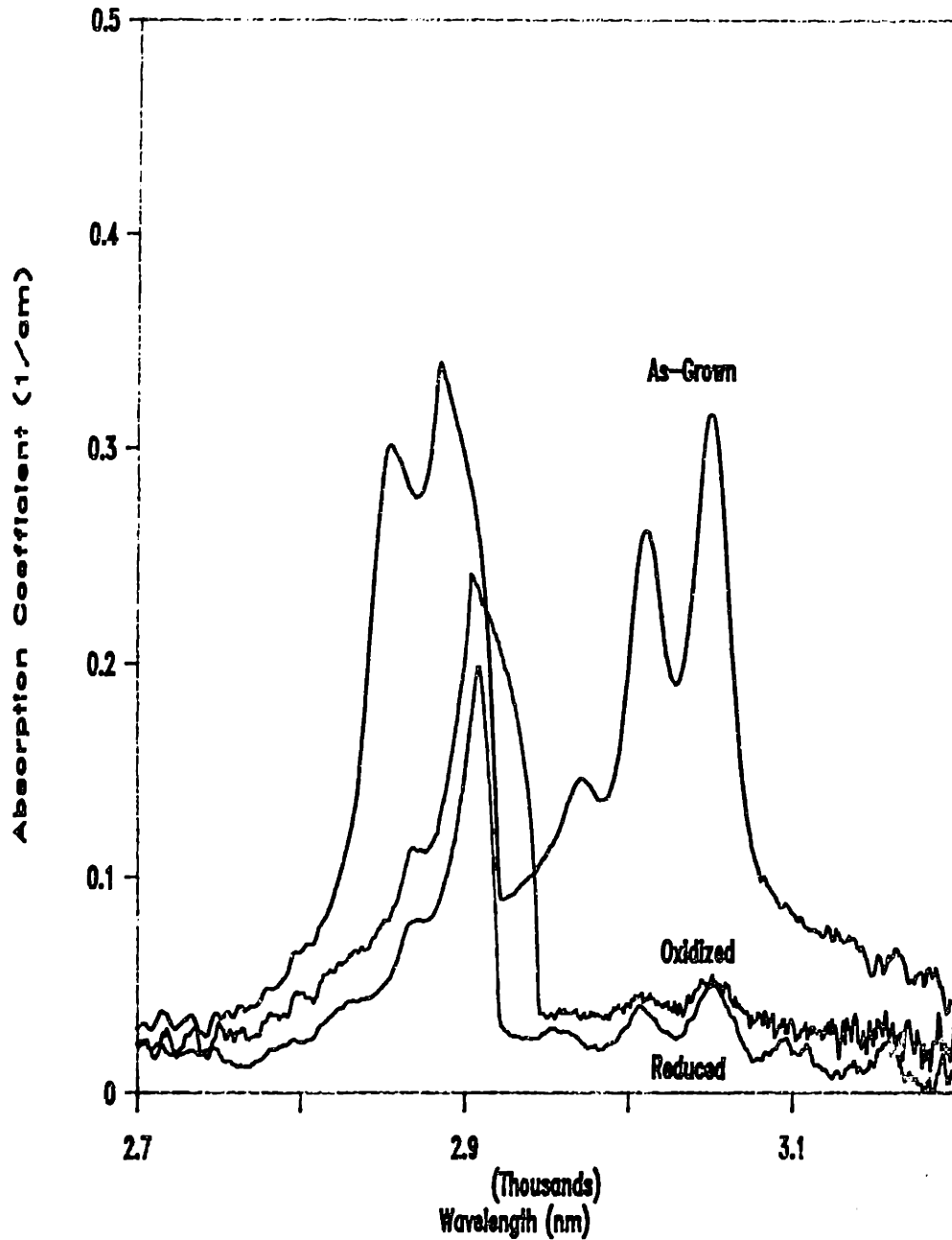


Figure 44. Effects of oxidation ($P_{O_2} = 1\text{atm}$, 800°C) and reduction ($P_{O_2} = 10^{-4}\text{atm}$, 800°C) on NIR features: $\text{BaTiO}_3:500\text{ppm Fe}$.

Barium Titanate: 1000ppm Fe

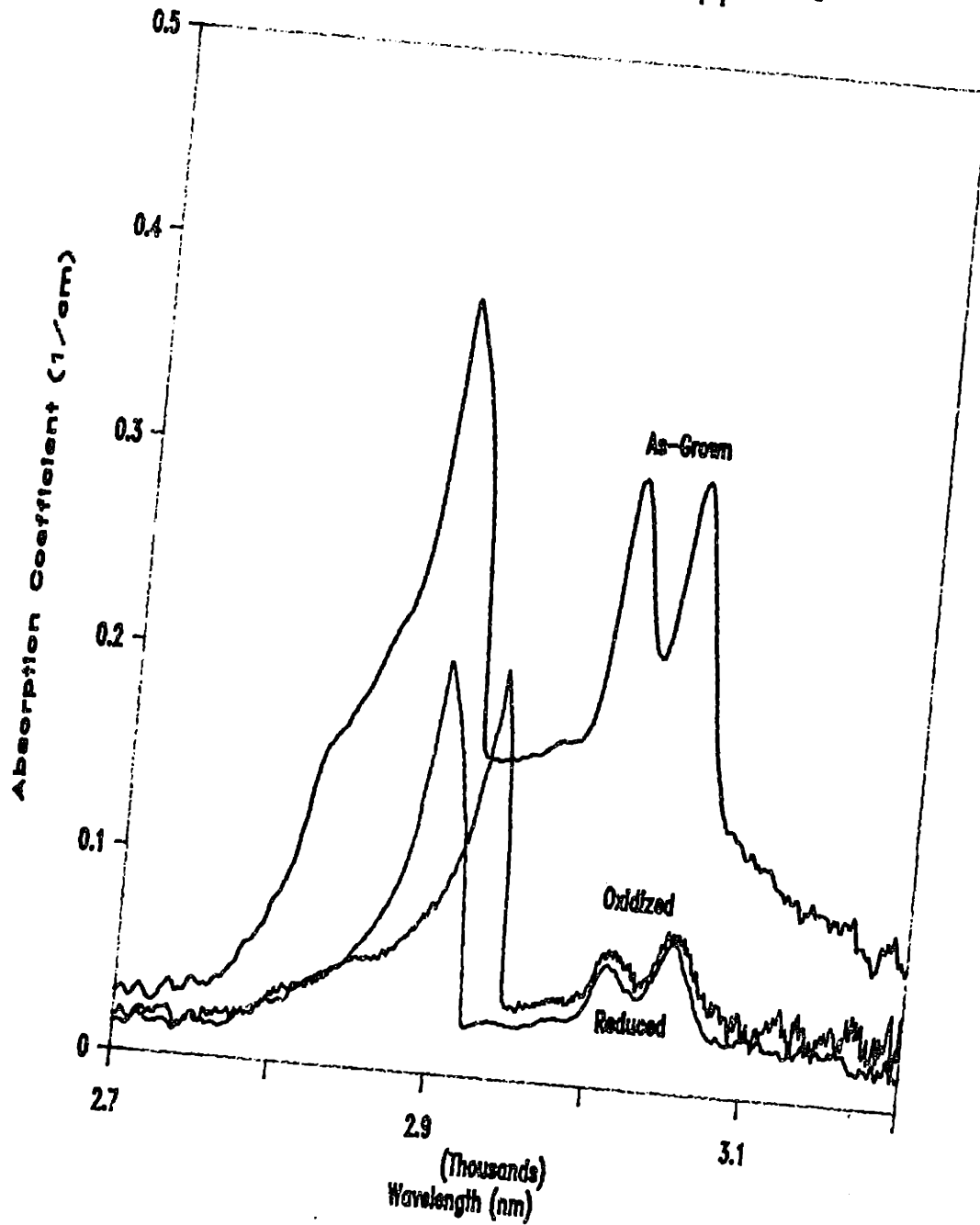


Figure 45. Effects of oxidation ($P_{O_2} = 1 \text{ atm}$, 800°C) and reduction ($P_{O_2} = 10^{-4} \text{ atm}$, 800°C) on NIR features: $\text{BaTiO}_3:1000\text{ppm Fe}$.

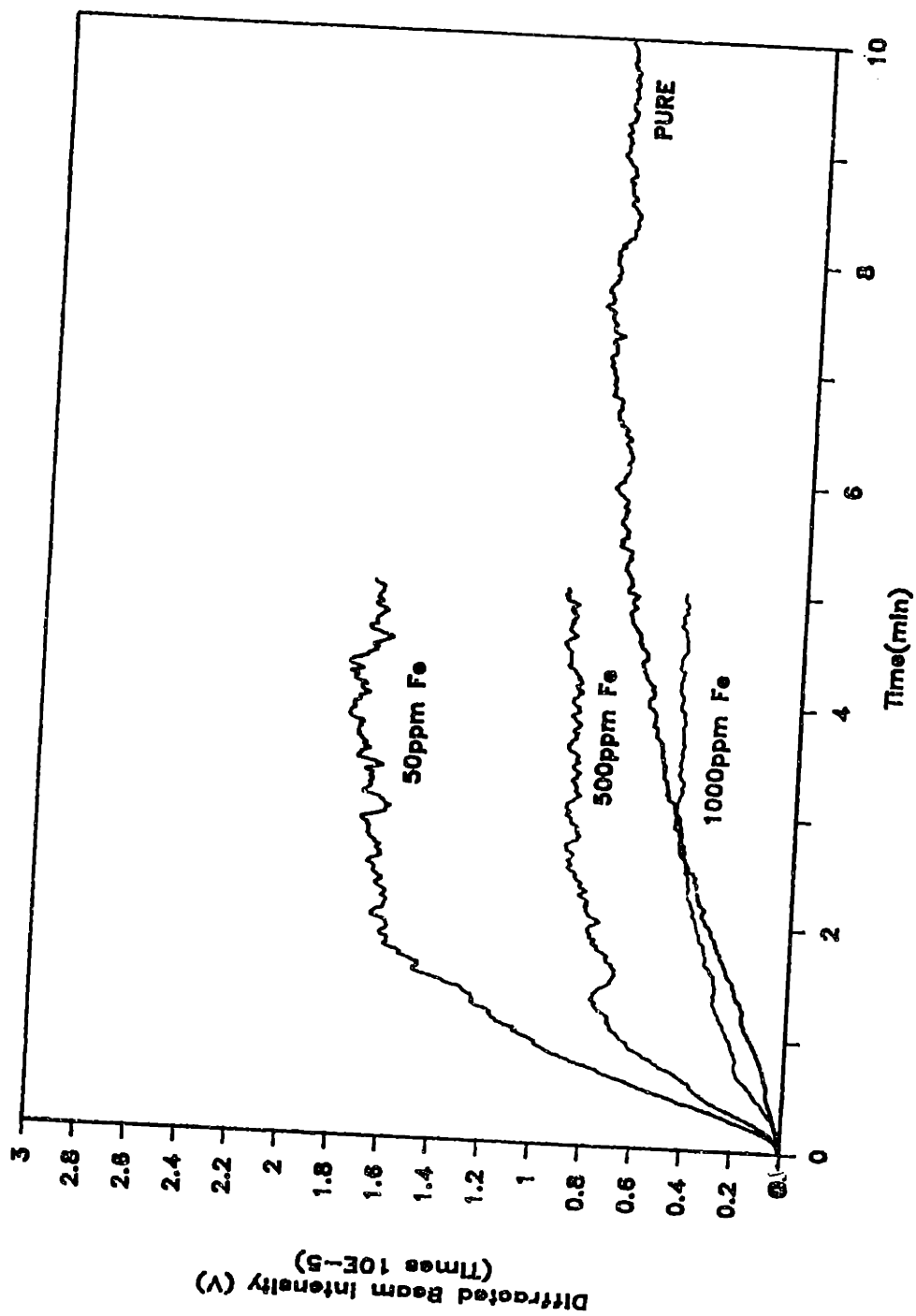


Figure 46. Diffracted beam intensity vs. time for as-grown BaTiO₃:High-Purity, 50, 500, 1000ppm Fe.

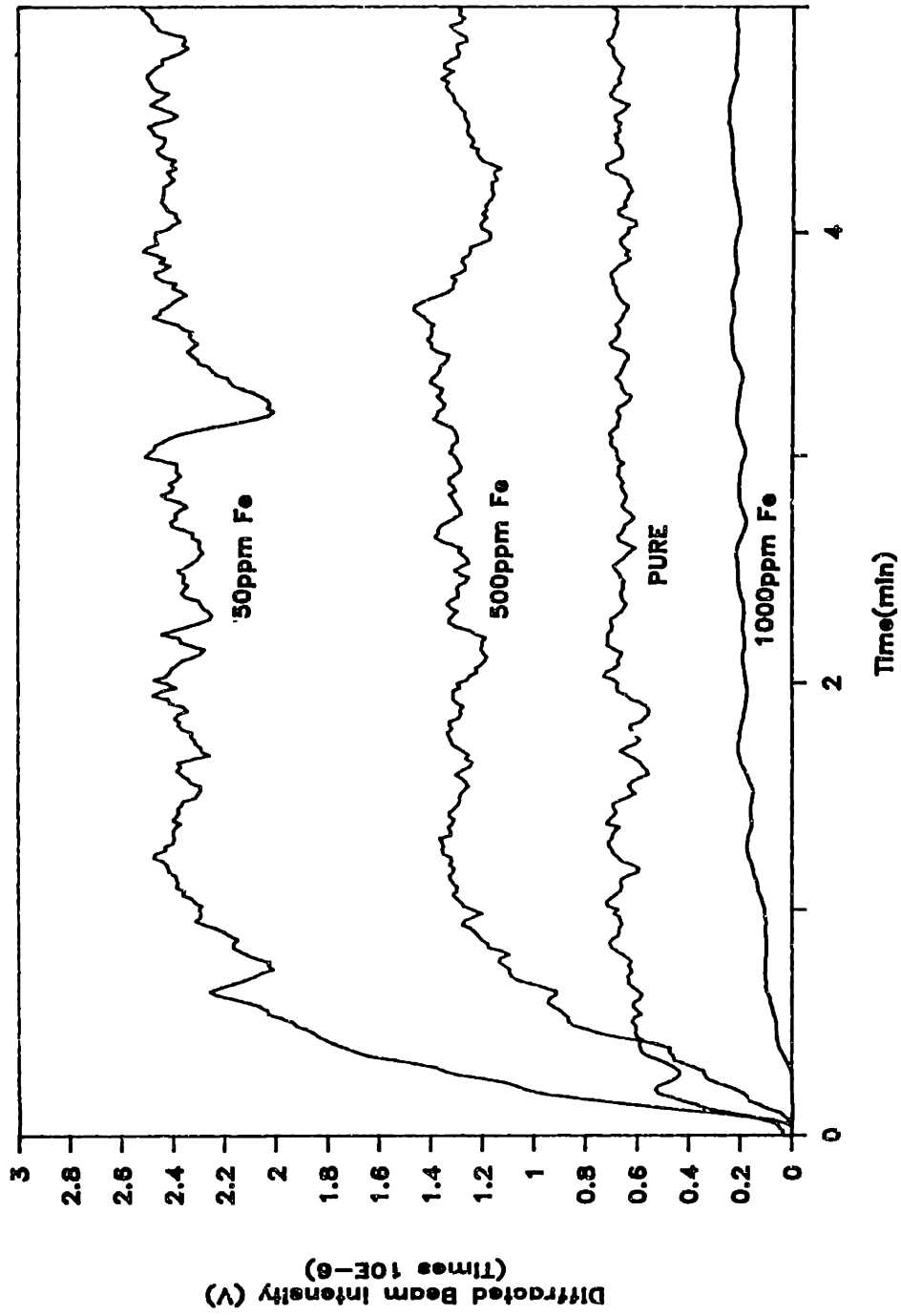


Figure 47. Diffracted beam intensity vs. time for oxidized BaTiO₃:High-Purity, 50, 500, 1000ppm Fe.

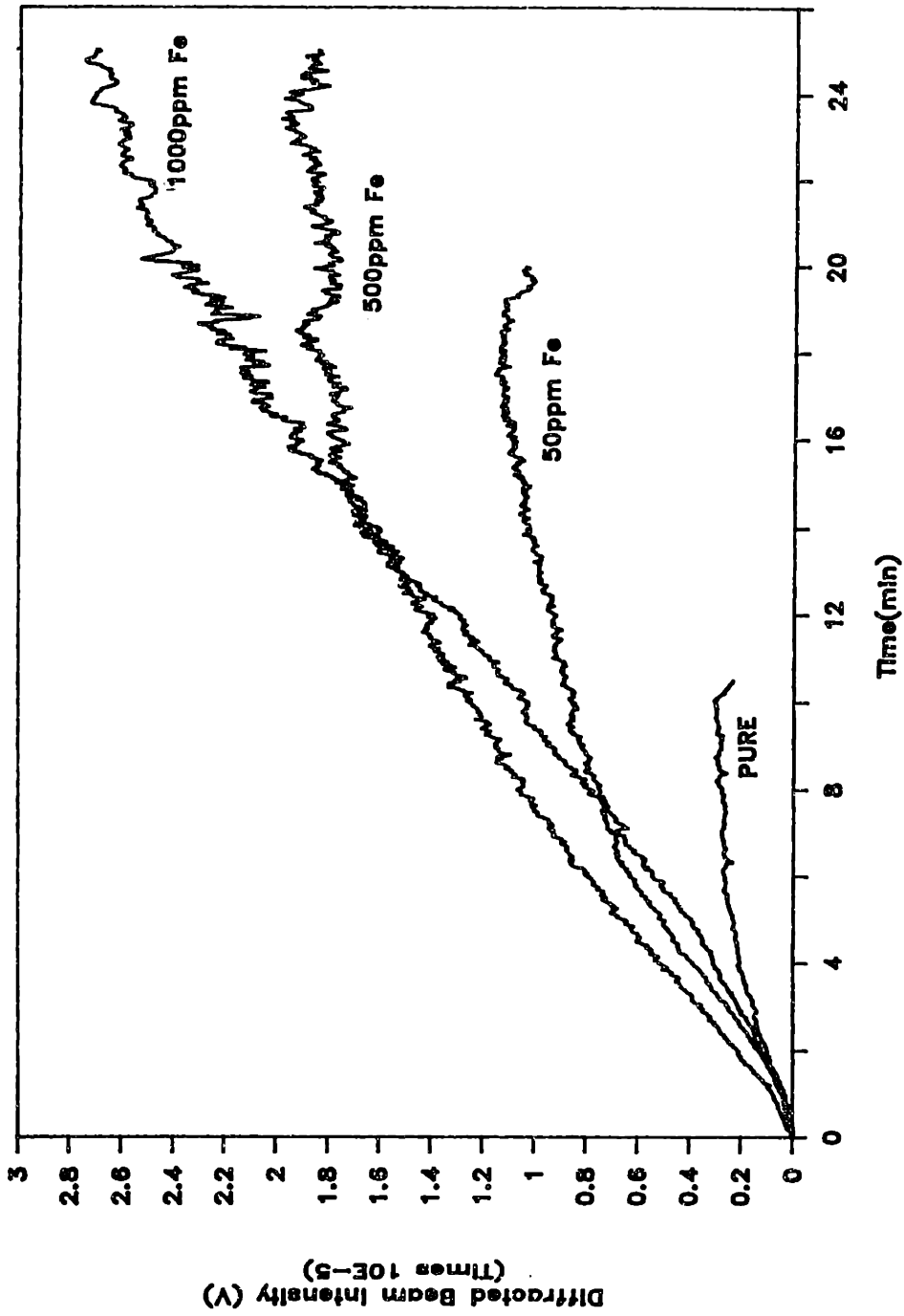


Figure 48. Diffracted beam intensity vs. time for reduced BaTiO_3 :High-Purity, 50, 500, 1000ppm Fe.

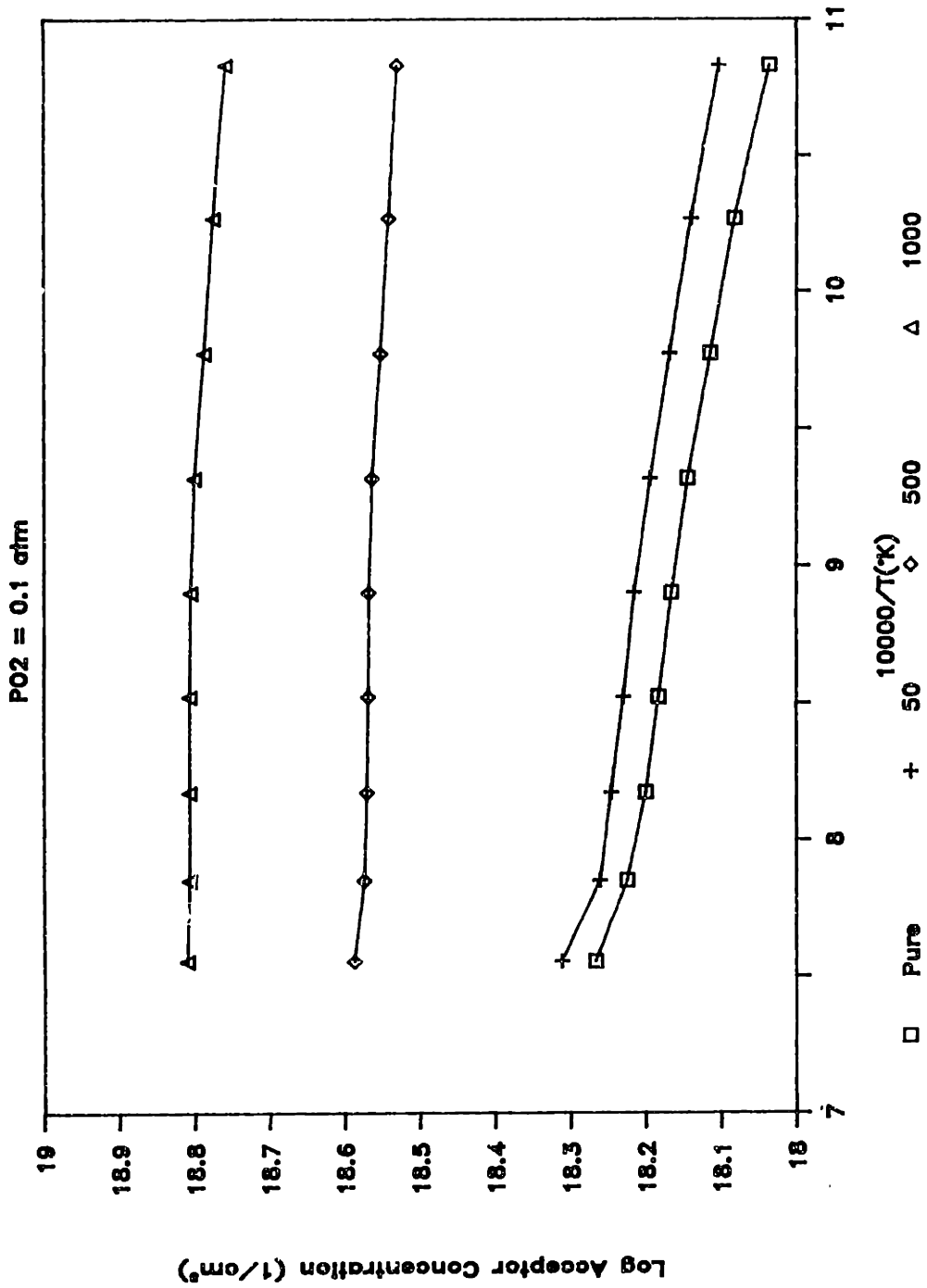


Figure 49. Slight temperature dependence of acceptor concentrations derived from the p-type conductivities of high-purity, 50, 500, and 1000ppm Fe-doped $BaTiO_3$ at $PO_2 = 0.1 \text{ atm}$.

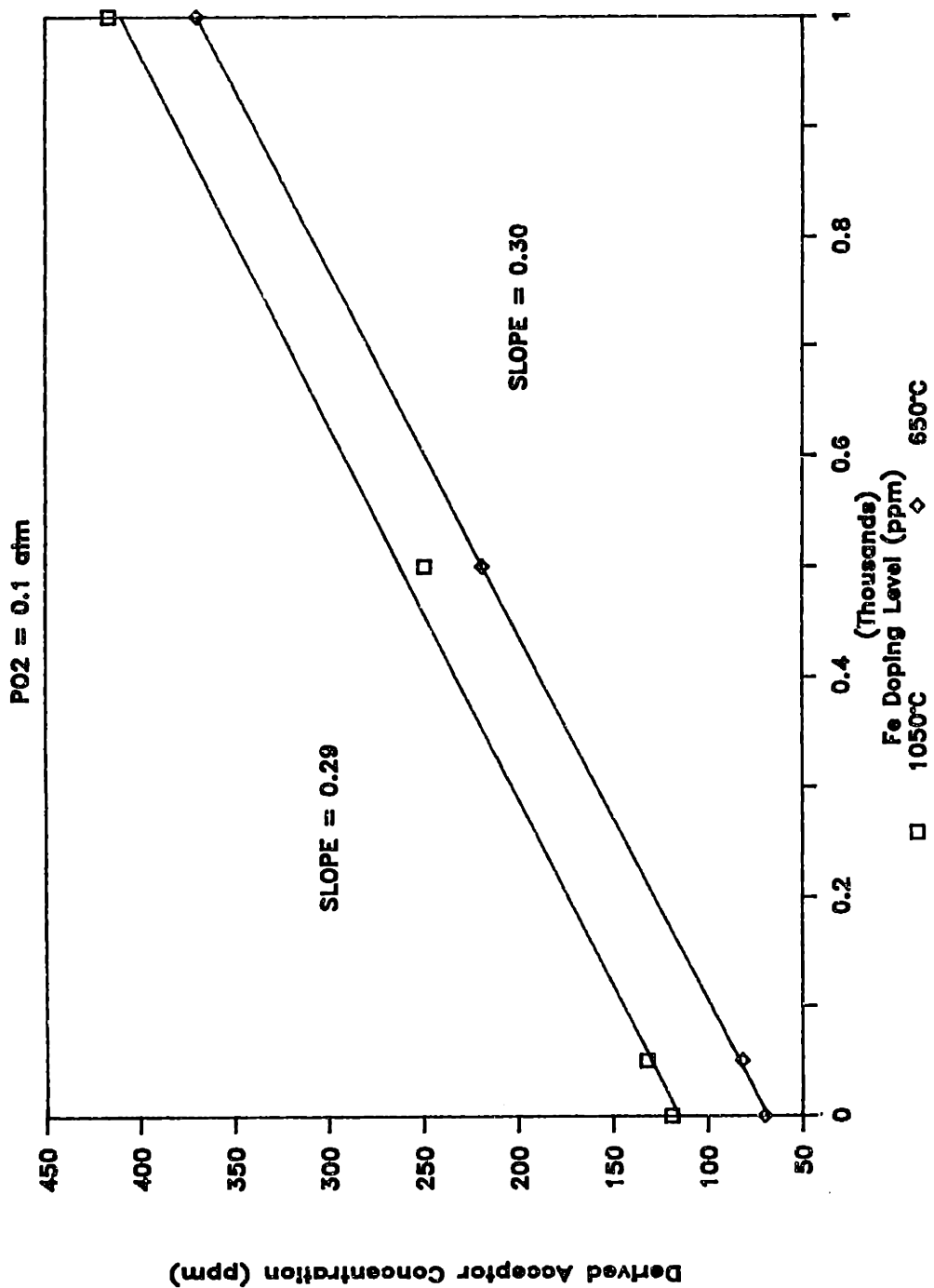


Figure 50. Derived acceptor content vs. Fe doping level. Slope indicates that the added Fe is only 30% effective as an electronic acceptor.

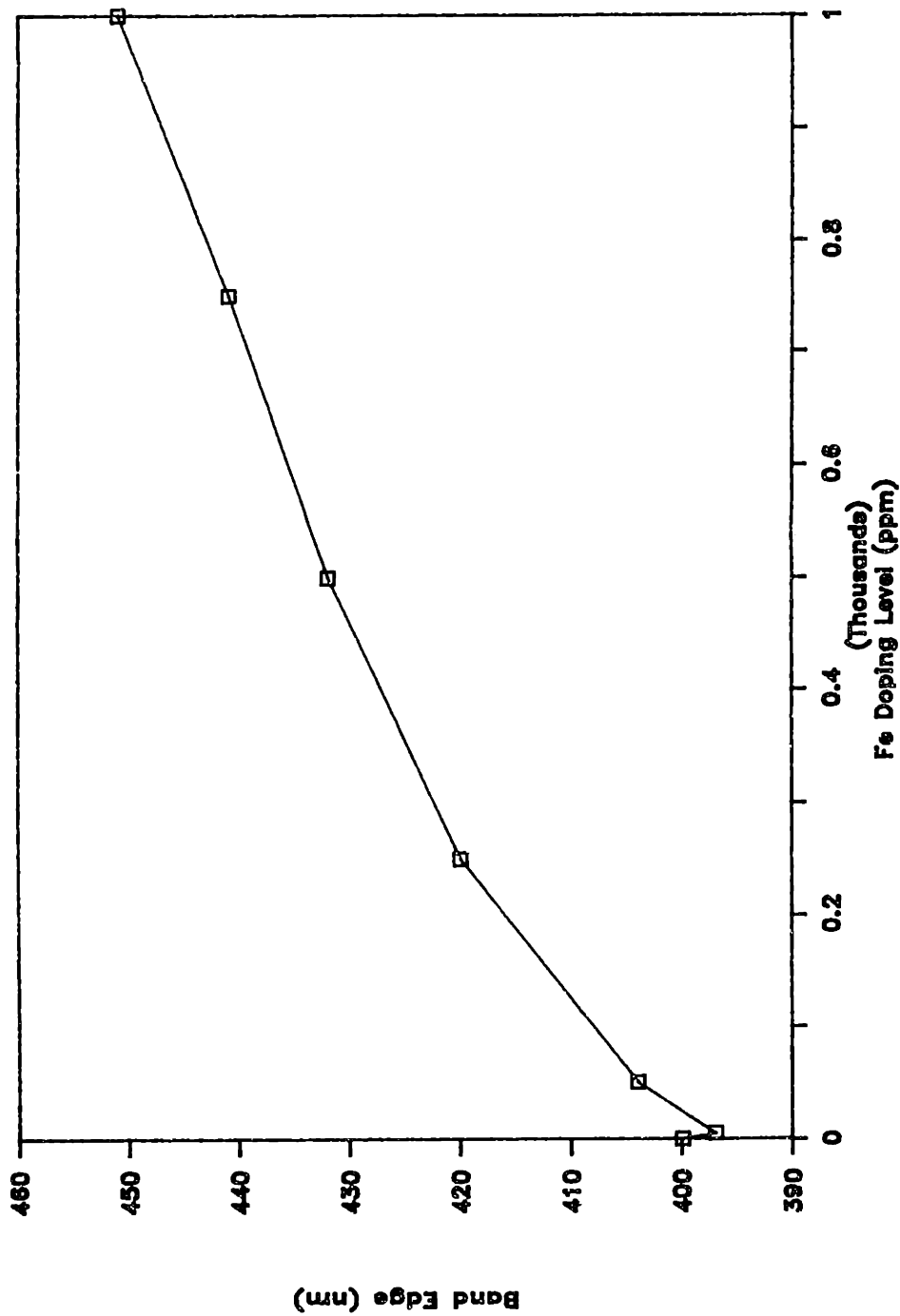


Figure 51. Systematic shift in the optical band edge (taken at $\alpha = 19\text{cm}^{-1}$) with increasing Fe content.

Log Alpha 620 vs Log [Fe]

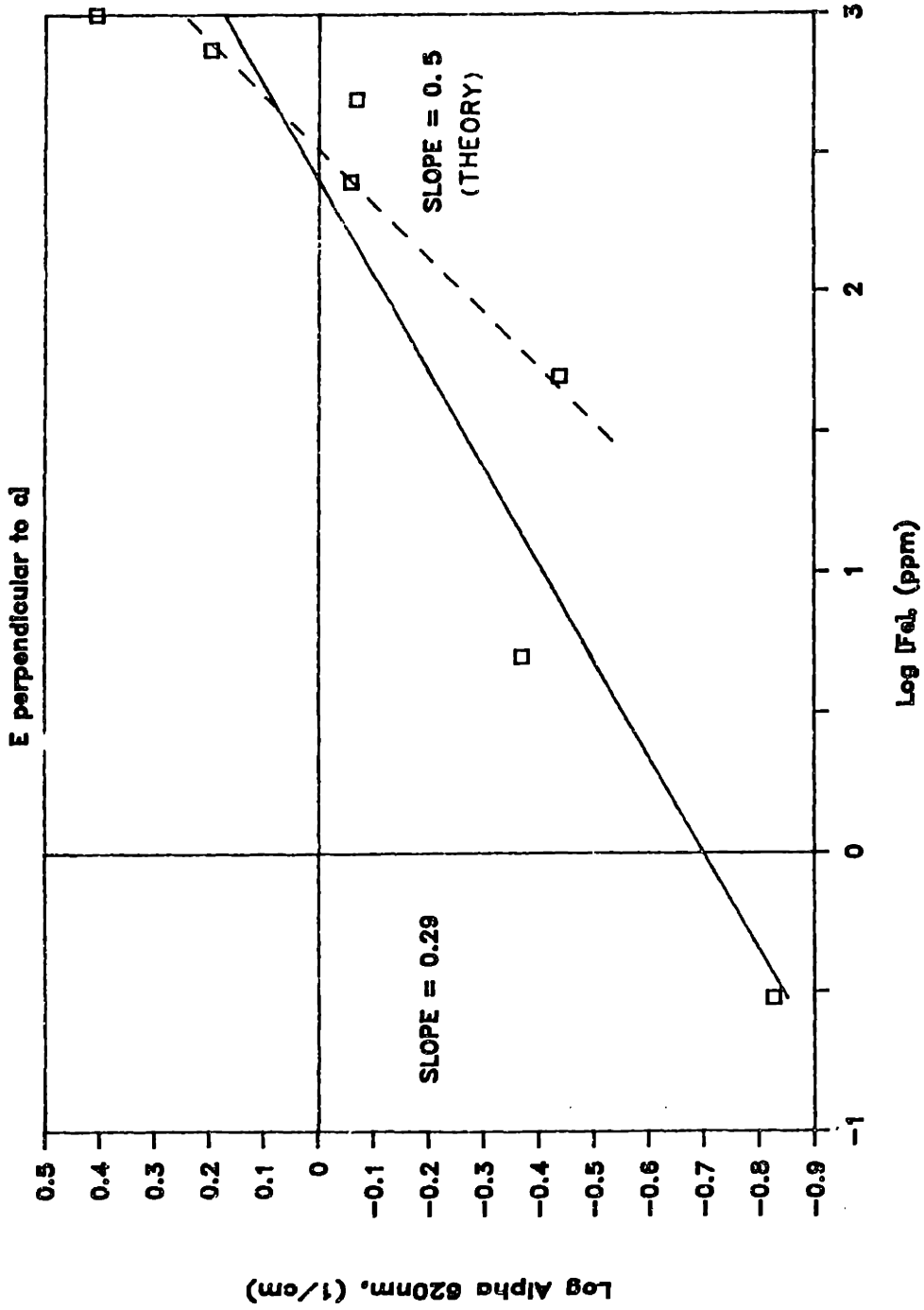


Figure 52. $\text{Log}\alpha_{620}$ vs. $\text{log}[\text{Fe}]_{\text{tot}}$, illustrating the trend toward the theoretical $1/2$ dependence at higher Fe concentrations.

Log Alpha (620nm) vs Log P_{O2}

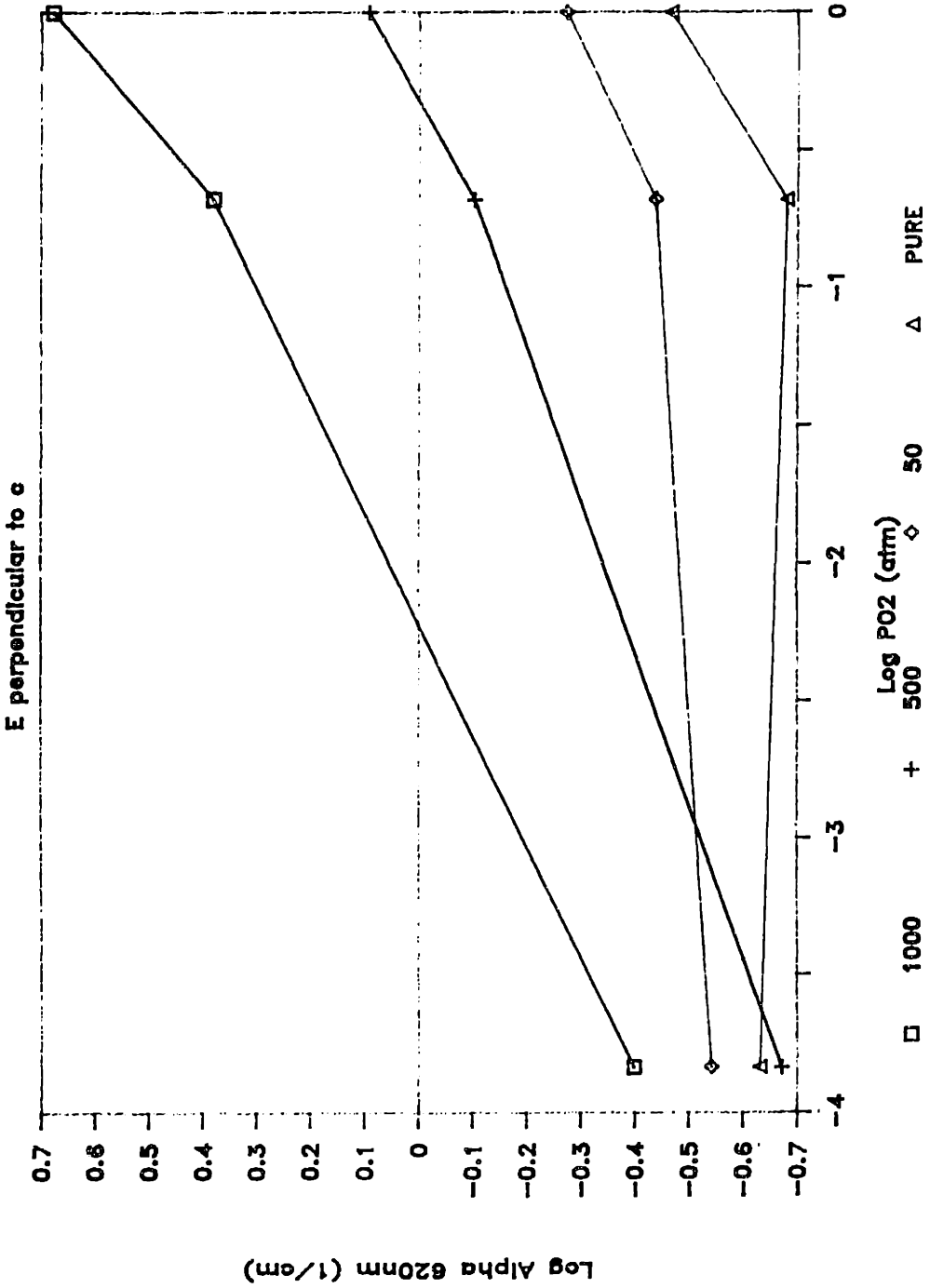


Figure 53. P_{O2}-dependence of the 620nm absorption coefficient (Fe⁴⁺) approaching the predicted 1/4 slope with increasing Fe content.

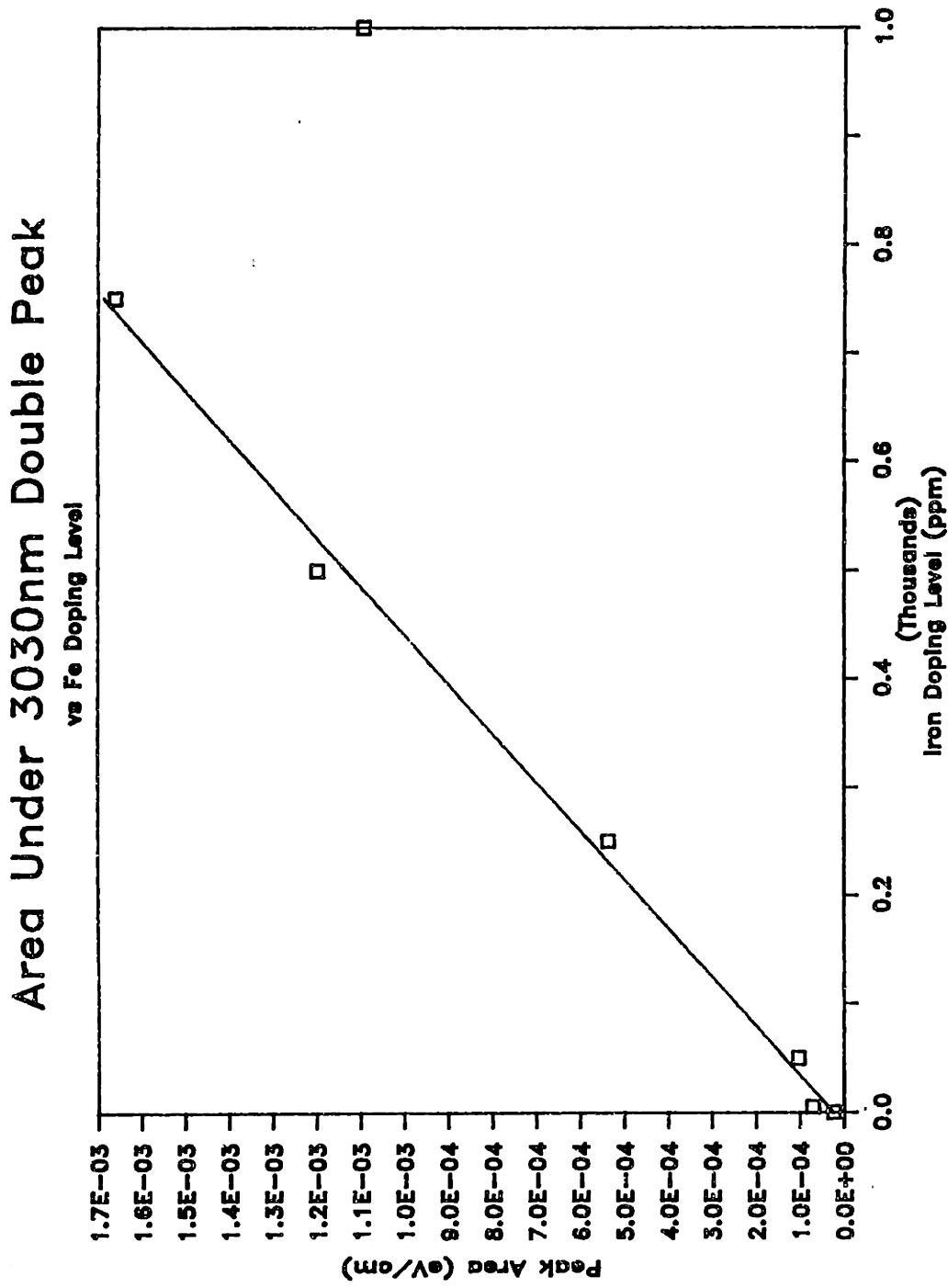


Figure 54. Linear dependence of 3010/3050nm peak area on Fe content, which saturates near 1000ppm Fe.

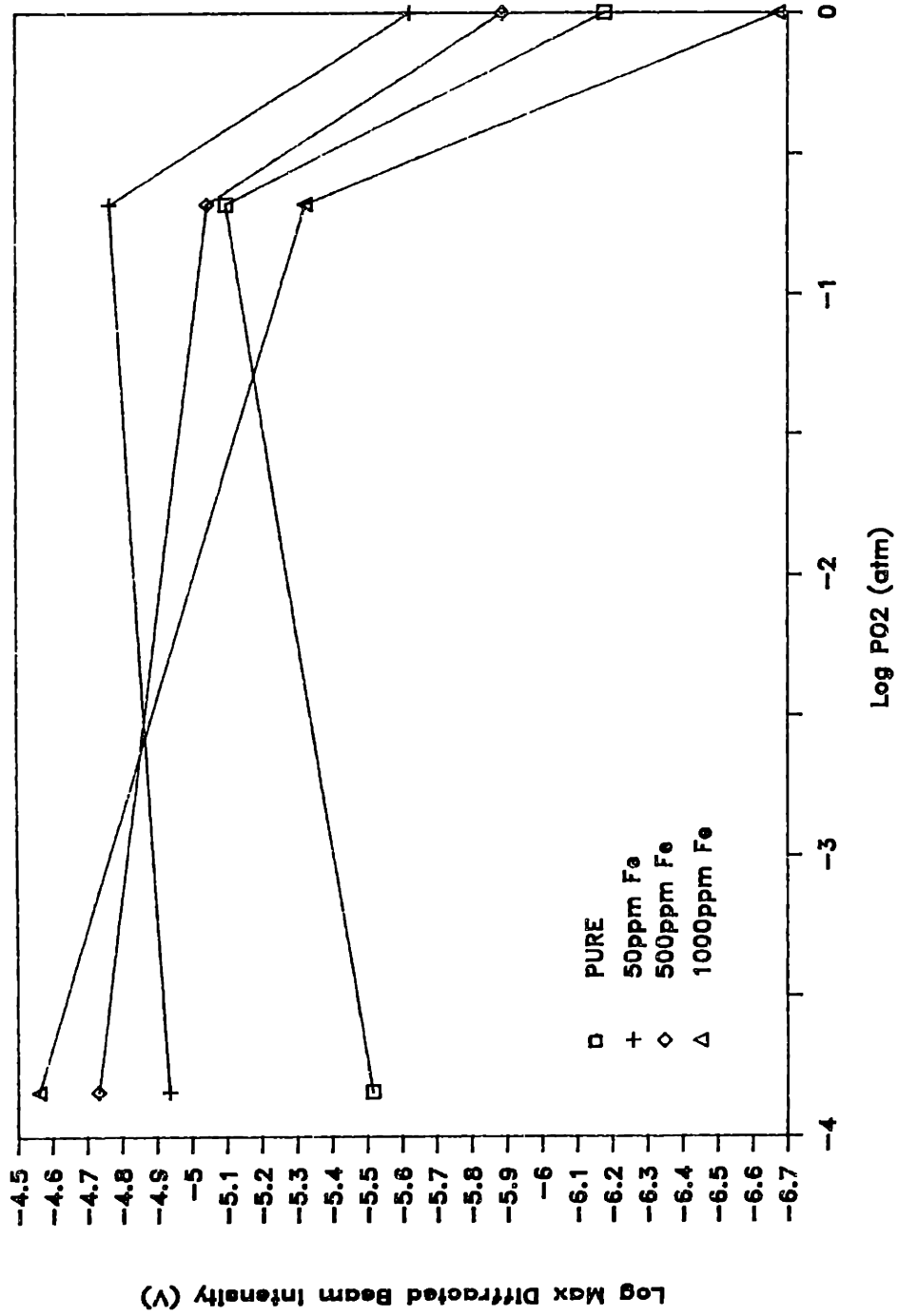


Figure 55. PO₂ dependence of the maximum diffracted beam intensity for "pure", 50, 500, and 1000ppm Fe-doped BaTiO₃ crystals.

APPENDIX 1

SINGLE CRYSTAL GROWTH

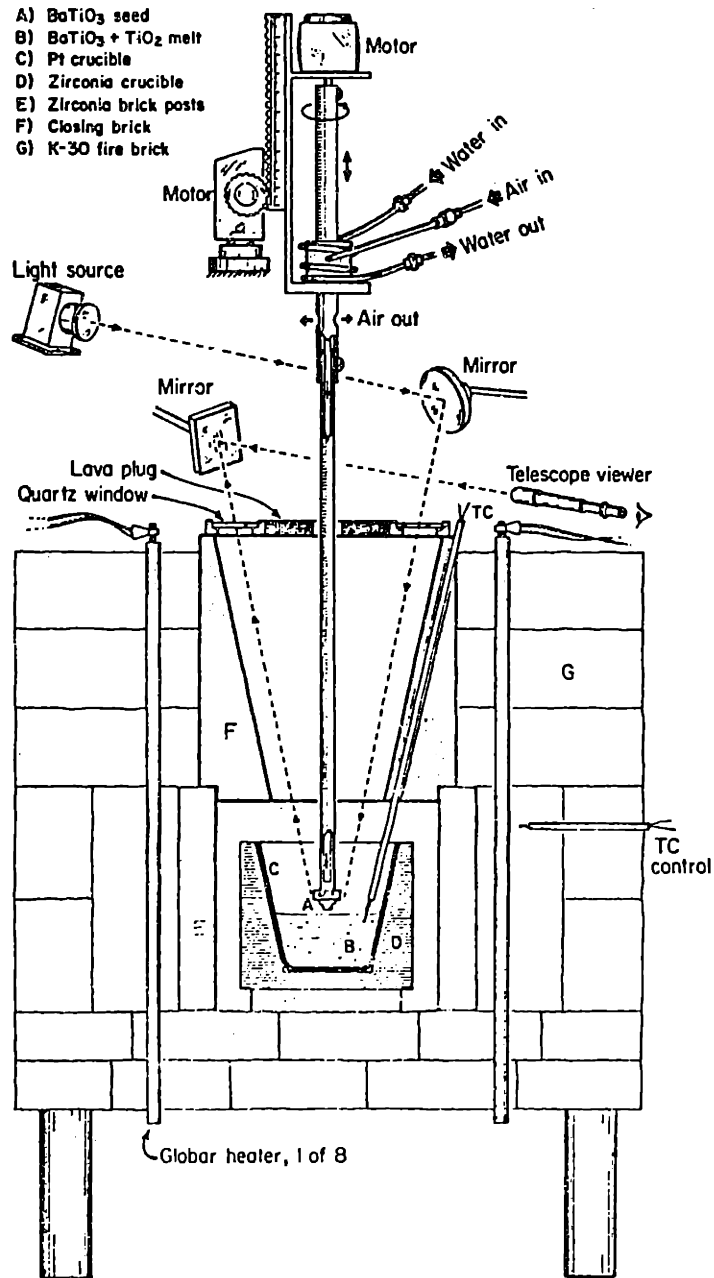


Figure A1.1 Schematic of furnace used for single crystal growth.

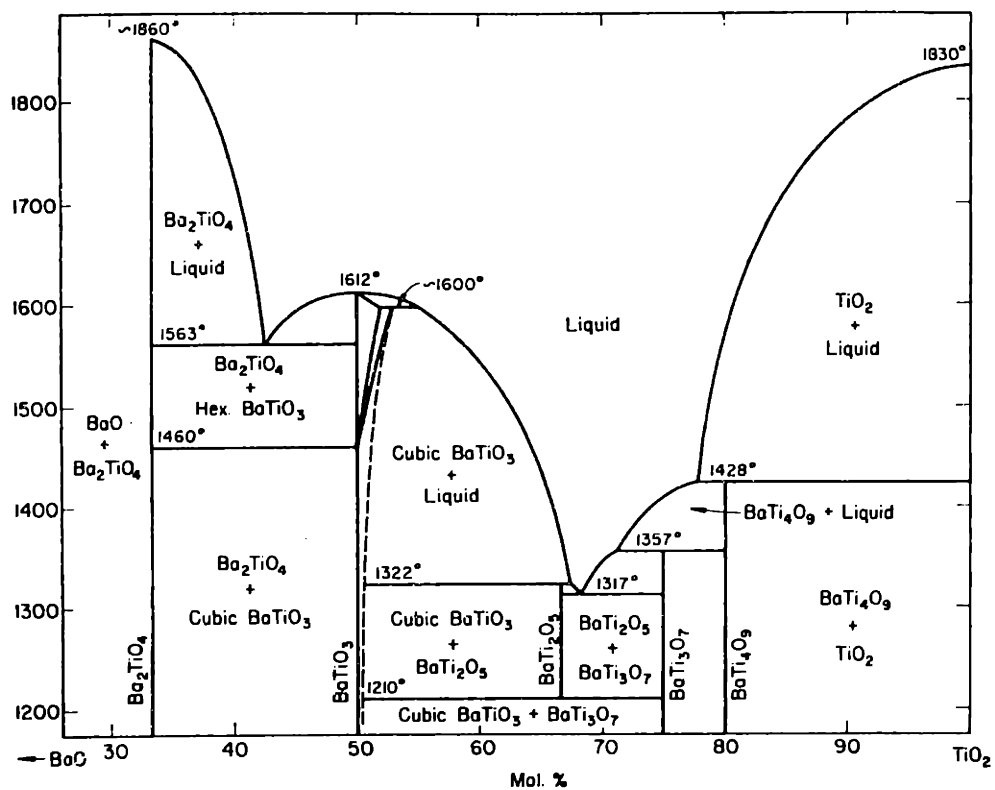


FIG. 213.—System BaO-TiO₂.

D. E. Rase and Rustum Roy, The Pennsylvania State University, College of Mineral Industries; Eighth Quarterly Progress Report, April 1 to June 30, Appendix II, p. 32 (1953); *J. Am. Ceram. Soc.*, 38 [3] 111 (1955); m.p. of BaTiO₃ given as 1618°C.

Figure A1.2 BaO-TiO₂ phase diagram.

Table A1. Details of BaTiO₃ crystal growth runs.
(Resulting crystals shown in Figure A1.3)

Run#	[Fe] (ppm)	Seeding Temp. (°C)	Cooling (°C/min)	Pulling (mm/hr)	Crystal wt. (g)	Comments
1434	Pure	1368	0.2 (25h) 0.5 (80h)	0.2	21.28	Good crystal, small
1437	Pure	1382	0.2 (25h) 0.5 (100h)	0.15	29.13	Added TiO ₂ , slow cool. (1°C/hr) thru T _c . Stressed wouldn't pole
1440	Pure	1386	0.2 (30h) 0.5 (101h)	0.15	33.01	Slow cool thru T _c stressed, wouldn't pole
1442	5	1387	0.2 (35h) 0.5 (116h)	0.15	34.51	Slow cool thru T _c
1443	50	1385	0.2 (35h) 0.5 (125h)	0.15	32.50	Slow cool thru T _c
1446	50	1392	0.2 (30h) 0.5 (124h)	0.15	36.59	Slow cool thru T _c (2°C/hr)
1448	250	1388	0.2 (30h) 0.5 (112)	0.16	34.92	Cooled 20°C/hr to 485°C, 60°C to R.T.
1451	250	1389	1 (3h) 0.3 (30h) 0.3 (30h)	0.22 0.1		Slow cool thru T _c (grown by Doyle Temple)
1453	500	1382	0.2 (30h) 0.5 (62h) 0.5 (60h)	0.16 0.10	38.40	Cooled 20°C/hr to 485°C, 60°C to R.T., excellent crystal

Table A1. (continued)

Run#	[Fe] (ppm)	Seeding Temp. (°C)	Cooling (°C/min)	Pulling (mm/hr)	Crystal wt. (g)	Comments
1457	750	1386	0.2 (30h) 0.5 (62h) 0.5 (62h)	0.16 0.10	42.05	Cooled 20°C/hr to 485°C, 60°C to R.T., excellent crystal
1459	1000	1386	0.2 (30h) 0.5 (62h) 0.5 (74h)	0.16 0.10	44.11	Cooled 20°C/hr to 485°C, 60°C to R.T., badly cracked
1462	1000	1389	0.2 (25h) 0.5 (62h) 0.5 (70h)	0.16 0.10	40.27	Cooled 20°C/hr to 485°C, 60°C to R.T.

0 1 2 3 4 5 6 7 8 9 10 11 12 13 14 15 16 17 18 1

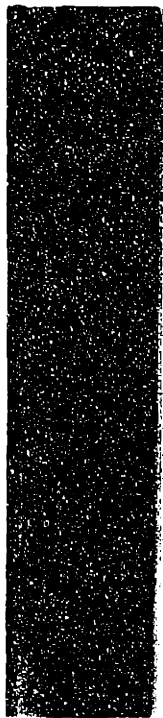


(b) (7) - (C)

1 2 3 4 5 6 7 8 9 10 11 12 13

13 14 15 16 17 18 19 20 21 22 23



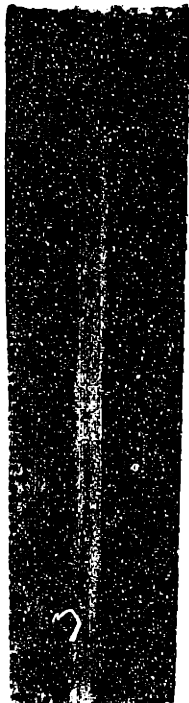


(a) #1434: High-purity



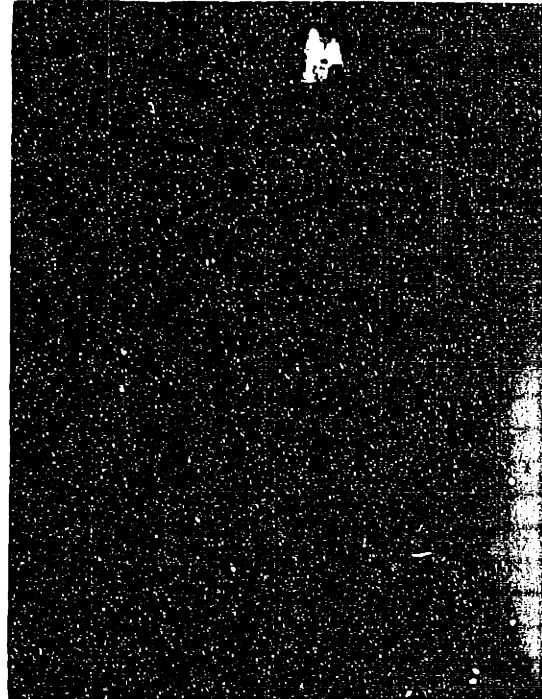
#1437: BaTiO₃ from purifying feed

(b) #1437: High-purity



#1440: High-purity BaTiO₃

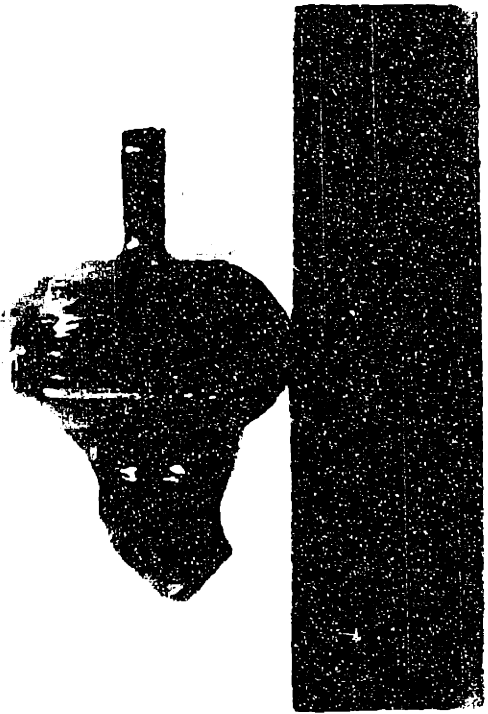
(c) #1440: High-purity



(d) #1442: 5ppm Fe

Figure A1.3 BaTiO₃ single crystals grown by TSSG.

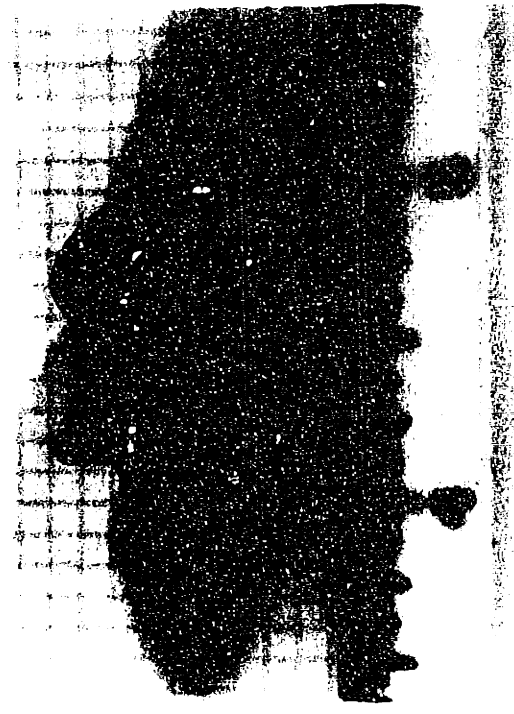
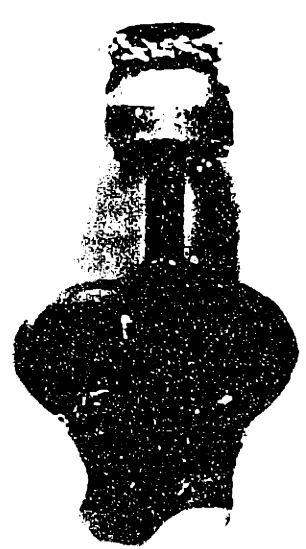
INTENTIONAL DUPLICATE EXPOSURE

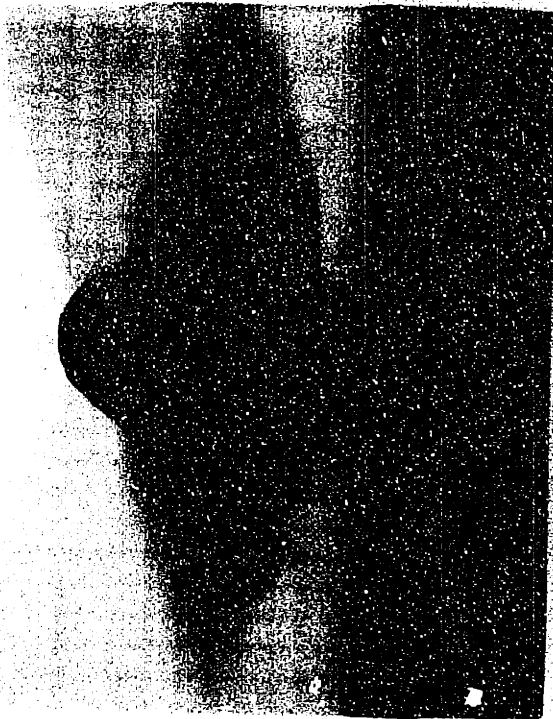


(D) #1443: 50ppm Fe

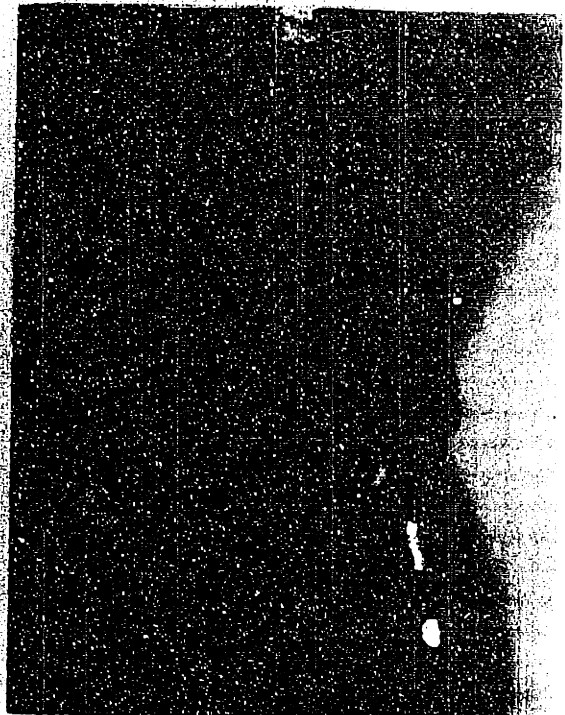


(E) #1446: 50ppm Fe

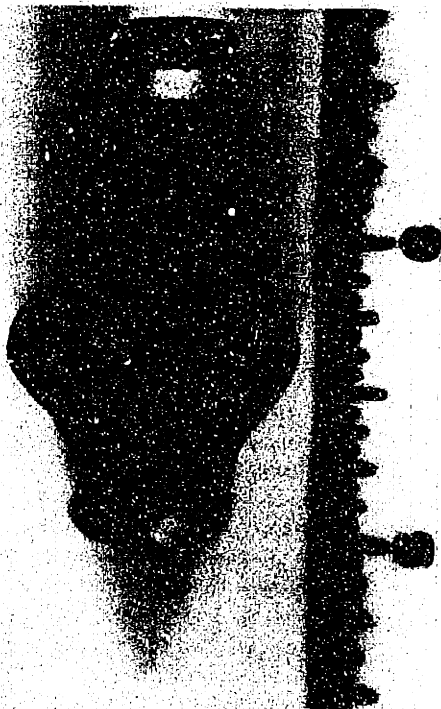




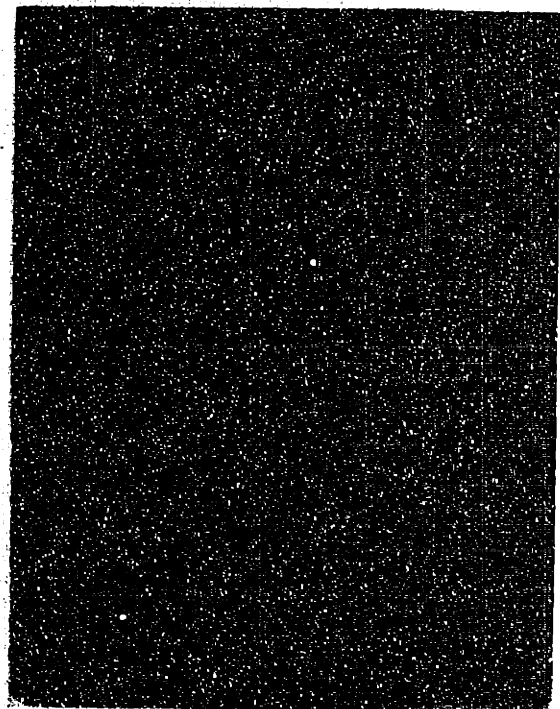
(e) #1443: 50ppm Fe



(f) #1446: 50ppm Fe



(g) #1448: 250ppm Fe



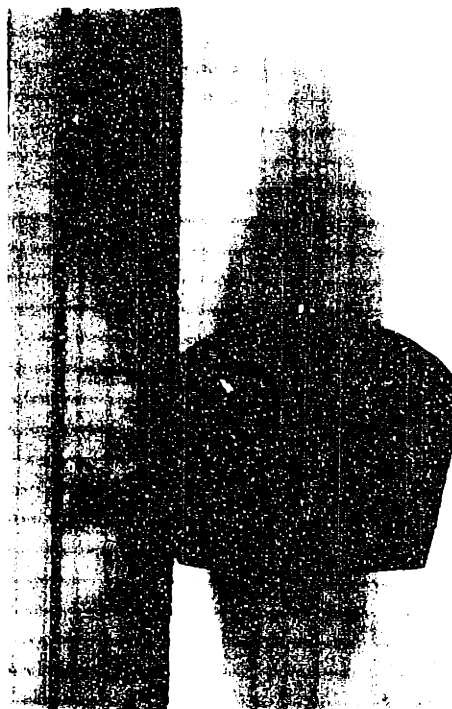
(h) #1451: 250ppm Fe

Figure A1.3 BaTiO₃, single crystals grown by TSSG (cont'd).

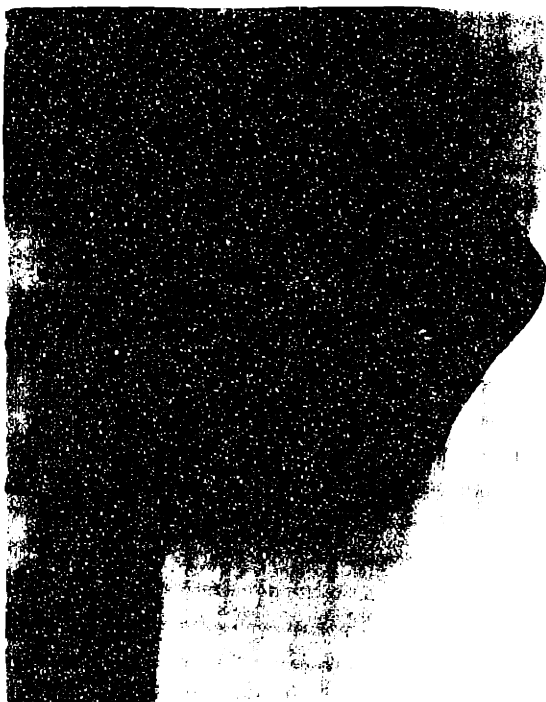
INTENTIONAL DUPLICATE EXPOSURE



(i) #1453: 500ppm Fe



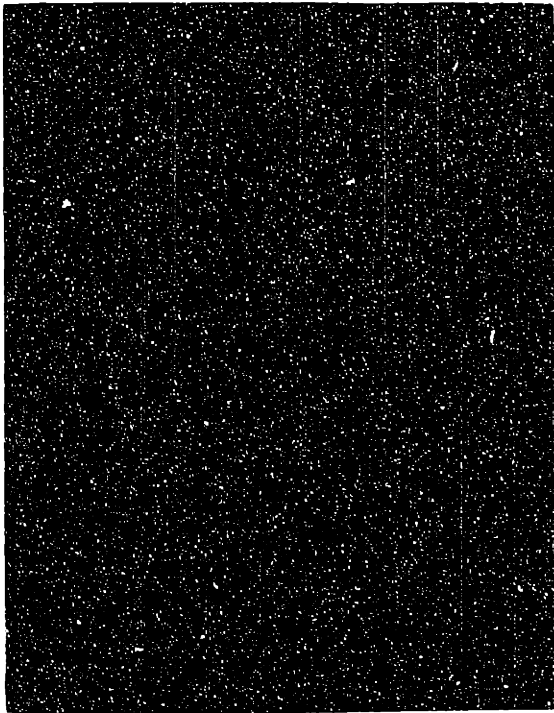
(j) #1457: 750ppm Fe



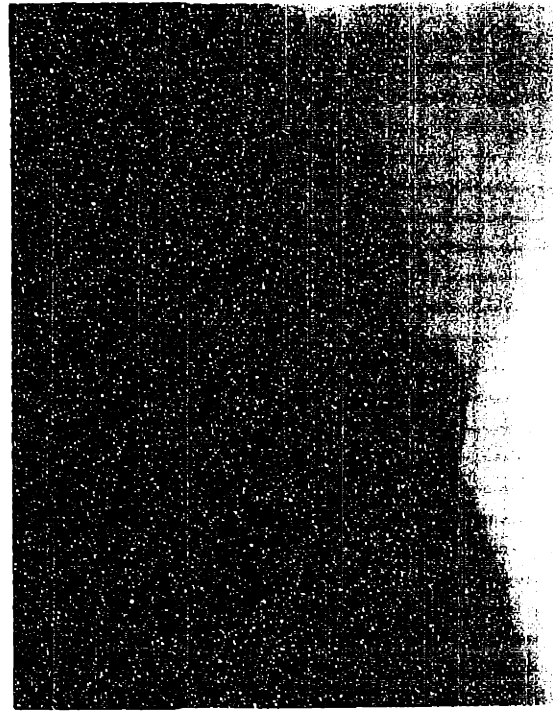
(k) #1454: 500ppm Fe



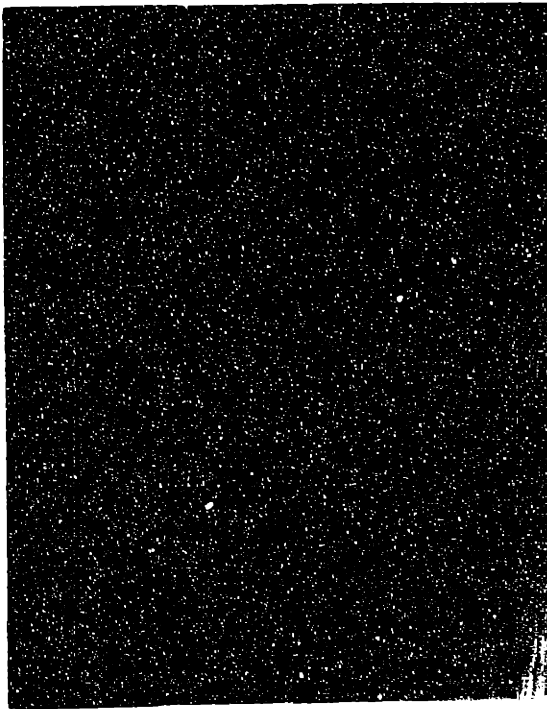
(l) #1455: 750ppm Fe



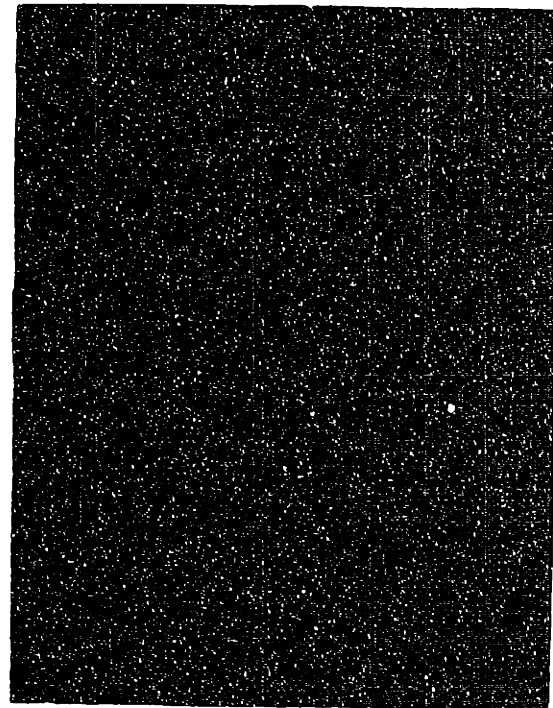
(i) #1453: 500ppm Fe



(j) #1457: 750ppm Fe



(k) #1459: 1000ppm Fe



(l) #1462: 1000ppm Fe

Figure A1.3 BaTiO₃, single crystals grown by TSSG (cont'd).

INTENTIONAL DUPLICATE EXPOSURE

APPENDIX 2

SAMPLES FOR USED OPTICAL EVALUATION

Table A2. Dimensions of Single Crystal samples used for optical evaluation. (Thickness a_1 used for optical absorption and diffraction efficiency measurements.)

Run #	[Fe] (ppm)	a_1 (mm)	a_2 (mm)	c (mm)	Comments
1434 A	Pure	2.90	3.87	6.08	Annealed
1434 B	Pure	3.24	5.67	6.10	
1437	Pure	4.58	9.73	8.97	Cracked during electrical poling
1442 A	5	4.58	8.17	6.77	Damaged during PR measurements
1442 B	5	6.43	8.33	6.77	Didn't elec- trically pole
1446 A	50	4.53	9.67	5.61	
1446 B	50	4.35	9.68	5.00	Annealed
1451	250	4.57	5.18	5.41	Broke during electrical poling Many domains
1453 A	500	4.49	6.58	6.53	
1453 B	500	4.53	5.63	5.96	Annealed
1457	750	4.54	6.01	6.88	
1462 A	1000	4.56	5.54	6.58	
1462 B	1000	4.57	5.27	6.09	Annealed

BIOGRAPHICAL NOTE

Peter Schunemann was born in Peabody, Massachusetts on March 20, 1962. He graduated from Peabody Veterans Memorial High School in 1980, and went on to study materials science and engineering at the Massachusetts Institute of Technology. He received the Bachelor of Science degree in 1984, after which he continued cooperative research on ceramics processing for multilayer capacitor production at Unitrode Corporation. In 1985 he returned to the Materials Science department at M.I.T. and studied BaTiO₃ crystal growth and characterization for photorefractive applications. After receiving the Master of Science Degree in 1987, he began employment at Sanders Associates in Nashua, N.H., to continue related work on BaTiO₃ and other single-crystal optical materials.